Superconductivity and Magnetism in the Extended Hubbard Model

A dissertation submitted to the
ETH Zürich
for the degree of the
Doctor of Natural Sciences

presented by
CARSTEN HONERKAMP
Dipl. Phys. ETH
born December 14th, 1971,
German citizen

Examiner Prof. T.M. Rice
Co-Examiner Prof. D. Vollhardt
Co-Examiner Prof. M. Salmhofer

ETH Diss. No. 13868
September 2000

Abstract

The general topic of this thesis is the interplay between superconductivity and magnetism in the extended Hubbard model on the two-dimensional square lattice. In the longer first part we investigate a system with infinite extension by a weak-coupling renormalization group method and describe how superconducting and magnetic tendencies can lead to a breakdown of the Landau-Fermi liquid state.

After introductory chapters focusing on certain aspects of two-leg Hubbard ladders and the two-patch model relevant for us, we describe a general renormalization group (RG) formalism for the one-particle irreducible vertex functions. Then we discuss the implementation of this scheme for the two-dimensional t-t' Hubbard model using a so-called N-patch technique which takes into account the full Brillouin zone.

Applying this scheme, we find a RG flow to strong coupling in a broad particle density and temperature range. This means that the interaction energies become larger than the bandwidth of the system and signals the breakdown of the weakly coupled Fermi-liquid state existing in normal metals at low temperatures. From the character of the flow to strong coupling we derive conjectures on the nature of the true strong coupling state of the system.

In the hole-doped parameter region of the model at band fillings smaller than one particle per site we compare the RG flow for the 2D case with the RG flow and other results for the half-filled two-leg Hubbard ladder. Due to the striking analogies between the RG flows of these two systems in a certain parameter region, we argue that in the two-dimensional t-t'-Hubbard model besides an antiferromagnetic phase around half-filling and a d-wave superconducting phase far away from half-filling there exists an additional intermediate phase with a partially truncated Fermi surface. The $\vec{k}$-space regions where the Fermi surface becomes destroyed exhibit the properties of an insulating spin liquid. This state, known to be the ground state of the half-filled two-leg Hubbard ladder, has a fully gapped spectrum (spin and charge gaps) and is not related to any kind of spontaneous symmetry breaking, i.e. all correlations remain purely short ranged. The saddle point regions of the two-dimensional dispersion close to the Fermi surface are identified as causing a mutual reinforcement between antiferromagnetic and d-wave superconducting fluctuations responsible for the formation of the unconventional strong coupling state. We further discuss the relevance of the insulating spin liquid state to the

pseudogap phase of the high-T_c cuprates and present results for the scattering rates of quasiparticles at the Fermi surface.

For the electron-doped side of the phase diagram we find a different picture which suggests that upon changing the electron density the ground state of the system changes abruptly from an antiferromagnetic phase with high characteristic energy scales to a d-wave superconducting state with low energy scale without the occurrence of an anomalous intermediate phase.

Further we briefly describe renormalization group results for special cases like the half-filled band and large values of the next-nearest neighbor hopping t'. There we find strong g-wave (or extended s-wave) pairing tendencies.

In the last chapter of this thesis we study the local interplay between magnetism and superconductivity at surfaces with [110] orientation. Within a mean-field analysis we compare different possible time-reversal symmetry breaking surface states leading to a split of the otherwise degenerate zero energy Andreev bound states observable in the tunneling conductance. Depending on the parameters we either find $s+id$ superconducting surface states or surface states with local magnetization due to the onsite Coulomb interaction as energetically most stable states.

Zusammenfassung

Das allgemeine Thema dieser Arbeit ist das Zusammenwirken von Supraleitung und Magnetismus im erweiterten Hubbard Modell auf dem zweidimensionalen Quadratgitter. Im längeren ersten Teil untersuchen wir ein unendlich ausgedehntes System mit Hilfe einer Renormierungsgruppen-Methode für schwache Kopplung und beschreiben, wie supraleitende und magnetische Tendenzen den Landau-Fermi Flüssigkeitszustand zerstören.

Nach einleitenden Kapiteln, die sich auf gewisse für uns bedeutsame Aspekte der halbgefüllten Hubbard Zwei-Bein-Leiter und des Zwei-Zonen-Modells konzentrieren, beschreiben wir ein allgemeines Renormierungsgruppen(RG)-Schema für die Ein-Teilchen irreduziblen Vertex-Funktionen. Anschliessend diskutieren wir die Implementierung dieses Schemas für das zweidimensionale t-t' Hubbard Modell. Dabei benutzen wir eine sogenannte N-Zonen-Technik, welche die gesamte Brillouin-Zone berücksichtigt.

Bei Anwendung dieses Schemas finden wir einen RG-Fluss zu starker Kopplung in einer weiten Teilchendichte- und Temperaturspanne. Dies bedeutet, dass die Wechselwirkungsenergien grösser als die Bandbreite des Systems werden, und signalisiert die Zerstörung des schwach gekoppelten Fermi-Flüssigkeitszustandes, welcher in normalen Metallen bei tiefen Temperaturen vorliegt. Aus der Art und Weise, wie der Fluss zu starker Kopplung von statten geht, leiten wir Vermutungen über den wahren stark gekoppelten Zustand des Systems ab.

In dem lochdotierten Parameter-Bereich des Modells bei Bandfüllungen mit weniger als einem Teilchen pro Gitterplatz vergleichen wir den RG-Fluss im zweidimensionalen Modell mit dem RG-Fluss und anderen Resultaten für die Zwei-Bein Hubbard-Leiter bei halber Füllung. Aufgrund der prägnanten Analogien zwischen den RG-Flüssen in diesen beiden Systemen in einem bestimmten Parameterbereich argumentieren wir, dass im zweidimensionalen t-t'-Hubbard Modell neben einer antiferromagntischen Phase nahe halber Füllung und einer d-Wellen supraleitenden Phase entfernt von halber Füllung eine Zwischenphase existiert, in der die Fermifläche auf Teilabschnitten zerstört wird. Die $\vec{k}$-Raum-Gebiete, wo die Fermifläche fehlt, weisen die Eigenschaften einer isolierenden Spinflüssigkeit auf. Dieser Zustand, bekannt als Grundzustand der zweibeinigen Hubbard-Leiter bei halber Füllung, weist keinerlei lückenlose Anregungen auf (Energielücken für Spin- und Ladungsanregungen) und beinhaltet keine spontane Symme-

triebrechung. Das bedeutet, dass alle Korrelationen kurzreichweitig sind.

Die Sattelpunktsgebiete der zweidimensionalen Dispersion werden als Ursache einer gegenseitigen Verstärkung zwischen antiferromagnetischen und d-Wellen supraleitenden Fluktuationen erkannt, welche letztendlich für das Auftreten des unkonventionellen stark gekoppelten Zustandes verantwortlich ist. Desweiteren diskutieren wir die Relevanz des isolierenden Spin-Flüssigkeitszustandes für die Pseudogap-Phase der Hoch-T_c-Kuprate und beschreiben Resultate für die Streurate von Quasiteilchen an der Fermifläche.

Für die elektrondotierte Seite des Phasendiagramms finden wir ein anderes Bild, welches nahelegt, dass hier bei Änderung der Elektronendichte der Grundzustand abrupt von einer antiferrromagnetischen Phase mit hoher charakteristischer Energieskala zu einem d-Wellen supraleitenden Zustand auf niedriger Energieskala wechselt, ohne dass ein anormaler Zwischenzustand auftritt.

Weiter beschreiben wir kurz Renormierungsgruppen-Resultate für Spezialfälle wie halbe Füllung und grosse Werte des Hopping-Parameters zwischen übernächsten Nachbarn. Dort finden wir starke Tendenzen zu g-Wellen-(oder extended s-Wellen-) Paarbildung.

Im letzten Kapitel dieser Arbeit betrachten wir das lokale Zusammenwirken von Supraleitung und Magnetismus an Oberflächen mit [110] Orientierung. Im Rahmen einer Mean-Field-Analyse vergleichen wir verschiedene Oberflächenzustände, welche die Zeitumkehr-Invarianz brechen und zur Aufspaltung des sonst bei Energie null entarteten Andreev Bindungszustandes führen. In Abhängigkeit von den Parametern finden wir entweder $s + id$ supraleitende Oberflächenzustände oder solche mit lokaler Magnetisierung aufgrund der Coulomb-Wechselwirkung als energetisch stabilste Zustände.

Preface

The main part of this thesis originates from the second half of my Ph.D. time at ETH. It deals with the question how the Landau-Fermi liquid breaks down in the two-dimensional Hubbard model and what one can infer from this about the nature of the true ground state. The method we choose for this analysis is a N-patch renormalization group (RG) scheme taking into account perturbative corrections to the interaction stepwise to successively lower energy scales. Here we give a short critique of this part of the thesis.

As positive results we remark:

- Our method yields results which are consistent with related RG studies and also with other approaches such as mean-field and quantum Montecarlo calculations (Chapter 8). The N-patch RG represents a numerically robust scheme for one-loop RG in two-dimensional models with a high $\vec{k}$-space resolution for the interactions. Despite the large number of variables and the numerical effort, these calculations allow to understand many of the results on a simple analytical level. Moreover we present an approximate method for the computation of quasiparticle scattering rates and do first steps to include selfenergy corrections like the FS shift into the one-loop flow.

- The saddle point regions of the two-dimensional tight-binding dispersion are identified as important link between d-wave superconducting and antiferromagnetic (AF) fluctuations. This opens a way to a mutual reinforcement of these two channels helping to understand how d-wave superconductivity can occur at comparably large energy scales. The relevance of the next nearest neighbor hopping t' for the interplay of these channels is clarified.

- The analogy of the RG flow in the t-t' Hubbard model and in the half-filled two-leg Hubbard ladder as found by the two-patch model studied in [Furukawa 1998] is verified to hold for a broad parameter region in the full two-dimensional treatment as well. This suggests the formation of an insulating spin liquid (ISL) in the saddle point regions. The schematic conclusions from this scenario compare well with experimental findings in the high-T_c cuprates.

- Our RG analysis indicates how the observed differences between the hole- and

electron-doped cuprates can be understood from a weak-coupling picture of the t-t' Hubbard model. (Chapter 7).

- For large values of the next nearest neighbor hopping we find a g-wave instability which can be understood as arising from approximate nesting of Fermi Surface (FS) parts connected by incommensurate wavevectors. This enriches the variety of potential ground states for the extended Hubbard model.

Here we comment on the drawbacks of the analysis:

- The RG results are complex and no clearcut distinctions between different regimes can be made. Most of the results require a careful analysis and have to be taken qualitatively. I preferred to show as much raw data as possible instead of only drawing phase diagrams from somewhat arbitrary criteria.

- Because of the flow to strong coupling the perturbative RG scheme breaks down at low energy scales. Only if we choose very small initial interactions the flow has developed a definite structure before the interactions exceed the order of the bandwidth. We are however interested in the physics of the high-T_c cuprates and should choose at least moderate bare interactions for a realistic description. This means that our analysis rather provides a consistency check for physical ideas than quantitative results or even proofs.

- Due to the lack of a strong coupling theory for the ISL in higher-dimensional systems we can compare our data to experiments only at high temperatures where the flow to strong coupling does not occur. For the strong coupling regime at low temperatures the comparison is possible only on a rough schematic level.

The structure of the thesis is as follows:

In Chapter 1 we review aspects of Landau-Fermi liquid theory and its breakdown. Then we briefly describe the physics of the high-T_c cuprates and the Hubbard model. Finally we discuss how unconventional superconductivity can arise from repulsive interactions.

In Chapter 2 we repeat the analysis of the RG flow in the half-filled Hubbard ladder in a formulation close to the one used later for the two-dimensional Hubbard model. We discuss how the mutual reinforcement between AF and d-wave channel arises and show how such an RG flow can occur at the saddle points of the two-dimensional Hubbard model as well.

Chapter 3 contains a description of the RG scheme for the one-particle irreducible vertex functions and related RG approaches.

In Chapter 4 we describe the numerical implementation of this scheme for the two-dimensional Hubbard model using the so-called N-patch technique.

Chapter 5 contains the discussion of the flow to strong coupling on the hole-doped side of half-filling. We classify the flow using three regimes, one of which is the saddle-point regime where we find a RG flow analogous to the half-filled two-leg Hubbard ladder. We discuss the one-loop Fermi surface shift, potential other instabilities and describe the scenario of ISL formation at the saddle points. These points have been written up in [HSFR 1999].

In Chapter 6 we calculate the scattering rates for quasiparticles at the FS with an approximate method based on our RG scheme. We compare the results to recent photoemission experiments.

Chapter 7 contains the RG analysis of the electron-doped case for band fillings larger than one. The saddle point regime found on the hole-doped side is absent on the electron-doped side and the instability is either strongly dominated by AF processes with high characteristic energy scale or by d-wave Cooper processes diverging at a much lower energy scale.

In Chapter 8 we first consider the half-filled cases for $t' = 0$ and $t' \neq 0$. Then we analyze the RG flow for large values of $|t'|$ and find an unusual g-wave Cooper instability caused by approximate nesting.

Chapter 9 briefly describes part of the work I did in collaboration with Prof. Manfred Sigrist in the first part of my Ph.D. time at ETH. There we analyze different possibilities to split the degenerate zero-energy Andreev bound states at [110] surfaces of $d_{x^2-y^2}$ superconductors, published in [HS 2000]. The main motivation were experimental results by Covington et al. [Covington 1997], which showed a low-temperature splitting of the zero-bias peak in the tunneling conductance measuring the local density of states at these surfaces. This splitting had already been ascribed to a spontaneous breaking of time-reversal symmetry by formation of an $s + id_{x^2-y^2}$-wave state at the surface for low temperatures [Fogelström 1997]. Our goal was to show that within a mean-field study of an extended Hubbard model this scenario which fits the experiments rather well does not represent the only possibility to obtain the observed split of the zero-bias conductance. We propose two alternative scenarios: the spontaneous current state (also suggested by [Higashitani 1997]) lifting the orbital degeneracy of the bound states, which turned out to be a ξ/λ effect[1] and therefore too small to explain the experiments[2]; and a magnetic surface state splitting the spin degeneracy which yielded surface densities of states compatible with the experiment. An experimental distinction between the magnetic surface state and the $s + id_{x^2-y^2}$-wave surface state is at least theoretically possible by spin-resolved tunneling spectroscopy.

Another more phenomenological project from this first half of my Ph.D. time on the competition between 0- and π-phase shift in Josephson junctions with Sr_2RuO_4 and Pb

[1] ξ denotes the superconducting coherence length and λ the in-plane penetration depth.

[2] Nonetheless a similar state proved to give useful results in the description of paramagnetic reentrance effects in proximity structures [Fauchère 1999].

is not included in this thesis [HS 1998].

Contents

Chapter 1

Introduction

1.1 Landau-Fermi liquid theory, its breakdown and new fixed points

Originally developed by Landau in the 1940s and 1950s as a phenomenological concept to describe the low energy excitations in strongly interacting fermion systems such as ^{3}He, *Landau-Fermi liquid theory* has become the standard theory of metals. Later on its fundamental assumptions were justified for certain classes of fermionic systems in dimensions higher than one starting from different microscopic descriptions, such as standard quantum field theoretical methods (e.g. [AGD]) or modern renormalization group (RG) ideas (see [Salmhofer 1999] and references therein, also [Shankar 1994] and [Chen 1995]). The RG methods allow to show to all orders in perturbation theory that for a rather general class of two-dimensional systems[1] Landau-Fermi liquid behavior is valid provided that the interactions are sufficiently weak and the Cooper channel is blocked.

The main theoretical implication of Landau-Fermi liquid theory is a one-to-one correspondence between the bare particles of the non-interacting system and the *renormalized* particles, called *quasiparticles*, of the possibly strongly interacting system. What remains after this renormalization process from the interaction between the bare electrons is a Hartree-like interaction between the quasiparticles whose effect can be taken into account properly. From this description the experimental milestones of Landau-Fermi liquid theory can be deduced, which are various simple laws for the temperature and frequency dependencies of thermodynamic and transport properties like the specific heat or

[1] The Fermi surface of the system is required to have positive curvature and the gradient of the dispersion has to be non-zero on the FS (for precise conditions see [Salmhofer 1999]). Therefore in the following analysis with the FS close to the van Hove singularities, these conditions are violated. Moreover we choose a moderate interaction strength, such that the curvature arguments do not prevent a flow to strong coupling from one-loop particle-hole diagrams.

the T^2 dependence of the quasiparticle lifetime and the resistivity, respectively.

The reason why Landau-Fermi liquid theory works is the vanishing of the scattering rate for the quasiparticles at the FS and the dominance of forward scattering between them at low energy scales. At temperatures T low compared to the Fermi energy E_F or when one probes the system with small external frequencies ω, the relevant contributions will come from low energy excitations out of a region of thickness $\Lambda \sim T, \omega$ around the Fermi surface. If we now ask which scattering processes could modify the results for the non-interacting system, the overwhelming part of these processes will be given by forward scattering processes[2]. More precisely requiring that for a generic two-particle scattering process with total momentum $\vec{P} \neq 0$ the initial and final states lie in the Λ-shell around the Fermi surface, where Λ is some small energy scale, we can easily see [Shankar 1994, Chen 1995] from the left plot in Fig. 1.1 that for given incoming wave-vectors $\vec{k}_1$ and $\vec{k}_2$ the outgoing wavevectors $\vec{k}_3$ and $\vec{k}_4$ must be within small segments of volume $\sim (\Lambda/E_F)^2$ around $\vec{k}_1$ and $\vec{k}_2$. This phase space restriction causes the scattering rate for quasiparticles at the FS to vanish like $\sim (\omega/E_F)^2$ or $\sim (T/T_F)^2$, i.e. the quasiparticles become well-defined at a sufficiently low energy scale. Further considering the limiting case $\Lambda \to 0$ it is justified to parameterize the scattering processes with the Landau function $f(\vec{k}, \vec{k}')$ with wave-vectors $\vec{k}$ and $\vec{k}'$ on the Fermi surface (for a precise discussion of the relation relation between the microscopic scattering vertex and the Landau function, see [Hewson 1994, Metzner 1998, Dupuis 1998]).

The reduction of the interaction to a Landau function $f(\vec{k}, \vec{k}')$ yields an important simplification of the Hamiltonian: the effective low-energy Hamiltonian now reads

$$H = \sum_{\vec{k}} \epsilon(\vec{k}) n(\vec{k}) + \frac{1}{2V} \sum_{\vec{k},\vec{k}'} f_{s_1 s_2 s_3 s_4}(\vec{k}, \vec{k}') \; c^\dagger_{\vec{k},s_3} c^\dagger_{\vec{k}',s_4} c_{\vec{k}',s_2} c_{\vec{k},s_1} \tag{1.1}$$

Therefore the effective theory is of Hartree-type, which implies that arbitrary (spin-independent) variation of the phases of the single-particle wave-functions for different wave-vectors $\vec{k}$ leave the Hamiltonian (1.1) unchanged: the low energy theory has local gauge invariance in $\vec{k}$-space. It is most natural to expect that the ground state wave function will respect this symmetry and will hence be given by an uncorrelated Slater determinant of single-particle wave-functions with well-defined wave-vectors $\vec{k}$. From (1.1) one obtains the Landau energy functional

$$\delta E = \sum_{\vec{k}} \tilde{\epsilon}(\vec{k}) \delta n(\vec{k}) + \frac{1}{2V} \sum_{\vec{k},\vec{k}'} f_{s_1 s_2 s_1 s_2}(\vec{k}, \vec{k}') \; \delta n(\vec{k}) \delta n(\vec{k}') \tag{1.2}$$

Using this expression, observable quantities can be systematically calculated to a given order in the deviations $\delta n(\vec{k})$ from the ground-state (described e.g. in [Pines&Nozières]).

[2] For the moment we ignore the Cooper processes with $\vec{P} = 0$ which can of course cause a low-scale instability of the Landau-Fermi liquid.

The effect of the interaction can be captured through a set of Landau parameters which renormalize the expressions for the non-interacting case.

In this thesis we want to analyze possible ways how the Landau-Fermi liquid description can fail and try to determine the nature of the new state of the system. We will mainly use an renormalization group language where we attempt to obtain an effective low-energy theory by a systematic successive elimination of higher energy modes. In the course of this scheme typically some *relevant* parameters or processes will become dominant, while the importance of some other *irrelevant* terms decreases. If we extrapolate these changes in the effective action we may reach a fixed point in the sense that the flow of the relevant parameters reaches some asymptotic form while the irrelevant parameters have become unnoticably small. If there are relevant parameters in the theory the physics at lowest energy scales is mostly determined by them.

In the Landau-Fermi liquid example above there are no relevant terms which grow if we reduce the energy scale, therefore the low energy theory is characterized by what is left over when we restrict the phase space to lower energy scales. These are the *marginal*[3] terms, in our case the kinetic energy and the forward scattering processes, which remain qualitatively unchanged in the mode elimination. Therefore the Hamiltonian (1.1) can be regarded as the fixed point of a series of theories initially having a more complicated interaction constrained to lower and lower energy scales.

Although the Landau-Fermi liquid state has a remarkable range of validity, it is clear that it cannot exist for all interaction strengths. Already within the Landau-Fermi liquid description one is led to stability criteria which constrain the range of interaction for which the theory can be applied (see [Pines&Nozières]). Further if the interaction is too strong a description built on quasiparticles with well-defined wave-vectors becomes inappropriate. This occurs in many strongly correlated systems where the interaction energy through the Coulomb repulsion between the electrons becomes comparable to the kinetic energy. Consider e.g. a large U-Hubbard model: there the energetically largest term, the on-site Coulomb repulsion has a local gauge invariance in real space rather than in $\vec{k}$-space. Therefore single-particle excitations with different wave-vectors will become correlated and the quasiparticle picture of (1.1) can break down at some critical interaction strength[4]. This failure occurs because one of the two building blocks of Landau-Fermi liquid theory loses its relevancy: when we look for a low energy theory it is no longer sufficient to narrow the phase space to regions of small kinetic energy around the FS.

In this thesis we want to concentrate on the weak-to-moderate interaction cases, where the kinetic energy is still the dominating term in the Hamiltonian. Then the other building block of Landau-Fermi liquid theory, the Fermi surface geometry in combination with the Pauli principle, will play a decisive role.

[3] In the simple sense that they do neither grow drastically nor vanish.

[4] According to current pictures e.g. for the half-filled Hubbard model the fraction of the spectral weight which is represented by 1.1 vanishes at the critical point, see also Subsection 1.2.2.

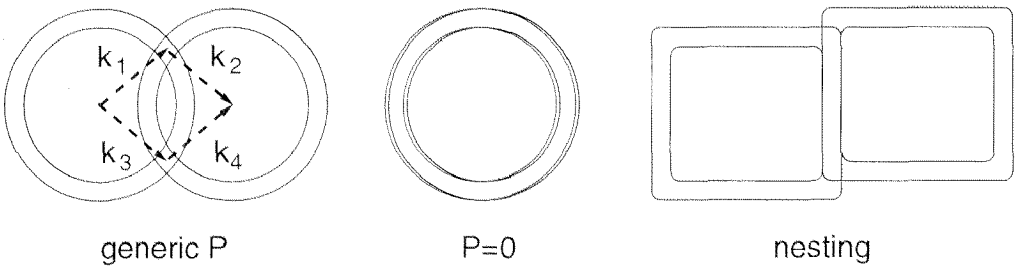

Figure 1.1: *Left: the generic case* $\vec{P} = \vec{k}_1 + \vec{k}_2 \neq 0$. *The low energy final states are constrained to the overlap regions of the* Λ*-shell around the FS and its translate by* $\vec{P}$. *The volume of this overlap is* $\propto \Lambda^2$. *Middle: For* $\vec{P} = 0$, *the possible final state are constrained to a volume* $\propto \Lambda$. *Right: the case of a nested FS.*

In situations where Landau-Fermi liquid theory is appropriate, the irrelevance of non-forward scattering processes at low energy scales arises from the curvature of the FS, as can be clearly seen in 2 dimensions from Fig. 1.1. In the generic case in the left plot the overlapping regions of the Λ-shells around the Fermi surface and its translate decrease at least [Salmhofer 1999] as $\Lambda^{3/2}$ for $\vec{P} = \vec{k}_1 + \vec{k}_2 \neq 0$, hence drastically constraining the outgoing wavevectors.

Next let us discuss which additional processes can enter the low-energy effective theory under certain circumstances. In dimensions larger than one there are two obvious cases where we would find a much wider low-energy phase space: one case arises for $\vec{P} = 0$, where the Λ-shells around the Fermi surface and its translate overlap perfectly[5] and the outgoing wavevectors adding up to zero can lie everywhere around the FS. In the second case the curvature is zero on some parts of the FS such that we can obtain overlapping regions which only decrease $\propto \Lambda$. Here the restriction to forward scattering processes becomes impossible as well, as the low-energy outgoing states allowed by wavevector conservation are no longer constrained to small regions close to the incoming wavevectors.

The larger number of low-energy scattering states has a far-reaching consequence: singularities can occur in second order perturbation theory because the decrease of the available low-energy phase space does no longer cancel the smallness of the energy denominators $\sim \Lambda$. In the first of the two cases mentioned above this leads to the well-known Cooper instability in the pairing or particle-particle channel while the second case is referred to as *nesting*, which typically occurs in the particle-hole channel. In both cases second order corrections to the scattering processes become singular at zero temperature and for an appropriate bare interaction the summation of an infinite number of these contributions leads to a divergence of these processes already at finite energy or frequency indicating an instability of the ground state. It should be noted that this

[5] We assume that parity is a symmetry of the system.

breakdown of the Landau-Fermi liquid does not require a true singularity of lower order (e.g. 2nd order) fluctuations, due to the summation of higher order processes (e.g. ladder summations) such a divergence can still occur at finite temperatures or for imperfect nesting provided the interaction is sufficiently strong.

In generic higher-dimensional systems it is unlikely that two different singularities like the Cooper and nesting instabilities occur at comparable energy scales. The reason is that the momentum space overlaps (see Fig.1.1) responsible for these channels becoming large involve different parts of the low energy regions around the FS. Moreover the interactions appearing in the summation of higher order processes which lead to the singularities are generally different.

The situation is however distinct in one-dimensional or quasi-one-dimensional systems. Due to the absence of Fermi surface curvature in 1D these systems are always nested and the low energy phase space for these $2k_F$-nesting processes is typically the same as the one available for the Cooper channel. As a consequence the same wavevectors can couple into different singular channels providing an intrinsic coupling between them. Thus the variety of possible non-Fermi liquid states becomes large. Apart from cases where again only a single channel dominates the low energy theory there are also cases where different channels combine to give more complex states. One example is the Luttinger liquid (for a review on 1D systems see [Voit 1994]): here particle-particle and particle-hole contributions exactly cancel at the one-loop level while the frequency dependence of the full selfenergy becomes infinitely steep at $\omega = 0$ such that the quasiparticle pole disappears. Correspondingly the ground state is a weak-coupling non-Fermi liquid state. Another example will be presented in Chapter 2: the half-filled two-leg Hubbard ladder. There, AF and d-wave pairing channels become strongly coupled due to certain Umklapp processes and mutually reinforce their flow to strong coupling. Thus the true strong coupling state, the so-called *insulating spin liquid*, exhibits both strong AF and d-wave fluctuations but has also spin and charge gaps arising from the combined flow singlet-pairing and insulating tendencies. It should be noted that the ISL ground state is not related to any kind of (quasi-) long range order: all correlation function are short ranged and decay exponentially. Hence it can be considered a Mott insulating state with the remarkable property that it exists at arbitrarily small repulsive interaction U.

The root of such a complex and interesting behavior lies in the intrinsic reinforcing coupling between different channels. An alternative point of view is to say that different channels like the AF or the d-wave channel receive a *substantial* part of their enhancement at low energy scales from the same interaction processes. One might expect that such a mechanism exclusively occurs in low spatial dimensions, as there the phase space overlaps are largest. In the main part of this thesis we want to show that due to special features of the energy landscape there is the possibility for such a complex non-Fermi-liquid fixed point also in the the two-dimensional t-t' Hubbard model. Our result is that in a certain parameter range, which we call the *saddle point regime*, the RG flow towards strong coupling is consistent with the formation of an insulating spin liquid in

certain parts of the Brillouin zone.

It should be noted that the reinforcing coupling between superconducting and antiferromagnetic fluctuations complicates the analysis of the strong coupling phase substantially. As clear from the absence of long-range order in the ISL state in the two-leg Hubbard ladder and suggested by the RG flow in the two-dimensional case as well, a straightforward mean-field approach will not yield a proper description of the low energy physics. Moreover already due to the flat dispersion in the saddle point regions multi-dimensional bosonization schemes are inapplicable such that the strong coupling analysis for the two-leg ladder[Lin 1998, Fisher 1998] cannot be taken over to the two-dimensional case. Thus for the analysis of the two-dimensional case we will mainly make use of susceptibilities and selfenergies which can be calculated perturbatively down to energy scales where the flow to strong coupling sets in. This implies that most of our results merely show tendencies and only qualitative conclusions can be drawn.

1.2 The high-T_c cuprates and the two-dimensional Hubbard model

1.2.1 The physics of the high-T_c cuprates

Since the discovery of superconductivity in $LaCuO_4$ [Bednorz&Müller 1986] the physics of the high-T_c cuprates has become one of the most debated topics of condensed matter physics. Rather soon a broad consensus arose that the most interesting properties of these materials emerge from the CuO_2 planes common to all known high-T_c superconductors. An important experimental parameter in these systems is the *doping*, which determines the charge carrier density in the cuprate planes[6]. Since the relevant electronic states close to the Fermi level mainly derive from rather narrow copper $3d_{x^2-y^2}$ orbitals, the Coulomb repulsion plays a dominant role: upon changing the carrier density the behavior of the cuprates changes from a Mott insulating state to a poor but rather conventional metallic state. The main challenge for a theoretical model of the high-T_c materials lies in the proper description of this wide range of ground states - in particular because the typical methods appropriate for the one extreme fail to be valid on the other side of the density axis.

A qualitative phase diagram of the cuprates is shown in Fig. 1.2. At half-filling (left side of the diagram) the system is an antiferromagnetic Mott insulator with a charge gap of approximately $2eV$. The antiferromagnetism and the corresponding spin excitations live on a much smaller energy scale with Néel temperature $T_N \approx 300-600K$ and Heisenberg exchange coupling $J \approx 0.13eV$. The metallic state in the high doping region on the very right side of the diagram is can characterized as a poor Landau-Fermi liquid. There, since the carrier concentration in the planes is far from half-filling, the strong local Coulomb repulsion between the electrons does not affect the qualitative behavior. As the carrier concentration is increased the system enters a $d_{x^2-y^2}$-wave superconducting phase or, at higher temperatures, the so-called spin-gap or pseudo-gap phase[7].

The d-wave superconducting state develops unusual properties [Lee 1999] when one moves further to the left on the doping axis decreasing the hole-concentration x with respect to half-filling: although the number of electrons increases, the superconducting density measured from the penetration depth decreases and appears to be roughly $\propto x$ towards the underdoped region. Moreover the condensation energy deduced from the specific heat anomaly at $T_c(x)$ reaches a maximum at the maximal T_c (optimal doping) and decreases as well towards half-filling [Tallon 2000]. Nonetheless other features of the superconducting state like quasiparticle properties and interference effects are well

[6] In a one-band description the undoped state ($x = 0$) corresponds to a half-filled band and hole-doping ($x > 0$) reduces the number of electrons.

[7] The question whether the pseudogap line merges with the superconducting critical temperature (like e.g. in the ISL scenario discussed below) or whether there is a quantum critical point hidden by the superconducting phase is still open, see [Tallon 2000] for a recent discussion.

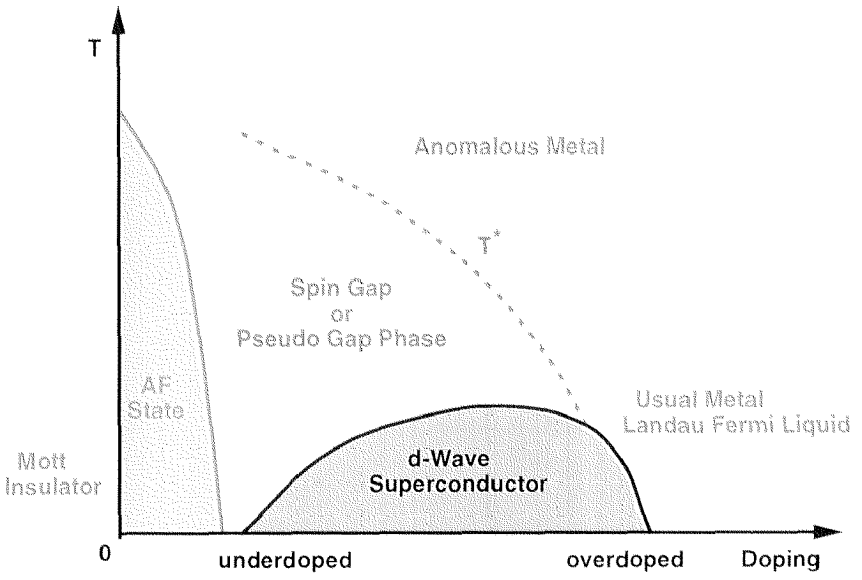

Figure 1.2: *Schematic phase diagram of the high-T_c cuprates.*

described within a conventional d-wave BCS framework.

The normal state transport properties become anomalous as well around optimal doping: the Hall coefficient changes sign and the in-plane resistivity exhibits an almost linear temperature dependence (for a detailed discussion see [Anderson 1997]) over a striking range of several hundred Kelvins. This linear behavior is against the expectations from ordinary Landau-Fermi liquid theory[8], moreover the large extension of this behavior in temperature and its apparent insensitivity against other influences like phonons has lead to many theoretical conjectures like "quantum protectorates" [Anderson 2000, Laughlin 2000] and underlying quantum critical points [Sachdev 1999, Abanov 2000].

The pseudogap state (for a recent review and references see [Timusk 1999]) setting in below the characteristic temperature $T^*(x)$ exhibits a rapid decrease of the Pauli spin susceptibility (the spin gap seen in the Knight shift) signaling a suppression of low-lying spin excitations and a general loss of low energy spectral weight observed in tunneling [Renner 1998] and photoemission. In particular angle-resolved photoemission (ARPES) measurements give evidence for the formation of a pseudogap in the $(\pi, 0)$ and $(0, \pi)$ regions in of the BZ, while gapless Fermi arcs with quasiparticle peaks remain near the BZ diagonals [Norman 1998]. On the other hand thermodynamic quantities like the specific heat do not show strong anomalies at T^*. Similarly, when cooling the sample into the pseudo-gap state, the in-plane-resistivity only shows a small step-like decrease signaling that some scattering mechanism may freeze out below T^*.

[8]For a two-dimensional Fermi liquid with cylindrical FS, the resistivity should be proportional to $T^2 \log(T/\mu)$ [Hodges 1971].

From these observations it appears plausible that the transition into the pseudogap state is not a thermodynamic phase transition but a continuous destruction of low energy excitations responsible for observable changes of certain properties while other low energy excitations remain. Therefore some properties like the in-plane resistivity which are dominated by the latter class of gapless excitations do not change drastically. Such a partial suppression of the low energy spectral weight which becomes more pronounced towards half-filling may also be the cause for the unusual doping-dependence of the condensation energy and the superfluid weight: only the remaining part of the low-energy excitations take part in the formation of a superfluid condensate.

From the ARPES results mentioned above it seems that the partial gap formation in the pseudogap state should occur around the $(\pi, 0)$ and $(0, \pi)$ points in the two-dimensional BZ. This picture is also qualitatively consistent with the doping dependence of the c-axis conductivity which shows insulating behavior in the underdoped region. The c-axis transport is mainly incoherent, in lowest order [Ioffe 1998] we have

$$\sigma_c \propto t_\perp(\vec{k})^2 N(\vec{k}) Z(\vec{k})^2 / \Gamma(\vec{k})$$

with $t_\perp(\vec{k})$ being the inter-plane hopping amplitude and $N(\vec{k})$ denoting the density of states with quasiparticle weight $Z(\vec{k})$ and width $\Gamma(\vec{k})$ for wavevector $\vec{k}$ in the plane. According to crystal structure considerations [Andersen 1995] $t_\perp(\vec{k})$ is maximal for $\vec{k}$ around $(0, \pi)$ and $(\pi, 0)$ and zero for $\vec{k} \propto (\pi/2, \pi/2)$. Therefore a destruction of the low-energy spectral weight around $(0, \pi)$ and $(\pi, 0)$ yields a drastic decrease of the c-axis conductivity.

A priori it is not clear whether the non-Landau-Fermi liquid phases towards the half-filled Mott insulating state can be - at least qualitatively - understood from a weak-coupling point of view, i.e. an analysis built on perturbing the non-interacting or Landau-Fermi liquid state. However exactly the experiments described above give us some confidence that this may indeed be the case: plane-wave amplitudes for different $\vec{k}$ vectors extracted in the photoemission experiments behave rather distinctly, showing that the single-particle content of the low-energy excitations plays a substantial role. Moreover the location of these low energy features roughly coincides with the expectation from the non-interacting model, thus the kinetic energy is not entirely dominated by the electronic interaction. Therefore it seems justified to use a weak-coupling approach in attempting to understand qualitatively the mechanisms leading to some of the observed phases[9].

1.2.2 The Hubbard model

The Hubbard model belongs to the most studied models in modern condensed matter physics. Originally it was introduced independently by Gutzwiller, Hubbard and

[9]This applies mainly to the doping regions further away from half-filling. The antiferromagnetic state at half-filling in the real cuprates is certainly better described by a Heisenberg model than by some weak-coupling SDW calculation.

Kanamori in the study of narrow band transition metals. In the form which we are going to use here, its Hamiltonian is given by

$$H = -t \sum_{\substack{ij \\ \text{n.n.}}} \left(c^\dagger_{i,s} c_{j,s} + c^\dagger_{j,s} c_{i,s} \right) - t' \sum_{\substack{ij \\ \text{n.n.n.}}} \left(c^\dagger_{i,s} c_{j,s} + c^\dagger_{j,s} c_{i,s} \right) + U \sum_i n_{i,\uparrow} n_{j,\downarrow} . \quad (1.3)$$

Here, n.n. and n.n.n. denote the sum over nearest or next nearest neighbors of the two-dimensional square lattice. t and t' are the amplitudes for hopping processes between the corresponding lattice sites and $U > 0$ stands for the Coulomb repulsion for two electrons on the same lattice site. Since there are no exact results on the two-dimensional Hubbard model for the interesting parameter regions, one has to use approximate methods. Here we briefly describe some of the results.

Weak coupling: two and more phases? The weak-coupling, i.e. small-U/t physics of the Hubbard model has been studied extensively by many authors and will also be analyzed in some length in the following chapters. Here let us only mention several RG-like approaches to the two-dimensional Hubbard model in recent years.

Schulz [Schulz 1987] and Lederer et al. [Lederer 1987] studied the RG flow of the processes connecting the saddle points (like in the two-patch analysis of Furukawa et al. described in Chapter 2) emphasizing the divergence of both AF and d-wave pairing correlations. Similar studies have been given by Alvarez et al. [Alvarez 1998] and Gonzalez et al. [Gonzalez 1996]. Later on, in a related formalism based on parquet equations, Zheleznyak et al. [Zheleznyak 1997] examined the interplay between critical scales and effects of the FS curvature for a quasi two-dimensional model restricted to approximately flat FS faces which occur in the Hubbard model for small t' close to half-filling. Another study of nesting effects between flat FS segments was given by Vistulo de Abreu and Doucot [Vistulo 1997]. Zanchi and Schulz [Zanchi 1997] presented the first fully two–dimensional treatment, based on Polchinski's RG equation briefly discussed in the following chapter. They studied the two-dimensional Hubbard model with $t' = 0$ and found two different regimes with dominant AF in the one and d-wave pairing correlations in the other. A more detailed analysis of the leading instabilities was given by Halboth and Metzner [Halboth 2000] using RG equations for Wick ordered functions by Salmhofer [Salmhofer 1999], also described briefly in the following chapters. The general picture from these weak-coupling studies (apart from one treatment [Dzyaloshinski 1987], which discusses the weak coupling non-Fermi liquid fixed point of such a model) is that there is an antiferromagnetic state for a sufficiently flat FS close enough to half-filling and that, upon destroying the nesting either by doping or increasing the FS curvature, the flow to strong coupling is dominated by d_{x-y^2}-wave superconducting fluctuations. The Fermi surfaces and the dominant processes for these two parameter regions are shown in Fig. 1.3.

In this thesis we study the RG flow for the one–particle irreducible (1PI) vertex functions for the model given by (4.1) and (4.2) for larger absolute values of $t' \sim -0.3t$,

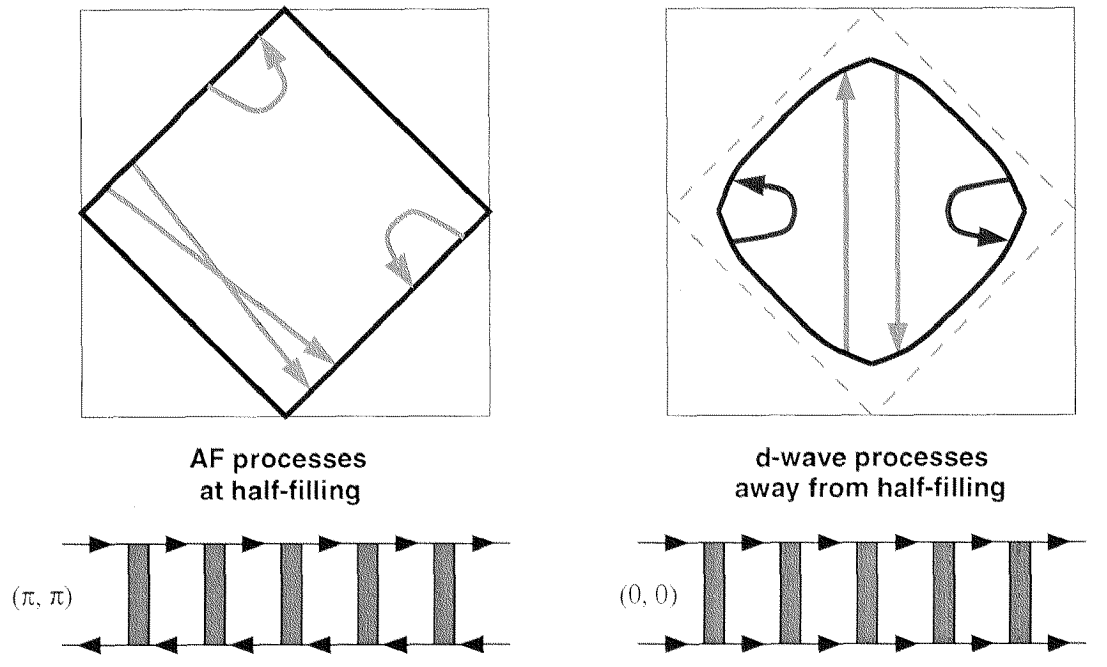

Figure 1.3: *Left: The FS of the $t' = 0$ Hubbard model at half-filling. The flow to strong coupling is dominated by AF processes $V(\vec{k}_1, \vec{k}_2, \vec{k}_3)$ (shown as rectangular boxes) with momentum transfer $\vec{Q} = (\pi, \pi)$ between second incoming $\vec{k}_2$ and first outgoing wavevector $\vec{k}_3$. The particle-hole ladder with momentum transfer $\vec{Q}$ enhances these processes and can become singular at low T and sufficient nesting. Right: The FS away from half-filling, where the AF processes are cut-off. The flow is dominated by d-wave Cooper processes. The particle-particle ladder becomes singular at low T.*

to investigate the possibility of a novel strong coupling state in the parameter region between the d-wave and the AF regime of the studies mentioned above. This new phase, the insulating spin liquid, as suggested by the recent two-patch study by Furukawa et al. [Furukawa 1998], exhibits some salient properties (see Section 5.2) which let it appear as a good candidate to describe the physics of the optimally and underdoped cuprates. This contrasts with the two-phase pictures of the other weak-coupling studies described above, where e.g. the unusual superconducting properties of the cuprates defy any natural description. Further we emphasize the similarities of the two-dimensional RG flow to the flow in the two-leg Hubbard ladder and the two-patch model which provides a clear understanding how the ISL may occur in two dimensions.

Strong coupling: The Mott insulating state arises at strong coupling for large $U/t \gg 1$. Here, double occupancy of a lattice site costs a large energy compared to the typical kinetic energies such that these states will not enter the low-energy physics. Therefore the charge dynamics is strongly determined by the number of holes. A particular case arises for $n = 1$, the half-filled system: there no charge motion is possible without paying the large energy U. Thus the system is in an insulating state, known as the Mott state. The density of states which measures the number of available states for adding or removing particles, consists of two Hubbard bands separated by a energy gap $\sim U$. This is a rather general picture which - unlike the weak coupling phases described above - does not depend on details of the lattice and hopping parameters: as long as U is much larger than the bare bandwidth a possible kinetic energy gain cannot compensate for the repulsion energy which is required for any charge transport. The resulting excitation gap for charge motion is solely due to the Coulomb repulsion and does not involve the spin degrees of freedom.

Despite the charge gap there are still virtual hopping process involving doubly occupied sites. These lead to an effective antiferromagnetic exchange coupling $J = 4t^2/U$ between the electron spins on neighboring sites[10]. For large U this energy J governing the spin dynamics is much smaller than the charge gap. Therefore one can describe the low energy excitations by models defined in the subspace with no doubly occupied sites with the effective spin-spin coupling $J\vec{S}_i \cdot \vec{S}_j$ as interaction term - the Heisenberg model at half-filling or the t-J model for general band filling. By now there is general agreement that the ground state of the two-dimensional Heisenberg model has AF long range order [Manousakis 1991].

A precise study of the Mott metal-insulator transition in two dimensions is difficult and many open questions are currently debated in literature. Green's function decoupling methods originally introduced by Hubbard (for an overview see [Gebhard 1999]) start on the insulating side and show the closing of the Mott gap upon decreasing U, but the metallic state arising on the gapless side is not a Landau-Fermi liquid. Moreover the

[10] Of course the t'-hopping generates an additional J'-exchange term which can cause frustration effects.

spin degrees of freedom are not properly described and at small U/t the connection to Hartree solutions is problematic.

The Brinkman-Rice variational treatment of the Hubbard model using Gutzwiller projected wavefunctions ([Brinkman&Rice 1970], recent reviews in [Fazekas 1999] and [Gebhard 1999]) gives a metal insulator transition at finite U and describes the correlated metallic state comprehensibly in terms of a renormalized hopping parameter (implying a reduced Fermi step) and the average number of doubly occupied sides. It further corroborates the physical intuition that the Mott transition should take place solely due to charge correlations. An exact treatment of the Gutzwiller variational method however showed that a metal-insulator transition of this pattern does not occur in a finite number of spatial dimensions [Van Dongen 1989].

In the limit of infinitely many spatial dimensions, all correlations are purely local and the dynamical mean-field approach becomes exact [Metzner 1989] . Then the metal-insulator transition in the Hubbard model can be investigated numerically without uncontrolled approximations. With growing U these calculations ([Georges 1996, Bulla 1999]) show an increasing transfer of spectral weight to precursors of the upper and lower Hubbard bands while the quasiparticle band around around zero energy narrows progressingly and finally disappears at the metal-insulator transition. The DMFT phase diagram also contains a paramagnetic insulating state at non-zero temperatures while the insulating ground state shows AF order.

A model for the cuprates: Further let us briefly mention why the Hubbard model is believed to be an appropriate model for the cuprates planes of the high-T_c compounds. The Cu ion in CuO_2 planes has the electron configuration $3d^9$. Taking into account the tetragonal crystal field, hybridization with the p-orbitals of the surrounding oxygen octahedron and Jahn-Teller distortion of the latter one finds that the highest energy level which remains half-filled in the undoped system is the antibonding state between the oxygen p_x- and p_y-orbitals and the copper $d_{x^2-y^2}$ orbital where latter orbital gives the largest contribution. Therefore it is common to speak about one hole in the Cu $3d_{x^2-y^2}$ orbital. If we now add another hole the strong Coulomb repulsion between two holes in the $d_{x^2-y^2}$ orbital effectively makes the hole go into the oxygen p-orbitals and form a Zhang-Rice-singlet state [Zhang 1988] with the hole on the Cu $3d_{x^2-y^2}$ orbital. This state is centered on the Cu ion and adding a hole to form such a singlet can be interpreted as adding a hole into a lower Hubbard band of a Hubbard model with lattice sites on the copper coordinates only. The upper Hubbard band is formed by the states with 2 electrons on the $3d_{x^2-y^2}$ orbitals which are separated by an energy U from the singly occupied state. The charge motion now consists of position interchanges between single holes and singlet two-hole states centered on neighbored Cu sites. An effective single-hole hopping amplitude t can be obtained in second-order perturbation theory in the t_{pd}-parameter giving rise to the hybridization between oxygen and copper orbitals.

Another route to an effective one-band Hubbard model for the cuprates consists in

a systematic downfolding [Andersen 1995] of the LDA (local density approximation) band structure onto tight-binding 4-(or 8-)band Hamiltonians valid at low energy which contain e.g. the bands arising from copper $3d_{x^2-y^2}$, copper $4s$ and oxygen p_x and p_y orbitals. This multi-band Hamiltonian is then diagonalized and after Fourier-transformation the hopping parameters of an effective one-band Hamiltonian can be extracted. The Coulomb repulsion is first treated on average within LDA. After arriving at an effective one-band Hamiltonian an Hubbard on-site repulsion is then added by hand in order to include correlations beyond LDA.

1.3 Superconductivity from repulsive interactions

In the conventional BCS framework of superconductivity a phonon-mediated attractive interaction between electronic states close to the FS gives rise to a Cooper instability in the s-wave pair scattering channel at sufficiently low temperatures. In strongly correlated systems however where the Coulomb repulsion on short distances is large it is generally believed that s-wave pairing does not occur. The reason is that a pair wavefunction with s-symmetry has a non-zero amplitude for both particles being close together and this will make the paring state energetically unfavorable. Hence upon lowering the temperature and in absence of other instabilities the developing singularity in the Cooper channel mentioned in Section 1.1 will appear in another channel.

1.3.1 Unconventional pairing at weak coupling

The gap equation: At the basis of the BCS theory for superconductivity is the gap equation (see e.g. [Sigrist&Ueda 1991])

$$\Delta_{ss'}(\vec{k}) = -\sum_{\vec{k}'} \tanh\left[\frac{E_{\vec{k}'}}{2T}\right] \frac{\Delta_{ss'}(\vec{k}')}{2E_{\vec{k}'}} V(\vec{k}, -\vec{k}, -\vec{k}') \tag{1.4}$$

$\Delta_{ss'}(\vec{k})$ is the mean-field gap function for a pair $(\vec{k}, s; -\vec{k}, s')$ which has to be determined by solving (1.4). It gives rise to the gapful dispersion

$$E_{\vec{k}} = \sqrt{\epsilon_{\vec{k}}^2 + |\Delta(\vec{k})|^2}$$

for Bogoliubov quasiparticles above the ground state. The Pauli principle enforces $\Delta_{ss'}(\vec{k}) = -\Delta_{s's}(-\vec{k})$. In singlet superconductors this can be fulfilled through a gap function which is even with respect to $\vec{k} \to -\vec{k}$ and antisymmetric in spin space, while for a triplet BCS state $\Delta_{ss'}(\vec{k})$ is odd in $\vec{k}$-space and symmetric in spin space. Further in writing Eq. (1.4) we have assumed spin independent interactions (see e.g. Eq. (3.46)) where the interaction function $V(\vec{k}, -\vec{k}, -\vec{k}')$ denotes the pair scattering matrix element $V_{s-ss-s}(\vec{k}, -\vec{k}, \vec{k}', -\vec{k}')$.

To show the main aspects let us confine the analysis to gap functions

$$\Delta_{ss'}(\vec{k}) = \Delta_{l,ss'}\eta_l(\vec{k})$$

which transform according to a single one-dimensional irreducible representation l of the symmetry group of the crystal. $\eta_l(\vec{k})$ denote normalized basis functions of the different representations, orthogonal to basis functions of the same and other representations.

Further we assume pair scattering matrix elements which can be decomposed in a simple product[11]

$$V(\vec{k}, -\vec{k}, \vec{k}') = \sum_{l'} V_{l'}\eta_{l'}(\vec{k})\eta^*_{l'}(\vec{k}') \,.$$

Then the gap equation (1.4) (suppressing the spin indices) becomes

$$\Delta_l\eta_l(\vec{k}) = -\sum_{\substack{\vec{k}' \\ l'}} \tanh\left[\frac{E_{\vec{k}'}}{2T}\right] V_{l'}\eta_{l'}(\vec{k})\eta^*_{l'}(\vec{k}')\,\frac{\Delta_l}{2E_{\vec{k}'}}\eta_l(\vec{k}') \,.$$

When we perform the angular integral over the FS, all terms with $l' \neq l$ drop out[12]. This has the immediate consequence that a solution $\Delta_l(\vec{k})$ of (1.4) transforming according to a certain representation l is independent of the $V_{l'}$ for $l' \neq l$. For $l' = l$ we have

$$1 = -V_l \sum_{\vec{k}'} \tanh\left[\frac{E_{\vec{k}'}}{2T}\right] \frac{|\eta_l(\vec{k}')|^2}{2E_{\vec{k}'}} \,. \tag{1.5}$$

The sum on the right hand side is positive. Thus for a non-trivial solution of the gap equation it is sufficient that one V_l for a certain representation is negative, the components of the pair scattering belonging to other representations do not matter. The decoupling of the different representation implies in particular that the isotropic on-site Coulomb repulsion does not impede pairing in a higher angular momentum channel. If more than one V_l become attractive, the instability will in general occur in the channel with the most negative coefficient for the energy gain is largest there.

Corrections to the pair scattering: Next we describe how such an attractive V_l can occur in a model with repulsive electron-electron interactions. Kohn and Luttinger [Kohn&Luttinger 1965] analyzed all second order corrections to $V(\vec{k}, -\vec{k}, \vec{k}')$ given by the particle-hole diagrams in Fig. 3.2 for a spherically symmetric system with non-local interactions. They realized that due to the singular slope of the particle-hole bubble at

[11] For simplicity we assume that all the η_ls occurring in the pair scattering belong to different irreducible representations. If there are several basis functions η_l from the same representation, the solution of the gap equation at $T < T_c$ will generally be given by a superposition of these different basis functions.

[12] Note that $\tanh\left[\frac{E_{\vec{k}'}}{2T}\right]/E_{\vec{k}'}$ transforms according to the trivial representation, therefore the angular integral vanishes for $l \neq l'$ due to the different symmetries of the η_ls.

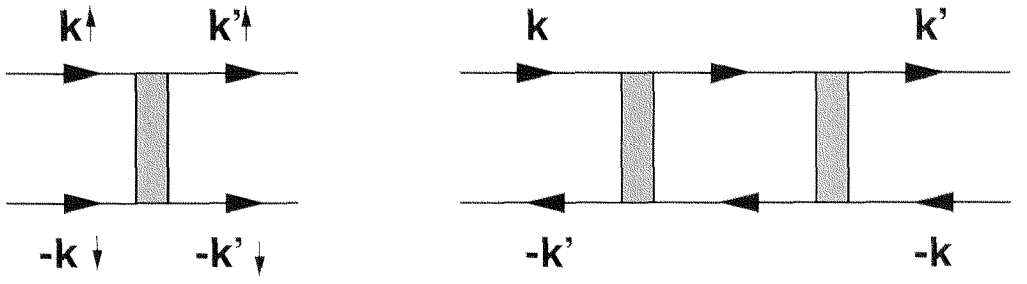

Figure 1.4: *Left: The pair scattering matrix element* $V_{s-ss-s}(\vec{k},-\vec{k},\vec{k}',-\vec{k}') = V(\vec{k},-\vec{k},\vec{k}')$. *Right: Correction to the pair scattering* $V(\vec{k},-\vec{k},\vec{k}')$ *through the crossed particle-hole second order diagram. The spin component has to be conserved at the short sides of the rectangles representing the interaction function* $V(\vec{k},-\vec{k},\vec{k}')$.

$2k_F$ the Legendre coefficients V_l of the second order corrections which are negative for odd l drop off slower ($\sim 1/l^4$) for large angular momentum than the coefficients for the first order pair scattering which fall off exponentially. Thus for sufficiently high angular momentum l the effective pair scattering becomes negative.

For local interactions like the Hubbard interaction the first order pair scattering only has a repulsive s-wave component, and three of the four second order particle-hole diagrams cancel each other, only the crossed particle-hole diagram remains, shown in Fig. 1.4. This gives rise to a correction[13]

$$\delta V(\vec{k},-\vec{k},\vec{k}') = -U^2 \chi_{\rm PH}(\vec{k}+\vec{k}') \tag{1.6}$$

to the scattering element between pairs $(\vec{k},-\vec{k})$ and $(\vec{k}',-\vec{k}')$. Therefore the particle-hole bubble $\chi_{\rm PH}(\vec{k}+\vec{k}') < 0$ will generate an anisotropic component in the pair scattering and depending on its structure this will allow the solution of (1.4) for an appropriate symmetry of $\Delta_{ss'}(\vec{k})$. Expression (1.6) has been used for the analysis of superconducting instabilities in the Hubbard model at low electron densities ([Baranov 1992, Hlubina 1997]). Of course non-local interactions e.g. arising from spin-fluctuations could yield expressions equivalent to (1.6).

Next we describe two simple and quite different examples where (1.6) generates an anisotropic component in the pair scattering with the right sign.

p-wave component: The first example is a spherical Fermi surface in three dimensions. Here $|\chi_{\rm PH}(\vec{q})|$ is peaked at $\vec{q}=0$ where it equals the density of states. This means that the pair scattering $V(\vec{k},-\vec{k},\vec{k}')$ at $\vec{k}=-\vec{k}'$, i.e. $|\vec{q}|\approx 0$, will be increased with respect to its value at $\vec{k}=\vec{k}'$, for which $|\vec{q}|\approx 2k_F$. This is equivalent to a non-zero p-wave component in the pair scattering in which $V(\vec{k},-\vec{k},\vec{k})<0$ and $V(\vec{k},-\vec{k},-\vec{k})<0$. Note

[13]The "-" in this expression comes because we calculate a second order correction to a first order matrix element, hence we get only one minus sign.

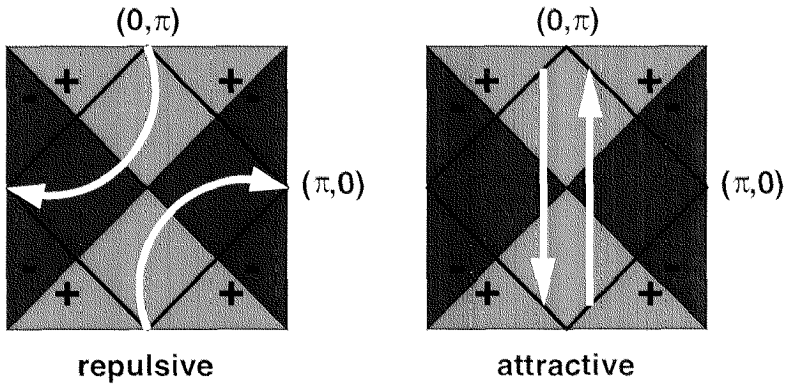

Figure 1.5: *Pair scattering for the $d_{x^2-y^2}$-symmetry. The square FS of the half-filled Hubbard model is shown as the dark line. A part of the repulsive processes involves momentum transfer $\approx (\pi, \pi)$.*

that the pair scattering still possesses the full rotational symmetry when we transform $\vec{k}$ and $\vec{k}'$ simultaneously. This suggests that an isotropic gap (like the Balian-Werthamer state) will maximize the condensation energy. The energy scale of such a p-wave instability may be extremely small, mainly because $\chi_{\rm PH}(\vec{q})$ is only weakly peaked at $\vec{q} = 0$.

d-wave component: The second example is crucial for the $d_{x^2-y^2}$-wave superconductivity in weak-coupling approaches to the two-dimensional Hubbard model. There close to half-filling $\chi_{\rm PH}(\vec{q})$ is strongly peaked at $\vec{q} = (\pi, \pi)$. Let us consider $\vec{k}$ close to the saddle points $(0, \pi)$ and $(\pi, 0)$ (see Fig. 1.5). Then for $\vec{k}'$ close to the other saddle point $\vec{k} + \vec{k}' \approx (\pi, \pi)$ and (1.6) will strongly enhance the corresponding pair scattering processes. For $\vec{k}$ and $\vec{k}'$ at the same saddle point the contribution from (1.6) will be small. As one can see from Fig. 1.5 this imbalance is also true to a somewhat reduced degree for pair scattering processes away from the saddle points: for processes with initial and final pairs in the different regions (of the "+" or the "-"-regions in the BZ) the momentum transfer $\vec{k} + \vec{k}'$ is always closer to (π, π) than for pair scattering processes inside the "+" or "-" regions.

Subtracting the average pair scattering we obtain a $d_{x^2-y^2}$ component. Its magnitude is coupled to the height of the peak of $\chi_{\rm PH}(\vec{q})$ at $\vec{q} = (\pi, \pi)$. This time the pair scattering is pinned to the lattice and obeys the four-fold rotational symmetry of the square lattice.

A priori the energy scale of this $d_{x^2-y^2}$-Cooper instability need not be small, after all in the $t' = 0$ Hubbard model the particle-hole bubble $\chi_{\rm PH}(\vec{q})$ at $\vec{q} = \vec{Q}$ diverges when we approach half-filling. This however can generate a much stronger singularity than the one in the d-wave channel, namely the antiferromagnetic or SDW (spin density wave) instability. If this instability does not occur because it is cut off at low scales or prevented by some other reason, the generated $d_{x^2-y^2}$ component diverging at low scales can be regarded as spin-fluctuation induced. We note that already before high-T_c Scalapino et

al. [Scalapino 1986] summed the paramagnon ladder diagrams made from $\chi_{\rm PH}(\pi,\pi)$ to obtain an attractive $d_{x^2-y^2}$ component for the 3D Hubbard model and pointed out its sensitivity to band structure and filling.

In the RG analysis it turns out that for the flat FS the AF processes suppress the d-wave channel in the same way as they drive it, mainly because all processes which exchange particles between two opposite sides of the FS flow to strong repulsion, and this also includes pair processes which should become attractive for $d_{x^2-y^2}$-wave symmetry.

We will use the term "Kohn-Luttinger superconductivity" when (1.6) or analogous mechanisms generate a finite attractive component $V_l < 0$ in the pair scattering and the Cooper processes of this unconventional channel l are the only processes which flow to strong coupling.

The situation will be different in the so-called saddle point regime described in Chapter 5. There the FS is curved and the main scattering processes occur between the saddle point regions. The RG analogue of (1.6) will serve as the main building block of the mutual reinforcement between d-wave Cooper and (π,π)-AF channel, leading to a high critical scale where both d-wave and AF processes diverge. This means that already without taking into account the particle-particle channel $V_{d-\rm wave} \to -\infty$, i.e. the $d_{x^2-y^2}$ component in the pair scattering is generated by processes which are singular themselves. Then of course the resulting instability is more complex and does not describe a pure d-wave Cooper instability.

1.3.2 d-wave superconductivity at strong coupling

Short range singlet pairing appears to be natural in the Hubbard model with $U/t \gg 1$ because singlets between electrons on neighboring lattice sites maximize the energy gain through the effective Heisenberg interaction on a single bond. Since the discovery of high temperature superconductivity there have been numerous studies[Dagotto 1994] analyzing the existence or non-existence of long-range d-wave pair correlations in the two-dimensional Hubbard and t-J model. However the typical numerical methods appropriate for the strong coupling region are confronted with difficulties like the sign problem (QMC), finite size effects (exact diagonalization) or cannot reach the relevant temperature and energy scales. Therefore the search for d-wave superconductivity in the Hubbard model is still a topic of ongoing research.

By combining variational Montecarlo on Gutzwiller wavefunctions with Lanczos iterations to improve the short-range behavior, Heeb [Heeb 1994] found a parameter region with stable $d_{x^2-y^2}$ superconducting long range order in the two-dimensional t-J model. These methods have recently been improved and extended by Becca et al. [Becca 2000], further supporting the existence of d-wave superconductivity in the t-J model. Moreover for the lightly doped t-J-model at $J/t = 0.4$ fixed node and Green's function Montecarlo methods[Calandra 2000] gave finite values for the d-wave pairing amplitude

extrapolated to infinite system size. Nevertheless the situation is far form being clear as there are other competing instabilities such as stripe formation [White 2000].

Recently two groups [Maier 2000, Liechtenstein 1999], , using cluster DMFT schemes, found stable off-diagonal components with $d_{x^2-y^2}$ symmetry in a selfenergy heavily coarse-grained in $\vec{k}$-space for the two-dimensional Hubbard model at $U/t = 12t$. The superconducting T_c shows a doping dependence very similar to the behavior observed experimentally in the cuprates.

Chapter 2

The Half-Filled Two-Leg Ladder and the Two-Patch Model

In this chapter we analyze the RG flow to strong coupling in the half-filled two-leg ladder and a simplified version of the two-dimensional problem, the so-called two-patch model. Both serve as toy models for the RG treatment of the full two-dimensional Hubbard model described in later chapters which help us to understand the main processes in a mostly analytical way. We will discuss how the reinforcing coupling between Cooper and antiferromagnetic channel yields an unusual flow to strong coupling and emphasize the role of Umklapp processes in creating this coupling and driving the system towards an incompressible, i.e. charge gapped state. First we review some general facts about ladder systems.

2.1 Spin-$\frac{1}{2}$ ladders

Ladder systems have attracted considerable interest over the last years (for a review see [Dagotto&Rice 1996]), mainly because they represent simpler models exhibiting strong correlation effects and magnetic phenomena similar to those in the two-dimensional high-T_c cuprates. From a theoretical point of view ladder systems are more convenient to analyze because one can make use of the large number of analytical (bosonization, conformal field theories, Bethe-Ansatz, etc.) and numerical (quantum Montecarlo, exact diagonalization, DMRG, etc.) methods which exclusively or most efficiently work in quasi-1D systems. However the low dimensionality seems to increase the complexity, as rather stable concepts like the Landau-Fermi liquid and the confinement of spin and charge break down and the variety of possible ground states becomes large.

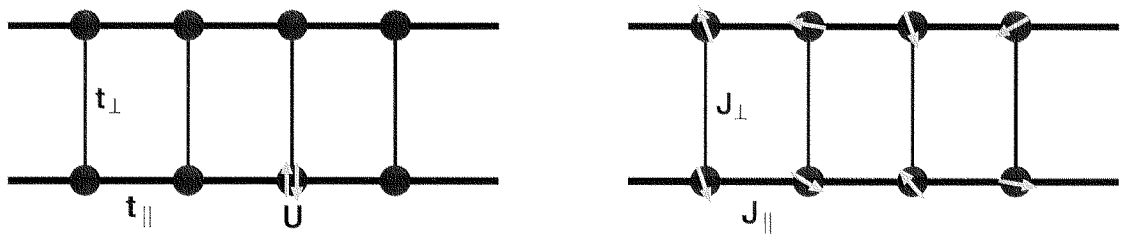

Figure 2.1: *Left: Hubbard two-leg ladder. Right: Heisenberg two-leg ladder.*

2.1.1 Half-filled two-leg ladders: the insulating spin liquid

First we want to focus on the half-filled two-leg Hubbard ladder which shall be the first toy model for the RG analysis of the two-dimensional Hubbard model. From the weak coupling (U/t small) side, two-leg Hubbard ladder systems have been extensively analyzed with combined RG and bosonization techniques [Schulz 1996, Balents 1996, Lin 1998, Fisher 1998]. The main result, parts of which we will reproduce in the next section, is that at half-filling the groundstate of the system has a fully gapped spectrum where adding a particle or creating an $S = 1$ excitation requires a finite amount of energy. Further the ground state is characterized by strong $d_{x^2-y^2}$-wave pairing (appropriately defined on the ladder) and AF fluctuations. This paired incompressible state is called an *insulating spin liquid* (ISL).

Another remarkable feature of the two-leg ladder systems is the continuous evolution of this singlet groundstate from weak to strong coupling ($U/t \gg 1$) where it can be interpreted as a RVB type spin liquid similar to the RVB state originally proposed by Anderson for the two-dimensional Heisenberg model.

Although it is relatively easy to understand that Heisenberg spin ladders with dominant coupling along the rungs ($J_\perp \gg J_\parallel$) have a spin gap, it came as a surprise that this spin liquid ground state persists [Dagotto 1992, Dagotto&Rice 1996] down to the isotropic Heisenberg ladder case ($J_\perp = J_\parallel = J$) which corresponds to the strong coupling ($J = t^2/4U$) limit of the Hubbard two-leg ladder. In fact the spin gap only disappears in the limit $J_\perp/J_\parallel \to 0$, where the two legs decouple into separate Heisenberg chains, which have a gapless spectrum as already found by Bethe in 1931 (see e.g. [Fradkin 1991]) and ensured by the Lieb-Schulz-Mattis theorem [LSM 1961].

2.1.2 Adding holes: a 1D d-wave superconductor

Upon doping holes into the half-filled two-leg ladder, analytical [Balents 1996] and DMRG [Noack 1994] calculations for the Hubbard two-leg ladder suggest that the system goes into a state analogous to the Luther-Emery liquid in a single chain with attractive backscattering ([Luther&Emery 1974], for a review on 1D systems see [Voit 1994]),

which still exhibits a spin gap and where the holes enter in pairs forming a one-dimensional superconductor with power-law $d_{x^2-y^2}$-wave pairing correlations. The same behavior had been predicted and found for doped two-leg t-J ladders on various ways ([Rice 1993, Sigrist 1994, Troyer 1996], see also [Schulz 1999]). Like in many scenarios for the two-dimensional cuprates, the vicinity to the Mott state drives the system towards an unconventional singlet pairing state. This contrasts with the doped single chain with repulsive interaction, where unconventional pairing in the singlet channel is impossible, and the groundstate is a Luttinger liquid without spin gap.

2.1.3 Adding legs: FS truncation

Hubbard ladders with more than two legs have also been considered extensively (see e.g. [Dagotto&Rice 1996]). At half-filling one finds a general odd-even effect: ladders with an even number of legs have a spin gap, while ladders with an odd number of legs maintain one gapless spin mode. Formally the difference in the spectra of the low-lying spin excitation between an odd and even number of legs can be understood due to the existence or absence of a topological term in the effective action for the continuum spin model [Khveshchenko 1994, Haldane 1983]. Further in weak-coupling RG treatments one finds a hierarchy of energy scales and critical dopings for the disappearance of the charge gap on pairs of legs when the particle density is decreased away from half-filling: the pairs of legs with smallest Fermi velocity have the largest charge gap [Ledermann 2000]. Hence upon doping the holes enter the bands with the smallest gaps first while the charge gap in the other bands persists. This is consistent with numerical results on three-leg t-J ladders which show that upon doping the half-filled three-leg ladder the holes go into the unpaired odd-parity band, while the particle number in the outer spin-gapped bands stays pinned to half-filling [Rice 1997]. Thus in these lightly doped systems there exists an intermediate state between the Mott insulator at half-filling and the Luther-Emery state with gapless charge excitations further away from half-filling. This intermediate state has a *truncated Fermi surface* in the sense that there is a coexistence of bands with gapful and bands with gapless charge excitations.

2.2 RG treatment of the 2-leg ladder at half-filling

The two-leg Hubbard ladder at weak coupling has been thoroughly analyzed by many authors [Fabrizio 1993, Khveshchenko 1994, Schulz 1996, Balents 1996, Lin 1998]. Here we repeat parts of the analysis using a renormalization group language which is closest to our study of the two-dimensional Hubbard model and introduce the main features of the RG flow towards the ISL. The two-leg Hubbard ladder with equal nearest neighbor

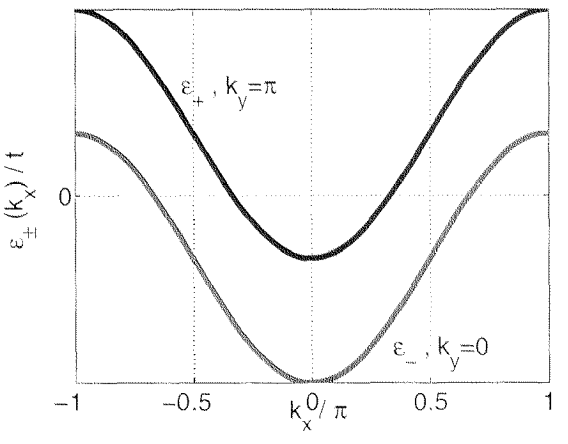

Figure 2.2: *Free dispersion of the two-leg Hubbard ladder at half-filling ($\mu = 0$). The Fermi wavevectors of the two bands add up to π.*

hopping t along and between the legs is described by the Hamiltonian

$$H = -t\left[\sum_x \left(c^\dagger_{x,1}c_{x,2} + c^\dagger_{x,2}c_{x,1}\right) + \sum_{x,i=1,2}\left(c^\dagger_{x+1,i}c_{x,i} + c^\dagger_{x,i}c_{x+1,i}\right)\right] + U\sum_{x,i} n_{x,i,\uparrow}n_{x,i,\downarrow}\,. \tag{2.1}$$

Here, $i = 1, 2$ labels the two legs and $U > 0$ is the on-site Coulomb repulsion. The non-interacting model has two bands (bonding and anti-bonding) with dispersion

$$\epsilon_\pm(k_x) = \pm t - 2t\cos k_x\,. \tag{2.2}$$

The wavefunctions in these two bands have different parity with respect to interchange of the ladders, therefore we can attribute transverse wavevectors $k_y = \pi$ and $k_y = 0$ to the $+$ and $-$ band, respectively. The system is half-filled with one electron per site if the chemical potential is at $\mu = 0$. Then the Fermi wavevectors of the two bands add up to π with the important implication that Umklapp processes where two particles scatter from the Fermi points on e.g. the right branches of the dispersion curves to the left branches become elastic.

2.2.1 The one-loop flow of the coupling constants

The influences of a small positive U shall be analyzed within a one-loop RG scheme basically equivalent to the one discussed in the following chapter. However to keep it simple for the time being we select the relevant channels where logarithmic infrared

divergences occur in a perturbation expansion. These are the Cooper channel, i.e. the particle-particle diagrams where the two incoming wavevectors add up to zero (modulo reciprocal lattice vectors), and - typical for 1D systems - the $2k_F$ particle-hole channel, which in our case includes all particle-hole loops with either $2k_{F+}$, $2k_{F-}$ or $k_{F+}+k_{F-}$ momentum transfer flowing through. All these diagrams have an arbitrarily small energy denominator and diverge logarithmically $\propto \log(\Lambda_0/\Lambda)$ when we decrease the infrared cutoff Λ starting from some high value Λ_0. Correspondingly the leading corrections to the bare interactions will be given by these contributions and a first RG analysis can be restricted to the scattering processes for particles close to the different Fermi points which couple to these dominant fluctuations. At half-filling we find 9 of these superficially relevant processes which are represented graphically in Fig. 2.3.

Away from half-filling the g_3-type processes g_{3e}, g_{3c} and g_{3x} become inelastic because the absolute values of the Fermi wavevectors of the two bands do no longer add up to π. Therefore the g_3-type processes do not enter the physics at lowest energy scales. Note however that close to half-filling they still grow strongly at intermediate energy scales are only cut off below a certain threshold energy related to the distance to half-filling. The true low energy physics should then be determined taking into account these large but non-divergent g_3-Umklapp contributions. This represents a severe problem as close to half-filling the Umklapp processes will exceed the perturbative range. Here we will restrict the analysis to the case at half-filling, where the g_3-type processes diverge and drive the system towards an incompressible state, and to densities further away from half-filling, where the g_3-Umklapp processes remain small and the compressibility remains unrenormalized.

With a linearized dispersion around the Fermi points and in the units of $v_{F\pm}\pi = 1$ (such that the DOS per band and spin orientation is unity) we can straightforwardly write down the one-loop RG equations [Furukawa]($\dot{g} = \Lambda dg/d\Lambda$ and Λ decreasing from an initial energy scale Λ_c):

$$\begin{aligned}
\dot{g}_{1x} &= \left(g_{1x}^2 + g_{2y}g_{1p} + g_{3x}^2 - g_{3x}g_{3c}\right)\\
\dot{g}_{2x} &= \frac{1}{2}\left(g_{1x}^2 + g_{2y}^2 + g_{1p}^2 - g_{3c}^2\right)\\
\dot{g}_{3x} &= 2g_{1x}g_{3x} - g_{1x}g_{3c} - g_{2x}g_{3x} - g_{2e}g_{3x} - g_{2y}g_{3e}\\
\dot{g}_{3c} &= 2g_{1e}g_{3c} + g_{1p}g_{3e} - g_{1e}g_{3x} - g_{2y}g_{3e} - g_{2e}g_{3c} - g_{2x}g_{3c}\\
\dot{g}_{2y} &= g_{1x}g_{1p} + g_{2y}g_{2x} - g_{2y}g_{2e} - g_{3c}g_{3x}\\
\dot{g}_{1p} &= 2g_{1e}g_{1p} + g_{1x}g_{2y} - g_{1e}g_{2y} + g_{1p}g_{2x} - g_{1p}g_{2e} + g_{3e}g_{3c} - g_{3e}g_{3x}\\
\dot{g}_{1e} &= g_{1e}^2 + g_{1p}^2 - g_{2y}g_{1p} + g_{3c}^2 - g_{3c}g_{3x}\\
\dot{g}_{2e} &= \frac{1}{2}\left(g_{1e}^2 - g_{3e}^2 - g_{3x}^2 - g_{2y}^2\right)\\
\dot{g}_{3e} &= 2g_{1p}g_{3c} + g_{1e}g_{3e} - g_{2y}g_{3c} - g_{1p}g_{3x} - g_{2y}g_{3x} - 2g_{2e}g_{3e}
\end{aligned} \tag{2.3}$$

If we could freely choose the initial conditions for the g's at Λ_0, this system of equations

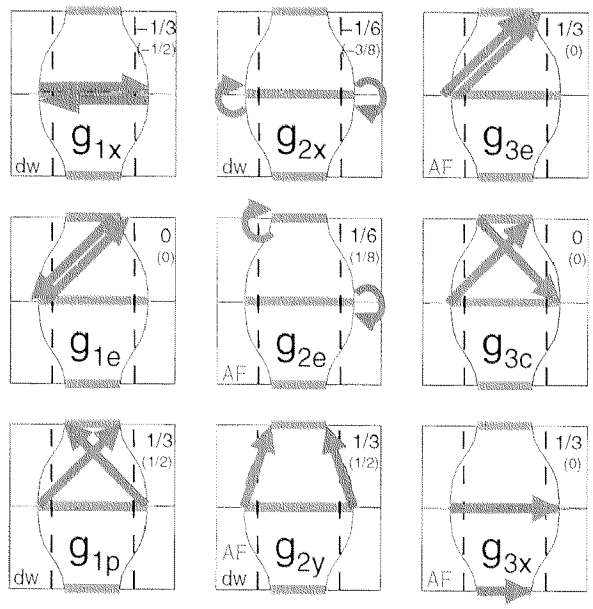

Figure 2.3: *The nine relevant couplings in the half-filled two-leg Hubbard ladder. The abbreviations "AF" and "dw" indicate whether the processes drives the AF or d-wave channel. The fractions in the upper right corners denote the asymptotic weight g_i^0 in the RG flow described in 2.4. The numbers in the brackets are the values away from half-filling where the Umklapp processes $g_{3e} = g_{3c} = g_{3x} = 0$.*

could be solved by the Ansatz

$$g_i(\Lambda) = \frac{g_i^0}{\log(\Lambda_c/\Lambda)}\,. \tag{2.4}$$

where the g_i^0's are a solution of the system (2.3) with g_i^0 replacing $\dot{g}_i$'s and g_i's everywhere. Λ_c is the scale, where all couplings diverge, its value is determined by the initial g_i's and Λ_0. For generic Hubbard interaction $g_i(\Lambda_0) = U$ however we have to perform a numerical integration of system (2.3). The result shows [Lin 1998] that the flow nonetheless is attracted to the form given in (2.4) with a particular set of g_i^0, which are [Furukawa]

$$\begin{aligned} g_{3c}^0 &= g_{3x}^0 = g_{2y}^0 = g_{1p}^0 = -g_{1x}^0 = \frac{1}{3}g_0^0\,, \\ g_{2c}^0 &= -g_{2x}^0 = \frac{1}{6}g_0^0\,, \qquad g_{3c}^0 = g_{1c}^0 = 0\,. \end{aligned} \tag{2.5}$$

g_0^0 is fixed by the initial conditions.

The divergence of the couplings means that a perturbative treatment breaks down, the system *flows to strong coupling* and the character of this flow may give at least qualitative information about the real strong coupling state. This is discussed in the following.

2.2.2 Flow of the susceptibilities

In order to obtain more information about the true strong coupling ground state it is helpful to consider the flow of several susceptibilities or the couplings to the corresponding fluctuations, respectively, as described in the next chapter. The analysis yields that the coupling to AF fluctuations $\gamma_s(\vec{Q})$ with $\vec{Q} = (\pi, \pi)$ flows with the equation

$$\frac{\dot{\gamma}_{AF}(\vec{Q})}{\gamma_{AF}(\vec{Q})} = -\frac{1}{2}\left(g_{2c} + g_{3c} + g_{3x} + g_{2y}\right) \quad \left[= -\frac{7}{12}\frac{g_0^0}{\log(\Lambda_c/\Lambda)}\right] \tag{2.6}$$

where the value in the square brackets is the asymptotic expression with values given by (2.5). Since $\dot{\gamma}_{AF}/\gamma_{AF} \to -\infty$ for Λ decreasing towards Λ_c, the coupling to AF modes and with it the AF susceptibility $\chi_s(\vec{Q})$ diverge at the critical scale.

According to the asymptotic behavior the d-wave pairing susceptibility diverges equally strongly

$$\frac{\dot{\gamma}_{dw}}{\gamma_{dw}} = \frac{1}{2}\left(g_{2x} + g_{1x} - g_{1p} - g_{2y}\right) \quad \left[= -\frac{7}{12}\frac{g_0^0}{\log(\Lambda_c/\Lambda)}\right]\,. \tag{2.7}$$

Furthermore let us consider the couplings to uniform external charges (γ_c) and spins γ_s, which determine the charge compressibility κ and the uniform spin susceptibility $\chi_s(0)$ and are renormalized by the forward scattering processes. As described in the chapter on

the RG formalism, we calculate these quantities for the effective theory below the cutoff. At a given scale, the charge coupling for electronic modes at the four Fermi points is then given by

$$\gamma_c = \frac{\gamma_{c,0}}{1 + (2g_{2e} + 2g_{2x} - g_{1e} - g_{1x})\, N_{F,b}}, \tag{2.8}$$

where $N_{F,b}$ denotes the density of states per band and spin orientation (set $= 1/2$ before) and $\gamma_{c,0}$ is the bare charge coupling. At half-filling, taking the solution (2.5), the asymptotic flow of the sum of interactions in the denominator is to $+\infty$, correspondingly the charge coupling and compressibility flows to zero. Away from half-filling, taking the asymptotic values for the couplings indicated in Fig. 2.3, the charge coupling remains unrenormalized. This shows the important role of the g_3-type Umklapp processes entering the flow at half-filling as being responsible for the charge gap tendencies.

Similarly we find for the uniform spin coupling ($\gamma_{s,0}$ denoting the bare spin coupling)

$$\gamma_s(0) = \frac{\gamma_{s,0}(0)}{1 - (g_{1e} + g_{1x})\, N_{F,b}}. \tag{2.9}$$

Again at half-filling, because g_{1x} (one of the two negative Cooper couplings) diverges to $-\infty$, γ_s and $\chi_s(0)$ flow to zero. Unlike the charge coupling, the spin coupling is still suppressed to zero away from half-filling, when we use the asymptotic values for the couplings given in Fig. 2.3: the spin gap remains as the system becomes a 1D superconductor.

Summarizing the flow of the susceptibilities at half-filling, the two-leg ladder system shows an intriguing behavior, which is referred to as insulating spin liquid (ISL): both AF and d-wave susceptibility diverge strongly, however the vanishing uniform charge and spin susceptibility indicate that spin and charge correlation functions remain purely short-ranged and that the true strong coupling ground state has no low-lying charge and spin excitation. This is unlike a superconductor where we can always add Cooper pairs at the chemical potential and also unlike a (quasi-) long-range ordered AF state which exhibits some sort of gapless magnetic excitations like spinons in the Heisenberg chain or spin waves in higher-dimensional systems. Therefore the true groundstate is not related to any kind of symmetry-broken phase and thus cannot be described by a Hartree-Fock-Bogoliubov mean-field theory.

Although this RG flow to strong coupling only indicates the way how the uncorrelated state breaks down, the qualitative picture described here can be confirmed by a bosonization analysis [Balents 1996, Lin 1998, Fisher 1998] of the effective Hamiltonian containing only the relevant couplings. In the bosonization treatment it can be clearly seen that the Umklapp processes are responsible for the charge gap, while the pairing processes open up the spin gap. At weak coupling these two gaps have the same magnitude.

Bosonization however has the drawback that it cannot be simply generalized to two dimensions[1], in which we are mainly interested. Moreover in $D \geq 2$ there are no weak

[1] Higher-dimensional bosonization [Kopietz 1997]) is exact in the limit of dominant forward scattering

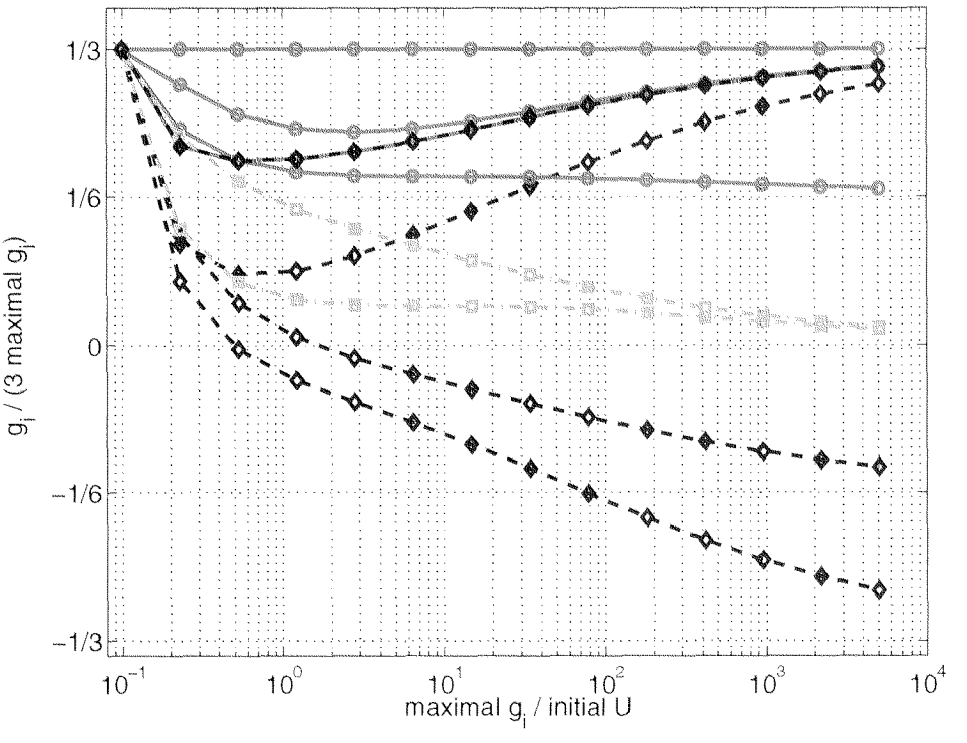

Figure 2.4: *Flow of the nine couplings versus largest coupling approaching the pole at Λ_c. The couplings are normalized with respect to largest one (g_{3c}). The solid (dashed) lines with circles (diamonds) denote processes which drive the AF (d-wave) susceptibility. The dashed-dotted lines with the squares show the irrelevant couplings which vanish in the asymptotic flow. The initial couplings at the starting scale $\Lambda_0 = 0.5t$ were $g_i = 0.1t$.*

coupling methods available which describe opening of spin and charge gaps without assuming any kind of long range order. Therefore our more modest strategy will be to understand better the particular situation leading to the RG flow described above and to search for the same conditions in the two-dimensional Hubbard model.

Another reason for this strategy arises from the numerical treatment of the two-leg ladder RG equations for realistic parameters, described in the next subsection.

2.2.3 Numerical integration of the RG flow

We discuss the numerical integration of the RG equations (2.3) for the following parameters: we start the RG flow at $\Lambda_0 = 0.5t$ with initial $g_i = 0.1t$. The density of states per band from the Fermi velocity is $1/\pi v_F \approx 0.184/t$, with this we obtain a rather small critical scale of $\Lambda_c \approx 3 \cdot 10^{-13} t$.

and locally linear dispersion. Both requirements become violated in the case of the 2D Hubbard model around half-filling.

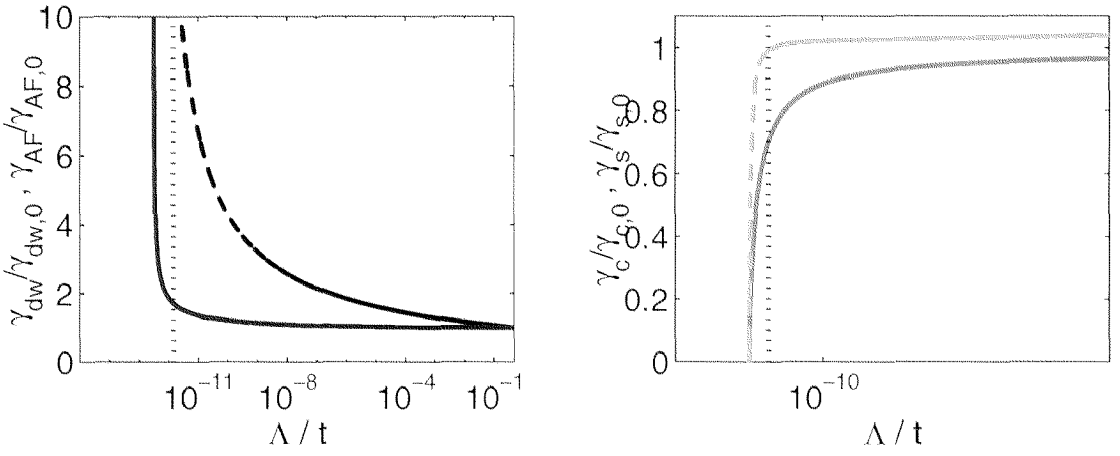

Figure 2.5: *Left plot: Divergence of d-wave coupling γ_{dw} (solid line) and AF coupling γ_{AF} (dashed line) approaching the pole at Λ_c. Right plot: Flow of charge coupling γ_c (solid line) and spin coupling γ_s (dashed line) for the effective theory below the cutoff normalized to their initial values $\gamma_{c,0}$ and $\gamma_{s,0}$. The vertical line signals the scale where the largest couplings exceed the bandwidth $6t$.*

The convergence of the flowing interactions towards the solution (2.5) when we integrate the flow further and further is shown in Fig. 2.4. For the given parameters the convergence to the asymptotic solution is rather slow and certainly beyond the perturbative regime. Nevertheless the tendencies are observable already when the coupling are comparable to the full bandwidth $6t$ of the system. The reason why certain couplings, namely those corresponding to pair scattering processes, reach their asymptotic flow rather late is clear: initially at $\Lambda = \Lambda_0$ all couplings are repulsive and in particular all Cooper processes are suppressed in the beginning. Only in the course of a flow an attractive d-wave component develops which then leads to the divergence of the Cooper processes to $\pm\infty$. The non-Cooper Umklapp processes like g_{3e} are not suppressed in the beginning and start to grow right from their initial values.

The numerical results for the couplings to external fields are shown in Fig. 2.5. Again we started the RG flow at $\Lambda_0 = 0.5t$ with initial $g_i = 0.1t$. The divergences of the d-wave and AF couplings γ_{dw} and γ_{AF} are very different because again the repulsive initial conditions favor the AF channel, while the d-wave component in the interaction is only generated during the flow. For these parameters the equal asymptotic growth of formulas (2.6) and (2.7) is only reached at scales where the interactions have exceeded the bandwidth by orders of magnitude. Similarly the suppression of spin and charge susceptibilities only occurs when interactions have become comparable to the full bandwidth.

Therefore for these parameters the interpretation of the RG results is somewhat problematic from only looking at the susceptibilities. Certainly we could choose a smaller initial coupling such that the asymptotic behavior is reached before the couplings leave

the perturbative region. Actually for the two-dimensional problem we will meet a flow analogous to the asymptotic behavior (2.5) of the half-filled two-leg ladder already at scales where the interactions reach values comparable to the bandwidth. Hence we can compare the two-dimensional case with moderate U to the two-leg ladder flow at very small initial U.

On the other hand from numerical treatments [Noack 1994] we know that the ISL physics in the two-leg ladder holds for stronger U as well[2]. Therefore the question arises whether at least for moderate U the ISL formation can still be understood from the one-loop flow. In the next subsection we will describe our view that this is indeed possible. We discuss how AF and d-wave processes mutually generate and reinforce each other giving rise to a combined flow towards an insulating spin liquid. Hence the question which susceptibility grows faster towards the divergence loses its importance because both tendencies are parts of a single mechanism and do not exclude each other at the ISL fixed point as it would be the case in conventional mean-field phase diagrams.

2.2.4 The mutual reinforcement mechanism in the half-filled two-leg ladder

A conventional analysis of RG flows [Solyom 1979] from weak to strong coupling compares the asymptotic growth of different susceptibilities, which then leads to a phase diagram where the strong coupling state in a certain region corresponds to a the strongest divergent susceptibility in this parameter region. This is already somewhat artificial in our case, as d-wave and AF susceptibility diverge together with the same asymptotic expression. One might think that this does not necessarily imply an unconventional state (or a new RG *fixed point*) as higher order terms and the initial conditions for the flow as described above will prefer the one or other, i.e. d-wave or AF channel. Indeed as we showed the asymptotic form is approached only slowly and depending on the initial interactions nothing guarantees that the one-loop equations are still valid until we get there. Similarly one could argue that the spin and charge gap tendencies which impede the straightforward interpretation will be cut-off at some low scale and only lead to quantitative renormalizations of the parameters of the true ground state.

On the other hand a more detailed analysis of the RG equations and the flow of the susceptibilities reveals that the flow does not describe a close competition between AF and d-wave superconducting channels, on the contrary it can be seen that here the two channels *mutually generate* and *reinforce* each other and that the spin and charge gap tendencies are inescapable consequences of this combined process.

Let us for example consider the RG equation for the coupling g_{1x} in (2.3)

$$\dot{g}_{1x} = \left(g_{1x}^2 + g_{2y}g_{1p} + g_{3x}^2 - g_{3x}g_{3c}\right) .$$

[2] Here spin and charge gap have different magnitudes and develop differently with changing U. This is also suggested by the RG for moderate U.

g_{1x} dominates the small angle Cooper pair scattering (the "−"-lobe of the d-wave). If the right hand side is positive g_{1x} will decrease when we reduce L. Apart from the last term which vanishes in the asymptotic flow, all terms on the right hand side of $\dot{g}_{1x}$ are positive, the second contains g_{2y}, the third is g_{3x}^2. These two couplings both drive the AF fluctuations (see (2.6)). Now let us assume that the AF processes flow to strong repulsion and the other processes have not changed much from their initial values. Then, due to the coupling on the right hand side of $\dot{g}_{1x}$, at least the terms containing g_{2y} and g_{3x}^2 will decrease the value of g_{1x} with decreasing Λ. This already generates an attractive d-wave component. The flow could lead to a Kohn-Luttinger-type d-wave instability at some low scale, even if the Cooper channel decoupled entirely from other processes after the initial d-wave component has been induced. This occurs away from half-filling, where the g_{3x} processes are inelastic and drop out at low energy scales. But in the present case at half-filling the flow of the attractive Cooper coupling g_{1x} even becomes enhanced through the additional driving g_{3x} term. The right hand side of the RG equation has the same form for all scales and there is *no decoupling*. If the AF processes diverge with $g_{2y} \to \infty$ and $g_{3x} \to \infty$, they necessarily drive g_{1x} to $-\infty$ and also amplify other d-wave processes even at lowest energies. Note that $g_{1x} \to -\infty$ is equivalent to spin gap tendencies, as can be seen from Eq. 2.9.

As another example take the flow of g_{3x},

$$\dot{g}_{3x} = 2g_{1x}g_{3x} - g_{1x}g_{3c} - g_{2x}g_{3x} - g_{2c}g_{3x} - g_{2y}g_{3c} \,.$$

In order to make g_{3x} and other AF couplings flow to strong repulsion, the right hand side should be negative. However for repulsive initial interactions $g_i = U$ the sum of the first two terms is positive: $g_{1x}(2g_{3x} - g_{3c})$. Now assume that the flow is such that the d-wave pair processes diverge and again the other couplings remain unchanged in the beginning. Then g_{1x} will flow to negative values, turning the sign the above $g_{1x}(2g_{3x} - g_{3c})$, so that this contribution will drive g_{3x} and along with that all other AF couplings to to strong repulsion. Again the growth of one channel, the d-wave channel in this case, generates and subsequently enhances the flow in the other channel, here in the AF channel.

Furthermore the induced divergence of g_{3x} will also drive the forward scattering to strong repulsion, hence strongly suppressing the charge compressibility. Thus at half-filling due to the coupling through Umklapp processes, a divergence of the d-wave coupling generates the tendency to open up a charge gap on the FS.

From these observations - as we mentioned earlier - the interaction between these channels is more appropriately regarded as mutual reinforcement and not as a competition: the latter would mean that a growth of one type of fluctuations suppresses the other, here the reverse is true: both kinds of fluctuation diverge together (see also Fig. 2.6) at a common critical scale much higher as the ones for the single channels.

The reason for the mutual reinforcement between d-wave and AF channel is related to the location of the Fermi points: Cooper pair scattering processes between the two bands as described by g_{2y} or g_{1p} involve a momentum change of (π, π) between the first

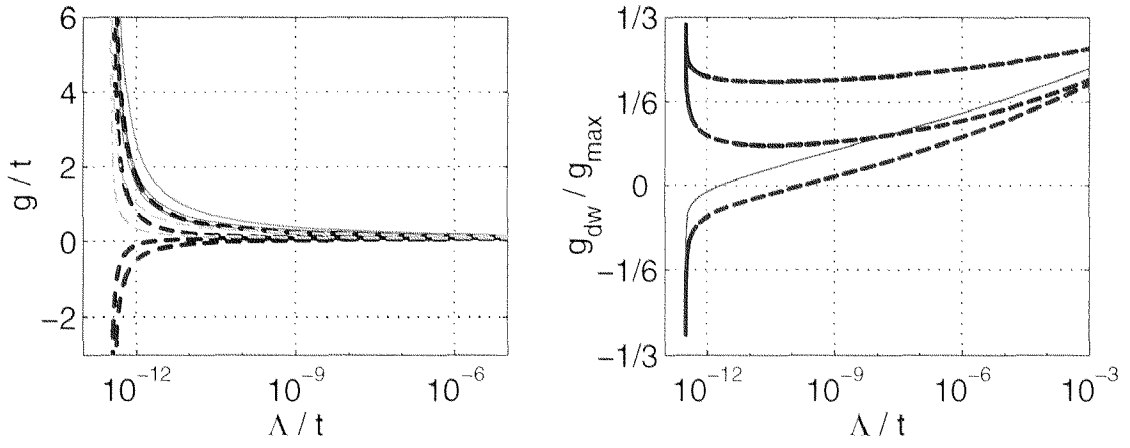

Figure 2.6: *Left plot: Flow of AF processes (solid lines) and d-wave Cooper processes (dashed lines). Both types of processes are strongly coupled in the flow and diverge together. The dashed-dotted lines denote the flow of the two irrelevant processes which vanish in the asymptotic flow. Right: Flow of the Cooper processes with respect to the largest coupling (g_{3e}) with asymptotic value* $1/3$*. The processes shown by the dashed lines have asymptotic values* $\pm 1/3$*, the solid line denotes a process with asymptotic value* $-1/6$*.*

incoming and the second outgoing particle. Therefore they couple to the AF processes which contain the same momentum transfer. Since two of these momentum transfers add up to zero, the AF Umklapp processes g_{3x} can also occur in the one-loop corrections to intraband Cooper processes g_{1x}.

On the other hand the high energy scale resulting from this mutual reinforcement comes at a price: the attractive Cooper processes g_{1x} driven to $-\infty$ by Umklapp-AF processes[3] involves g_{2y} and g_{3x}^2 inevitably causes a suppression of the uniform spin susceptibility as it increases the denominator in (2.9). Therefore as soon as the Umklapp-AF couplings grow strongly they also lead to spin gap tendencies: $\chi_s(0) \to 0$. In the second example the growth of the Umklapp-AF processes induced by the d-wave pair processes implies that g_{2e} flows to strong repulsion. Again this has an effect on the uniform susceptibilities, this time κ gets driven to zero, because the forward scattering process g_{2e} appears in the the denominator of (2.8). Again it is the coupling of d-wave and AF processes through Umklapp processes which causes a divergence in the d-wave channel and at the same time makes the system incompressible. We repeat that in the generic case away from half-filling where the Umklapp processes do not enter the low energy physics, the RG flow is towards a Luther-Emery state with diverging d-wave couplings while in this case, if we apply the same analysis without the Umklapp processes and the asymptotic values given in Fig.2.3, κ remains unrenormalized.

In the following we want to show that this complex flow to strong coupling with the key

[3] Viewed from the 2D perspective g_{2y} is an Umklapp process as well because the momentum in y-direction is only conserved after subtracting reciprocal lattice vectors.

signatures of an insulating spin liquid is also realized in a rather broad parameter range of the full two-dimensional t-t' Hubbard model. There, Umklapp scattering between Fermi surface parts close to $(\pi, 0)$ and $(0, \pi)$ again leads to a mutual reinforcement between d-wave and AF processes and the contribution of these regions to the uniform charge and spin susceptibility will become strongly suppressed. We will also show an example, namely the electron-doped side of the phase diagram, where the coupling between the channels is only weak and does not persist until the flow reaches the instability and the ISL tendencies do not occur.

2.3 The two-patch model

Two dimensions and two patches: In order to see how a strong coupling flow similar to the two-leg ladder discussed above can arise in a two-dimensional model, we give a brief discussion of the dominant mechanisms. These are most transparent in the two-patch model ([Furukawa 1998], and also [Schulz 1987, Lederer 1987]), where only small phase space patches around the saddle points at $(\pi, 0)$ and $(0, \pi)$ are kept. These Brillouin zone regions can be expected to give the leading flow if the FS is at the van Hove points. The reasons for their predominance are the large density of states and the vicinity of the FS to the so-called Umklapp surface (see Fig. 2.7), which sides are connected by $\vec{Q} = (\pi, \pi)$. If the band energy at the Umklapp surface is small, Umklapp processes between two sides provide an additional low-energy scattering channel with interesting consequences.

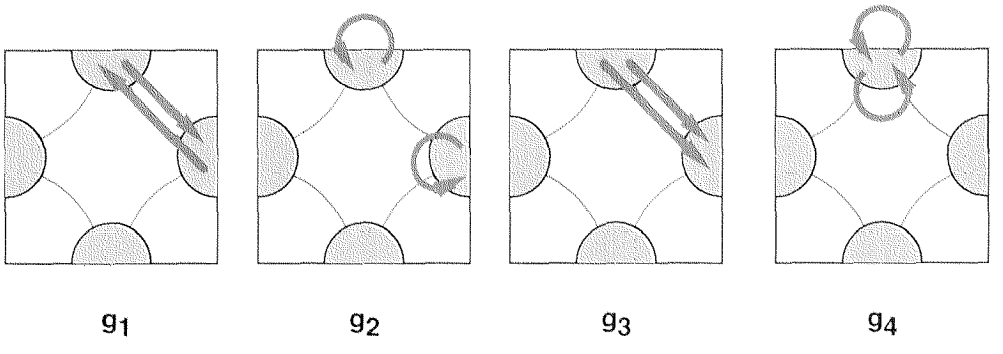

Figure 2.7: *The relevant scattering processes in the two-patch model. The gray semi-circles denote the phase space patches around the saddle points. The interactions are assumed to be spin-independent and constant over the patches. In this notation the spin of the initial and final particle connected by an arrow has to be the same.*

The RG flow: Neglecting again possible frequency dependence we can approximately describe the scattering processes within and between the two patches by four coupling constants, $g_1 \ldots g_4$, depicted in Fig. 2.7.

The main terms which drive the one-loop RG flow of these vertices are:

1. The particle-particle loop d_0 with zero total incoming momentum, which diverges like $\log^2(\Lambda_0/\Lambda)$ with decreasing energy scale $\Lambda \leq \Lambda_0$ due to the van Hove singularity in the density of states.

2. The particle-hole loop with momentum transfer (π, π) denoted by d_1 which, in presence of a small but nonzero t', diverges like $\log(\Lambda_0/\Lambda)$ with a large prefactor.

Below an energy scale determined by t'/t and μ, these terms become small compared to $\dot{d}_0$, which then dominates the flow. However if the initial coupling U is not too weak, the coupling constants diverge already above that scale.

Keeping only these two contributions, and denoting $y = \log(\Lambda_0/\Lambda)$, so that decreasing Λ means increasing y, we obtain the RG flow equations

$$\dot{g}_1 = 2\dot{d}_1 g_1 (g_2 - g_1), \tag{2.10}$$
$$\dot{g}_2 = \dot{d}_1 (g_2^2 + g_3^2), \tag{2.11}$$
$$\dot{g}_3 = -2\dot{d}_0 g_3 g_4 + 2\dot{d}_1 g_3 (2g_2 - g_1), \tag{2.12}$$
$$\dot{g}_4 = -\dot{d}_0 (g_3^2 + g_4^2). \tag{2.13}$$

where $\dot{g}_i = \partial g_i/\partial y$, and $\dot{d}_0, \dot{d}_1 \geq 0$. Next we briefly review the analysis of the two-patch model by Furukawa et al. [Furukawa 1998]. The second term on the right hand side of (2.12) enhances the basin of attraction of the strong coupling fixed point. Starting from the on-site repulsion $g_1 = g_2 = g_3 = g_4 = U$ given by (4.2), the coupling constants diverge at a scale Λ_c:

$$g_3 \to +\infty, \quad g_4 \to -\infty \quad \text{and} \quad g_2 \to +\infty, \tag{2.14}$$

g_1 diverges more slowly. Initially there is a competition between the two terms on the r.h.s. of (2.12), but the r.h.s. of (2.13) is always negative and thus decreases g_4. Eventually, g_4 becomes negative; then both terms in (2.12) have the same sign, which accelerates the flow to strong coupling.

The mutual reinforcement: For incoming and outgoing particles directly at the saddle points g_3-processes correspond to both Cooper and Umklapp processes. However, away from the saddle points we can distinguish between Cooper processes with approximately zero total incoming momentum driven through the particle-particle channel and Umklapp processes with momentum transfer $\approx (\pi, \pi)$ driven by the corresponding particle-hole channel. Taking the flow of the Cooper processes, the second term in (2.12) containing the particle-hole contributions $\propto \dot{d}_1$ is exactly the term discussed in Section 1.3.1 which creates the d-wave component in the pair scattering. The difference is here that it continues to enhance the g_3-Cooper processes down to lowest scale, such that the d-wave channel has an additional driving term. Even more, once the d-wave g_3 and g_4 processes diverge they will cause the AF processes to grow strongly as well.

From this point of view, Eq. (2.12) states that for incoming and outgoing wavevectors near the saddle points the AF and the $d_{x^2-y^2}$-wave Cooper processes are coupled and mutually reinforce each other through the g_3-processes which belong to both channels, thereby increasing the critical scale Λ_c. In fact the divergence of the Umklapp scatterings processes implies a divergence of the d-wave couplings and vice versa. Therefore we find again the mutual reinforcement between d-wave and AF tendencies.

d-wave and AF susceptibilities: An analysis of the susceptibilities shows again divergences in the $d_{x^2-y^2}$-pairing and AF channel controlled by

$$\dot{\gamma}_{dw} \propto g_3 - g_4 \tag{2.15}$$

and

$$\dot{\gamma}_{AF} \propto g_2 + g_3 \tag{2.16}$$

respectively. Again g_3 appears in both equations and we say that AF and d-wave channel have an *substantial overlap* in the sense that large contributions to their growth arise from the same g_3 processes. Correspondingly, for $g_3 \to \infty$, d-wave and AF susceptibility necessarily diverge together.

Using an ansatz similar to (2.4) for a not-too-weak value of U/t and t'/t Furukawa et al. found that the d-wave susceptibility diverged most strongly, closely followed by the AF susceptibility.

Uniform charge and spin susceptibilities: The uniform susceptibilities are renormalized by the forward scattering processes, one obtains (κ_0 is the bare compressibility)

$$\kappa = \frac{\kappa_0}{1 + (2g_2 - g_1 + g_4)N_0} \tag{2.17}$$

and ($\chi_{s,0}(0)$ is the bare uniform spin susceptibility)

$$\chi_s(0) = \frac{\chi_{s,0}(0)}{1 + (-g_1 - g_4)N_0} \tag{2.18}$$

with N_0 denoting the density of states per patch at the Fermi energy. For the same parameter values as above the combination of forward scatterings in the denominator flow to $+\infty$. Consequently, both κ and $\chi_s(0)$ are suppressed to zero. We note that while the suppression of $\chi_s(0)$, i.e. the spin gap tendency, is a direct consequence of the singlet pairing ($g_4 \to -\infty$), the charge gap arises because the diverging g_3 Umklapp processes drive the forward scattering g_2 to strong repulsion (see Eq. (2.11)). Thus the g_3 processes do not only couple AF and d-wave channel: as they are Umklapp processes as well, they also cause the opening of a charge gap on the FS.

A two-dimensional analogue of the two-leg ladder: The above analysis shows that the RG flow in two-patch model is analogous to the asymptotic behavior of the flow for the half-filled two-leg ladder. Therefore Furukawa et al. suggested that the fixed point in the two-patch model is of the same type as that of the repulsive two-leg Hubbard ladder at half-filling. The analysis of the two-patch model makes clear how a flow similar to the one in the half-filled two-leg ladder can arise in the two-dimensional t-t'-Hubbard model. The central ingredient of the flow to the ISL, the coupling of d-wave and AF

channel, is provided through Umklapp processes at the saddle points. However in the two-patch model the influence the FS parts away from the saddle point regions is not taken into account and it is not obvious that the coupling between the channels remains in a less coarse-grained description of the scattering processes. The main result of the following N-patch study will be that one can indeed identify parameter regions where the strong coupling flow exhibits the key properties of the asymptotic flow found for the half-filled two-leg Hubbard ladder, thus suggesting an ISL formation around the saddle points.

Chapter 3

The RG Formalism

In this chapter we describe the renormalization group (RG) formalism for the one-particle-irreducible (1PI) vertex functions which will be used for the analysis of the two-dimensional Hubbard model. We discuss the approximations made and comment on other RG approaches.

3.1 Wilsonian RG

Renormalization group techniques are widely used in theoretical physics and have besides their calculational successes (outside particle physics e.g. [Wilson&Fisher 1972, Wilson 1975]) led to new and quite far-reaching ideas about the status and validity of important theoretical concepts like the standard model of elementary particles or the Landau-Fermi liquid in condensed matter systems.

While in the 1950s *renormalization group* methods were initially introduced by Gell-Mann and Low [Gell-Mann 1954] and independently by Stückelberg and Petermann [Stückelberg 1953] in order to analyze the structure of quantum-field theories plagued by infinities like QED (see e.g. [Weinberg 1997]), the *Wilsonian* renormalization group introduced by K.G. Wilson in the first half of the 1970s[1] is a more general concept which proved very useful even on a less technical and intuitive level.

Although there is much more to say about Wilsonian RG, in particular in connection with phase transitions and statistical mechanics (for a recent and very readable review, see [M.E.Fisher 1998]), let us focus here on its importance in the interacting electron problem in condensed matter physics. There one is typically interested in low-energy and long-wavelength properties of the system, like the nature of the groundstate and the excitations above the latter. When applying perturbation theory in the particle-particle

[1]The idea of obtaining a long-range theory by reducing the degrees of freedom by integrating out the short-range processes ("block spins") had been introduced before by Kadanoff (see e.g. [M.E.Fisher 1998].

interactions one is first confronted with a large number of intermediate processes and different classes of diagrams to be summed and second typically encounters infinities, e.g. in second order diagrams for particular values of the external momenta and frequencies. The latter are infrared singularities and arise because the bare single-particle Green's function

$$G_2^0(\vec{k}, i\omega_n) = \frac{1}{i\omega_n - \epsilon(\vec{k})}$$

is singular on the Fermi surface for $T \to 0$. For both problems the Wilsonian strategy of successively integrating out higher energy excitations proves very useful. First one approaches the singularities at low energy scales in a controlled way by keeping a non-zero infrared cutoff. Second in the course of successive mode elimination it typically becomes clear which processes are *relevant*, i.e. determine the physical behavior at low energy scales or in the groundstate, and which interactions are *irrelevant*, as they become less important when we further decrease the energy scale. Therefore Wilson's RG is a powerful scheme for determining the *effective low energy theory* of a system initially containing more degrees of freedom at many energy scales.

The most common effective theory in condensed matter physics, the Landau-Fermi liquid, had however been formulated much earlier without explicit use of RG ideas. Also before the development of Wilson's RG and its modern formulations, similar strategies like poor man's scaling (briefly described in a later section) and "field-theoretic" renormalization (reviewed in [Solyom 1979]) had already led to the idea that the different possible ground states can be understood as distinct scaling trajectories of the system parameters (later related to fixed points of the RG transformation). However these approaches usually require particular conditions like scale-invariance, renormalizibility and a clear separation of energy scales and their structure gets rather involved for general problems. The renormalization group formulation of Wilson based on the invariance of the system's partition function with respect to performing partial traces over certain subspaces provides a more robust and straightforwardly generalizable way for arriving at an effective theory. Its importance for condensed matter physics has recently been highlighted in [Shankar 1994]. Here we will however not use his terminology but present in this chapter a more general and precise formalism, mainly developed by M.Salmhofer and described briefly in [HSFR 1999].

3.2 The formal objects

Here we introduce the formal object which occur in the derivation of the RG equations.

Grassmann variables: The field theory of the electronic system will be expressed in terms of anti-commuting Grassmann variables $\psi(X) = \psi(\vec{x}, \tau, s)$ and $\bar{\psi}(X)$ (for an introduction, see e.g. [Negele&Orland 1988]) which live in imaginary time τ on lattice

sites labeled by $\vec{x}$, s is the spin index. We take care of the fermionic nature of the electrons by imposing the boundary conditions

$$\begin{aligned} \psi(\vec{x}, \tau + \beta) &= -\psi(\vec{x}, \tau) \\ \bar{\psi}(\vec{x}, \tau + \beta) &= -\bar{\psi}(\vec{x}, \tau) , \end{aligned}$$

where $\beta = 1/T$ is the inverse temperature Apart from the ψ-fields we will use fermionic source fields represented by Grassmann variables η and $\bar{\eta}$. Further it is convenient to introduce a antisymmetric bilinear form

$$(\eta, \psi) = \sum_{\vec{x},\tau,s} \eta(\vec{x}, \tau, s)\psi(\vec{x}, \tau, s) . \tag{3.1}$$

The action: In real space and imaginary time the quadratic "free" part of the action of the physical system shall be given by

$$\mathcal{A}_2 = \int_0^\beta d\tau \sum_{\vec{x},\vec{y}} \bar{\psi}(\vec{x}, \tau) \left[\delta_{\vec{x},\vec{y}}(\partial_\tau - \mu) + t_{\vec{x},\vec{y}}\right] \psi(\vec{y}, \tau) \tag{3.2}$$

Here, $t_{\vec{x},\vec{y}}$ denotes the hopping from site $\vec{x}$ to site $\vec{y}$ and μ is the chemical potential. The above form of $\mathcal{A}_2$ is the typical situation we are interested in. The formalism, however, can be applied to a much wider range of actions. The same holds for the interaction between the fermions which we choose to be instantaneous and of density-density type

$$\mathcal{A}_4 = \int_0^\beta d\tau \sum_{\substack{\vec{x},\vec{y} \\ s,s'}} \bar{\psi}_s(\vec{x}, \tau)\psi_s(\vec{x}, \tau)V_{s,s'}(\vec{x}, \vec{y})\bar{\psi}_{s'}(\vec{y}, \tau)\psi_{s'}(\vec{y}, \tau) , \tag{3.3}$$

with e.g. $V_{s,s'}(\vec{x}, \vec{y}) = \frac{U}{2}\delta_{\vec{x},\vec{y}}$ for the Hubbard model. After transforming to frequency and momentum space using

$$\psi(\vec{x}, \tau) = T \sum_{i\omega_n} \int \frac{d\vec{k}}{(2\pi)^D} e^{i(\omega_n \tau - \vec{k}\vec{x})} \psi(\vec{k}, i\omega_n) , \tag{3.4}$$

with $\omega_n = \pi T(2n + 1)$, n integer, the quadratic part reads

$$\mathcal{A}_2 = T \sum_{i\omega_n} \int \frac{d\vec{k}}{(2\pi)^D} \bar{\psi}(\vec{k}, i\omega_n) \left[i\omega_n - \epsilon(\vec{k})\right] \psi(\vec{k}, i\omega_n) . \tag{3.5}$$

The kernel $\left[i\omega_n - \epsilon(\vec{k})\right]$ is also called $Q(\vec{k}, i\omega, s)$ and will be eventually supplemented with a cutoff function making it operate on fields with in a certain energy range only.

The Fourier-transform of the interactions reads

$$\mathcal{A}_4 = \frac{1}{\beta^3} \sum_{\substack{i\omega_1, i\omega_2, i\omega_3 \\ s,s'}} \int \frac{d\vec{k}_1}{(2\pi)^D} \frac{d\vec{k}_2}{(2\pi)^D} \frac{d\vec{k}_3}{(2\pi)^D} V_{s,s'}(\vec{k}_1, \vec{k}_2, \vec{k}_3, i\omega_1, i\omega_2, i\omega_3)$$
$$\bar{\psi}_s(\vec{k}_1, i\omega_1)\bar{\psi}_{s'}(\vec{k}_2, i\omega_2)\psi_{s'}(\vec{k}_4, i\omega_4)\psi_s(\vec{k}_3, i\omega_4)\,, \tag{3.6}$$

where $\vec{k}_4$ and $i\omega_4$ are determined by momentum (modulo reciprocal lattice vectors) and frequency conservation. The initial interaction for the Hubbard model is momentum-independent, $V_{s,s'}(\vec{k}_1, \vec{k}_2, \vec{k}_3, i\omega_1, i\omega_2, i\omega_3) = U$, but in the course of the RG procedure, $V_{s,s'}(\vec{k}_1, \vec{k}_2, \vec{k}_3, i\omega_1, i\omega_2, i\omega_3)$ will acquire a pronounced momentum structure. Typically we will neglect the frequency dependence of the interaction.

Partition function: The partition function of the system is given by a functional integral over the Grassmann fields:

$$Z = \int d\mu_C(\psi, \bar{\psi})\, e^{-\mathcal{V}(\psi,\bar{\psi})}\,. \tag{3.7}$$

Here, $d\mu_C(\psi, \bar{\psi})$ is an abbreviation for the normalized Gaussian measure (with Q as the quadratic kernel of the free action),

$$d\mu_C(\psi, \bar{\psi}) = [\det Q(\vec{x}, \tau, s, \vec{x}, \tau, s')]^{-1} \prod_{\vec{x},\tau,s} d\bar{\psi}(\vec{x}, \tau, s) d\psi(\vec{x}, \tau, s)\, e^{-\mathcal{A}_2(\psi,\bar{\psi})}\,, \tag{3.8}$$

or in frequency-momentum space,

$$d\mu_C(\psi, \bar{\psi}) = \Big[\det Q(\vec{k}, i\omega, s)\Big]^{-1} \prod_{i\omega_n, \vec{k}} d\bar{\psi}(i\omega_n, \vec{k}) d\psi(i\omega_n, \vec{k})\, e^{-\mathcal{A}_2(\psi,\bar{\psi})} \tag{3.9}$$

where the subscript $C = Q^{-1}$ describes the covariance appearing in the exponent of the Gaussian measure.

Nambu notation At this point it is convenient to condense the notation to the so-called Nambu form. We introduce two-spinors

$$\Psi = \begin{pmatrix} \psi(\vec{x}, \tau) \\ \bar{\psi}(\vec{x}, \tau) \end{pmatrix}, \qquad H = \begin{pmatrix} \eta(\vec{x}, \tau) \\ \bar{\eta}(\vec{x}, \tau) \end{pmatrix} \tag{3.10}$$

with the bilinear form $(H, \Psi) = (\bar{\eta}, \psi) - (\eta, \bar{\psi})$. Thus e.g. $\mathcal{A}_2$ from (3.2) now reads

$$\mathcal{A}_2 = \frac{1}{2}(\Psi, \mathbf{Q}\Psi)$$

with X denoting $(\vec{x}, \tau, s)$ and

$$\mathbf{Q}(X, X') = \begin{pmatrix} 0 & \delta_{\tau,\tau'}\left[\delta_{\vec{x},\vec{x}'}(\partial_\tau - \mu) + t_{\vec{x},\vec{x}'}\right] \\ -\delta_{\tau,\tau'}\left[\delta_{\vec{x},\vec{y}}(\partial_\tau - \mu) + t_{\vec{x},\vec{x}'}\right] & 0 \end{pmatrix}$$

Here, $\mathbf{Q}\Psi(X) = \int dX' \, \mathbf{Q}(X, X')\Psi(X')$ and $\int dX = \int_0^\beta d\tau \sum_{\vec{x},s}$.

Correlation functions and generating functional: Further, for the calculation of correlation functions, it is convenient to couple fermionic source fields η, $\bar{\eta}$ to the ψ, $\bar{\psi}$-fields by writing

$$Z(H) = \int d\mu_C(\Psi) e^{-\mathcal{V}(\Psi)+(H,\Psi)} \tag{3.11}$$

The quantity

$$W(H) = -\log Z(H) \tag{3.12}$$

is the generating functional for the connected n-point correlation functions $G_n(\underline{X} = X_1, \ldots, X_n)$, obtained by

$$G_n(\underline{X}) = \prod_{j=1,\ldots,n} \frac{\delta}{\delta H(X_j)} W(H)\Big|_{H=0} . \tag{3.13}$$

Effective action: With a shift in the integration variables we can write

$$Z(H) = e^{(H,\mathbf{C}H)} \int d\mu_C(\Psi) e^{-\mathcal{V}(\Psi-\mathbf{C}H)}. \tag{3.14}$$

With another Grassmann field $\phi = C\eta$ or $\Phi = \mathbf{C}H$ we introduce the *effective action* $\mathcal{G}(C, \Phi)$:

$$e^{-\mathcal{G}(C,\Phi)} = \int d\mu_C(\Psi) \, e^{-\mathcal{V}(\Psi+\Phi)} . \tag{3.15}$$

The effective action contains the same information as the generating functional $\log Z(H)$ and can be expanded in monomials of the fields with the amputated (the new source fields are $\mathbf{C}^{-1}H$), connected n-point correlation (or Green's) functions as coefficients.

Effective potential: From the (exponentiated) generating functional for the connected and non-amputated Green's functions

$$\exp\left[-W(H)\right] = \int d\mu_{\mathbf{C}}(\Psi) \, \exp\left[-\mathcal{V}(\Psi) + (H, \Psi)\right] \tag{3.16}$$

we obtain the effective potential by taking the functional derivative with respect to the external field,

$$\Phi_{cl}(H) = \frac{\delta}{\delta H} W(H) , \tag{3.17}$$

which is the expectation value of the Ψ-field in presence of the external field H. We can also search for the external source H for a given expectation value, say Φ, i.e. solve the equation

$$\frac{\delta}{\delta H} W(H(\Phi)) = \Phi \tag{3.18}$$

and consider W as a functional of Φ.

Generating functional for 1PI vertex functions: The Legendre transform of W is defined as functional of the Φ-field,

$$\Gamma(\Phi) = W(H(\Phi)) - (H(\Phi), \Phi) \ . \tag{3.19}$$

In general we can expand Γ in monomials of the Φ-field (again with $\underline{X}$ denoting the collection of m generalized coordinates $X_1, \ldots, X_m$),

$$\Gamma(\Phi) = \sum_{m \geq 0} \frac{1}{m!} \int d^m \underline{X} \ \gamma_m(\underline{X}) \Phi^m(\underline{X}) \ . \tag{3.20}$$

The expansion coefficients $\gamma_m(\underline{X})$ are called the *one-particle-irreducible* (1PI) *m-point functions* and are fully antisymmetric under exchange of the generalized coordinates $X_1, \ldots, X_m$ due to the anticommuting Grassmann fields. In contrast with the connected correlation functions G_n the graphical representation of the γ_n does not include tree graphs and the diagrams are amputated, i.e. the external legs do not carry a bare propagator. Further by differentiating (3.18) we obtain

$$\int dZ \frac{\delta H(\Phi)(Z)}{\delta \Phi(Y)} \frac{\delta^2 W}{\delta H(Z) \delta H(X)} = \delta(X, Y) \tag{3.21}$$

and

$$\frac{\delta^2 \Gamma}{\delta \Phi^2}(\Phi) = \left[\frac{\delta^2 W}{\delta H^2}(H(\Phi)) \right]^{-1} \ , \tag{3.22}$$

where X, Y or Z stand for generalized coordinates in space-time and spin. This means that the quadratic part of the Legendre transform Γ, i.e. the two-point vertex function, is just the inverse of the full connected two-point function Green's function obtained from $\delta^2 W(H)/\delta H(X) \delta H(Y)$.

The four-point one-particle irreducible vertex function is (up to a minus sign) the amputated four-point correlation function obtained from $W(H)$. Thus to first order γ_4 is equivalent to the interaction term (3.3) in the action (for further details see for example [Negele&Orland 1988]).

3.3 The RG scheme: doing the functional integral stepwise

Integral-splitting formula and reducing the bandwidth: In many cases the functional integral for the effective action (3.15) cannot be performed exactly and a perturbative approach has to be used. Doing this, as mentioned in the introduction, one often encounters singularities which in condensed matter problems mostly arise from low energy modes. Therefore it is convenient to perform the functional integral in (3.15) stepwise and do integrate out the innocuous high energy modes first.

To this end we split the Hilbert space of the system into two halves: a low energy part which includes the states with absolute values of the band-energy $\epsilon(\vec{k})$ smaller than a energy scale Λ and a higher energy part with the states with band-energy above Λ. Formally this is achieved by writing the full covariance C of the Gaussian measure as a sum $C = C_< + C_>$:

$$\begin{aligned} \exp\left[-\mathcal{G}(C,\Phi)\right] &= \int d\mu_{C_<+C_>}(\Psi) e^{-\mathcal{V}(\Psi+\Phi)} \\ &= \int d\mu_{C_<}(\Psi_<) \int d\mu_{C_>}(\Psi_>)\, e^{-\mathcal{V}(\Psi_>+\Psi_<+\Phi)}\,. \end{aligned} \tag{3.23}$$

Here we used the so-called covariance splitting formula which holds for arbitrary Gaussian fields. Integrating out the high energy modes corresponds to performing the functional integral with $C_>$ only. Comparing the $d\mu_{C_>}$-integral with (3.15) we observe that this just generates a new effective action for the low energy modes:

$$\exp\left[-\mathcal{G}(C,\Phi)\right] = \int d\mu_{C_<}(\Psi_<)\, \exp\left[-\mathcal{G}(C_>,\Phi+\Psi_<)\right]\,. \tag{3.24}$$

An expansion of $\mathcal{G}(C_>,\Psi_<)$ in monomials of $\Psi_<$ will yield the effective vertices for the theory below the cutoff Λ. Apart from this interpretation as effective action, $\mathcal{G}(C_>,\Phi+\Psi_<)$ also generates the amputated connected correlation functions for the theory above Λ, if we consider $\Phi+\Psi_<$ as source fields.

Equations (3.23) and (3.24) are the formal basis of the RG scheme we use. They express the invariance of the generating functional under performing partial traces over certain degrees of freedom. We can use this invariance to arrive at an effective action at low energy scales. The hope is then that the latter has a simpler form from which one can read off the properties of the low energy excitations.

The RG equations for the n-point correlation functions G_n of the low energy modes can then be obtained from the equation

$$\mathcal{G}(C_\Lambda,\Phi) = -\log \int d\mu_{C_\Lambda}(\Psi)\, e^{-\mathcal{V}(\Psi+\Phi)} \tag{3.25}$$

by taking the derivative with respect to the varying energy scale Λ, expanding both sides in monomials of Φ and comparing the coefficients on the left hand side, which are basically the correlation function G_n differentiated with respect to Λ and the more involved expressions on the right hand side of (3.25). This is described in [Salmhofer 1999]. Here we will use another type of RG equations, namely those for the one-particle irreducible vertex functions.

3.4 The RG equations for the 1PI vertex functions

In this section we describe the derivation the RG equations for the one-particle irreducible vertex functions. First they will be formulated in real space. Then the equations are Fourier-transformed into frequency-momentum space, where the actual numerical implementation is performed.

3.4.1 The explicit RG equations

RG equations for Γ: The RG equations for the 1PI vertex functions can be obtained from

$$\exp\left[-W_\Lambda(H)\right] = \int d\mu_{\mathbf{C}_\Lambda}(\Psi)\, \exp\left[-\mathcal{V}(\Psi) + (H, \Psi)\right] , \tag{3.26}$$

where the covariance $\mathbf{C}_\Lambda = \mathbf{Q}_\Lambda^{-1}$ now has its support on the high energy fields with band energy above a cutoff Λ which we want to integrate out. From

$$\frac{d}{d\Lambda} W_\Lambda(H_\Lambda(\Phi)) = \frac{\partial W_\Lambda(H_\Lambda(\Phi))}{\partial \Lambda} + (\dot{H}_\Lambda(\Phi), \Phi) \tag{3.27}$$

follows (using $\frac{\partial}{\partial \Lambda} W = \dot{W}$ and $\Gamma_\Lambda(\Phi) = W_\Lambda(H_\Lambda(\Phi)) - (H_\Lambda(\phi), \Phi)$)

$$\dot{\Gamma}_\Lambda(\Phi) = \dot{W}_\Lambda(H_\Lambda(\Phi)) . \tag{3.28}$$

In the integral (3.26) only the Gaussian measure is Λ-dependent, and differentiation of its prefactor $(\det \mathbf{Q}_\Lambda)^{-1}$ yields the field-independent and therefore uninteresting term $\mathrm{Tr}(\mathbf{C}_\Lambda \dot{\mathbf{Q}}_\Lambda)$. From differentiating the exponent in (3.26) we get down a factor $(\Psi, \dot{\mathbf{Q}}_\Lambda \Psi)$, where the Ψ's can be replaced by derivatives with respect to the sources H. Altogether we obtain

$$\dot{W}_\Lambda(H) = \frac{1}{2} \mathrm{Tr}(\mathbf{C}_\Lambda \dot{\mathbf{Q}}_\Lambda) + \frac{1}{2} \left(\frac{\delta W_\Lambda}{\delta H}, \dot{\mathbf{Q}}_\Lambda \frac{\delta W_\Lambda}{\delta H} \right) - \frac{1}{2} \left(\frac{\delta}{\delta H}, \dot{\mathbf{Q}}_\Lambda \frac{\delta}{\delta H} \right) W_\Lambda . \tag{3.29}$$

With (3.18) and (3.22) this can be rewritten as an equation for Γ:

$$\dot{\Gamma}_\Lambda(\Phi) = \frac{1}{2} \mathrm{Tr}(\mathbf{C}_\Lambda \dot{\mathbf{Q}}_\Lambda) + \frac{1}{2} \left(\Phi, \dot{\mathbf{Q}}_\Lambda \Phi \right) - \frac{1}{2} \mathrm{Tr} \left[\dot{\mathbf{Q}}_\Lambda \left(\frac{\delta^2 \Gamma_\Lambda}{\delta \Phi^2} \right)^{-1} \right] . \tag{3.30}$$

The first term is field-independent and the second term quadratic in Φ. The inverse second derivative in the third term makes things more complicated, but it can be expressed as a Neumann series in powers of Φ. This is done best after an expansion of Γ in monomials of Φ similar to (3.20),

$$\Gamma_\Lambda(\Phi) = \sum_{m\geq 0} \frac{1}{m!} \int d^m \underline{X}\, \gamma_{m,\Lambda}(\underline{X}) \Phi^m(\underline{X}) \,. \tag{3.31}$$

Inserted in (3.30), this expansion will again lead to an infinite hierarchy of equations for the coefficients of this expansion, which are the 1PI vertex functions $\gamma_{m,\Lambda}(\underline{X})$ for the fields below the cutoff.

The two derivatives in the third term in (3.30) remove two fields in the expansion (3.31), therefore we have

$$\frac{\delta}{\delta\Phi(X)} \frac{\delta}{\delta\Phi(X')} \Gamma_\Lambda(\phi) = \sum_{m\geq 0} \tilde{\gamma}_\Lambda^{(m)}(X, X', \Phi) \,. \tag{3.32}$$

Here due to the antisymmetry properties of vertex functions the $\tilde{\gamma}$ are given by

$$\tilde{\gamma}_\Lambda^{(m)}(X, X', \Phi) = \frac{1}{m!} \int d^m \underline{X''} \gamma_{m+2,\Lambda}(X, X', \underline{X''}) \Phi^m(\underline{X''}) \,. \tag{3.33}$$

Truncation: In the expansion (3.33) above will be mainly interested in the $m = 0$ term which is field independent and equals the inverse two-point function and in the $m = 2$ term which includes the four point vertex γ_4 and two fields. These will turn out to be legs connected to internal lines in the diagrammatic expression of the RG equation. Focusing on these two contributions we have

$$\begin{aligned} \frac{\delta}{\delta\Phi(X)} \frac{\delta}{\delta\Phi(X')} \Gamma_\Lambda(\phi) &= \gamma_{2,\Lambda}(X, X') \\ &+ \frac{1}{2} \int dZ\, dZ'\, \gamma_{4,\Lambda}(X, X', Z, Z') \Phi(Z) \Phi(Z') + \dots \,. \end{aligned} \tag{3.34}$$

This approximation which only retains the two terms written out is equivalent to a truncation after the four-point vertex where the back reaction of higher order 1PI vertex functions on $\gamma_{2,\Lambda}$ and $\gamma_{4,\Lambda}$ is neglected. We will discuss this further in the next section.

The next step is now the evaluation of the inverse in (3.30). This can be done by noting that $\gamma_{\Lambda,2}$ is the inverse of the full Nambu Green's function $\mathbf{G}_{\Lambda,2}$ and therefore

$$\begin{aligned} \frac{\delta}{\delta\Phi(X)} \frac{\delta}{\delta\Phi(X')} \Gamma_\Lambda(\phi) = \int dX'' \gamma_{2,\Lambda}(X, X'') \cdot \Big[\delta(X'', X') \\ + \frac{1}{2} \int dX''' dZ dZ'\, \mathbf{G}_{\Lambda,2}(X'', X''') \gamma_{4,\Lambda}(X''', Z, Z', X') \Phi(Z) \Phi(Z') \Big] \end{aligned} \,. \tag{3.35}$$

The $\gamma_{2,\Lambda}$ in front of the square brackets can be inverted using (3.22), and the inverse of the expression inside the brackets can expanded as geometrical series, $\frac{1}{1+x} \approx 1-x+x^2$,

$$\begin{aligned}\left[\frac{\delta}{\delta\Phi(X)}\frac{\delta}{\delta\Phi(X')}\Gamma_\Lambda(\phi)\right]^{-1} &= \mathbf{G}_{\Lambda,2}(X,X') \\ &-\frac{1}{2}\int dX''dX'''dZdZ'\, G_{\Lambda,2}(X,X'')\gamma_{4,\Lambda}(X'',Z,Z',X''')G_{\Lambda,2}(X''',X')\Phi(Z)\Phi(Z') \\ &+\frac{1}{4}\int dX''dX'''dY''dY'dZdZ'dZ''dZ'''\, G_{\Lambda,2}(X,X'')\gamma_{4,\Lambda}(X'',Z,Z',Y'')G_{\Lambda,2}(Y'',Y') \\ &\gamma_{4,\Lambda}(Y',Z'',Z''',X''')G_{\Lambda,2}(X''',X')\Phi(Z)\Phi(Z')\Phi(Z'')\Phi(Z''')\,. \end{aligned} \tag{3.36}$$

The first term is field-independent and gives a constant contribution to the effective action. The second term contains a product of two Φ-fields and will yield selfenergy corrections while the third term is of fourth order in Φ and yields the flow of the four point vertex. Here, stopping the Neumann series after the second order term does not represent a further approximation, because the higher order terms only generate contributions of higher order in the Φ-fields. These only affect the flow of higher order vertex functions which already have been dropped in the truncation above.

Due to the trace structure of (3.30) the differentiated kernel $\dot{\mathbf{Q}}_\Lambda$ always occurs in the combination $\mathbf{G}_{\Lambda,2}(X''',X')\dot{\mathbf{Q}}_\Lambda(X',X)\mathbf{G}_{\Lambda,2}(X,X'')$ so that it is convenient to introduce the so-called single-scale propagator

$$\mathbf{S}_\Lambda(X'',X''') = -\int dXdX'\mathbf{G}_{\Lambda,2}(X'',X')\dot{\mathbf{Q}}_\Lambda(X',X)\mathbf{G}_{\Lambda,2}(X,X''')\,. \tag{3.37}$$

Using this expression the contributions $\propto \Phi^2$ in the third term in (3.30) read

$$\dot{\Gamma}^{(2)} = \frac{1}{4}\int dXdX'dZ\,dZ'\,\mathbf{S}_\Lambda(X,X')\gamma_{4,\Lambda}(X',Z,Z',X)\Phi(Z)\Phi(Z')\,, \tag{3.38}$$

and the quartic terms are

$$\begin{aligned}\dot{\Gamma}^{(4)} &= -\frac{1}{8}\int dXdX'dY''dY'dZdZ'dZ''dZ'''\,\mathbf{S}_\Lambda(X,X') \\ &\Phi(Z)\Phi(Z')\gamma_{4,\Lambda}(Z,Z',Y,X')\mathbf{G}_{\Lambda,2}(Y,Y')\gamma_{4,\Lambda}(Y',Z'',Z''',X)\Phi(Z'')\Phi(Z''')\,. \end{aligned} \tag{3.39}$$

These two terms are represented graphically in Fig. 3.1.

RG equation for the two-point and four-point vertex function: In order to compare (3.38) and (3.39) with the coefficients in the field-expansion (3.31), we have to antisymmetrize them in the coordinates of the Φ-fields. This, after some renaming of

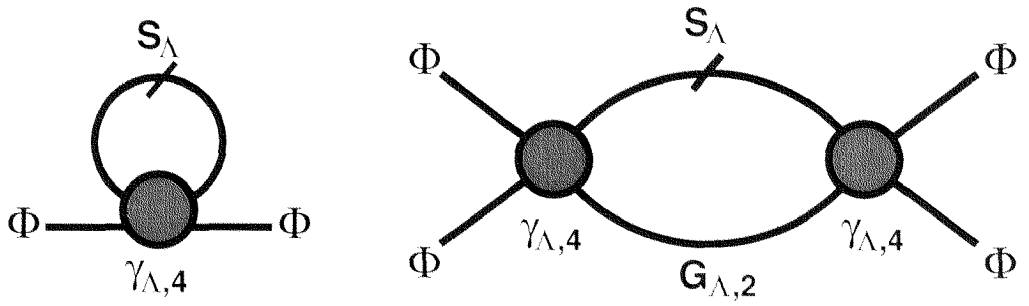

Figure 3.1: *Terms of second and fourth order in the fields in the RG equation for the 1PI vertex functions.*

the variables, leads to the following RG equations for the 1PI two-point and four-point vertex functions,

$$\dot{\gamma}_{2,\Lambda}(X,X') = \dot{\mathbf{Q}}_\Lambda(X,X') + \frac{1}{2}\int dY\,dY'\,\mathbf{S}_\Lambda(Y',Y)\gamma_{4,\Lambda}(Y',Y,X,X')\,. \quad (3.40)$$

$$\begin{aligned}\dot{\gamma}_{4,\Lambda}(\underline{X}) = \frac{1}{2}\int d\underline{Y}\,\mathbf{S}_\Lambda(Y,Y'')\mathbf{G}_{\Lambda,2}(Y',Y''') \\ \cdot\Big[\gamma_{4,\Lambda}(X,X',Y,Y')\gamma_{4,\Lambda}(Y'',Y''',X'',X''') \\ -\gamma_{4,\Lambda}(X,X'',Y,Y')\gamma_{4,\Lambda}(Y'',Y''',X',X''') \\ -\gamma_{4,\Lambda}(X,X''',Y,Y')\gamma_{4,\Lambda}(Y'',Y''',X',X'')\Big]\,. \end{aligned} \quad (3.41)$$

Particle-number conservation: These equations further simplify to one-loop equations similar to those obtained by straightforward perturbation theory if we only consider particle-number conserving propagators vertices. This means that for the two-point vertex $\gamma_{2,\Lambda}(X,X')$ and the Green's function $\mathbf{G}_{\Lambda,2}(X,X')$ the Nambu indices of X and X' must be different, e.g. $-$ for X and $+$ for X'. The same holds for $\mathbf{S}_\Lambda(X,X')$, we use the notation $G_{\Lambda,2}(X,X')$ and $S_\Lambda(X,X')$ for these components. Then we write

$$\gamma_{\Lambda,2}(X,X') = \gamma^n_{\Lambda,2}(X;X')\,,$$

where the first entry in $\gamma^n_{\Lambda,2}$ is always reserved for the incoming particle with $-$ index. Y, Y' etc. further only contain space-time and spin variables and the superscript ^{n} denotes that the particle number is conserved at the corresponding vertex. In $\gamma_{4,\Lambda}(\underline{X})$ we only consider contributions where two Nambu indices are $+$, e.g. the ones belonging to X and X', while the other two belonging to X'' and X''' are $-$. Then the Nambu indices of Y, Y' must be $-$ while those of Y'' and Y''' are $+$ again. In this case we write

$$\gamma_{\Lambda,4}(Y,Y',Y'',Y''') = \gamma^n_{\Lambda,4}(Y,Y';Y'',Y''')\,,$$

where now the two first entries are reserved for the incoming particles with $-$ indices. $\gamma^n_{\Lambda,4}$ is antisymmetric in the first two and the second two entries. With the antisymmetry of the full Green's function $G_{\Lambda,2}$ with respect to interchange of the coordinates the three terms become

$$\begin{aligned}\dot{\gamma}^n_{2,\Lambda}(X_1;X_2) &= \dot{Q}_\Lambda(X_1;X_2) + \\ &\quad \int dY_1 dY_2\; S_\Lambda(Y_2;Y_1)\gamma^n_{4,\Lambda}(X_1,Y_1;X_2,Y_2)\,. \qquad (3.42)\\ \dot{\gamma}^n_{4,\Lambda}(X_1,X_2;X_3,X_4) &= \triangle_{PP,\Lambda}(X_1,X_2;X_3,X_4) + \triangle_{PH,\Lambda}(X_1,X_2;X_3,X_4) \\ &\quad -\triangle_{PH,\Lambda}(X_1,X_2;X_4,X_3) \qquad (3.43)\end{aligned}$$

with the abbreviations

$$\begin{aligned}\triangle_{PP,\Lambda}(X_1,X_2;X_3,X_4) &= \frac{1}{2}\int d\underline{Y}\,\gamma^n_{4,\Lambda}(X_1,X_2;Y,Y_1)L(Y_1,Y_2;Y_3,Y_4) \\ &\quad \cdot\gamma^n_{4,\Lambda}(Y_3,Y_4;X_3,X_4)\,, \qquad (3.44)\\ \triangle_{PH,\Lambda}(X_1,X_2;X_3,X_4) &= -\int d\underline{Y}\,\gamma^n_{4,\Lambda}(X_1,Y_1;X_3,Y_2)L(Y_2,Y_3;Y_4,Y_1) \\ &\quad \cdot\gamma^n_{4,\Lambda}(X_1,Y_4;X_4,Y_3)\,, \qquad (3.45)\end{aligned}$$

and

$$L(Y_1,Y_2;Y_3,Y_4) = G_{2,\Lambda}(Y_1,Y_3)S_\Lambda(Y_4,Y_2) + S_\Lambda(Y,Y_3)G_{2,\Lambda}(Y_4,Y_2)\,.$$

Spin-independent interactions: Further we assume that the interactions are spin-independent, i.e. $SU(2)$-invariant in spin space. Then the total spin and its projection on the z-axis of the two incoming particles has to be the same that of the outgoing particles. This can be achieved in two ways, either by $D^{s1,s2}_{s3,s4} = \delta_{s1,s3}\delta_{s2,s4}$ (1 and 2 label the incoming, 3 and 4 the outgoing particles) or by $E^{s1,s2}_{s3,s4} = \delta_{s1,s4}\delta_{s2,s3}$. Therefore we can make the Ansatz

$$\gamma^n_{4,\Lambda}(X_1,X_2;X_3,X_4) = D^{s1,s2}_{s3,s4}\phi_\Lambda(x_1,x_2,x_3,x_4) - E^{s1,s2}_{s3,s4}\theta_\Lambda(x_1,x_2,x_3,x_4)\,. \qquad (3.46)$$

The x_i variables now denote space-time. From the required antisymmetry of $\gamma^n_{4,\Lambda}$ we immediately get

$$\phi_\Lambda(x_1,x_2,x_3,x_4) = \theta_\Lambda(x_1,x_2,x_4,x_3)\,. \qquad (3.47)$$

This means that in order to obtain the renormalization group flow of the full four-point vertex $\gamma^n_{4,\Lambda}(X_1,\ldots,X_4)$ we only have to consider e.g. the case $s1 = s3 = -s2 = -s4$, from (3.47) we directly obtain the four-point vertex for a different spin configuration, e.g. $s1 = s4 = -s2 = -s3$.

Inserting Ansatz (3.46) and (3.47) and performing the spin sums the RG equations become

$$\dot{\phi}_\Lambda(x_1,x_2;x_3,x_4) = \mathcal{T}_{PP,\Lambda} + \mathcal{T}^d_{PH,\Lambda} + \mathcal{T}^{cr}_{PH,\Lambda}$$

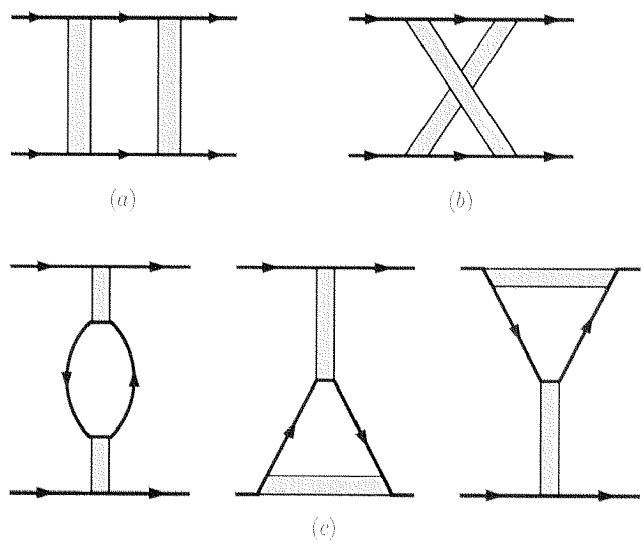

Figure 3.2: *The contributions to the right–hand side of the RGDE. (a) the particle–particle term (b) the crossed particle–hole term (c) the direct particle–hole terms; the first of these three graphs has a factor -2 because of the fermion loop.*

with

$$\mathcal{T}_{PP,\Lambda}(x_1,x_2;x_3,x_4) = -\int dy_1\ldots dy_4 \cdot \phi_\Lambda(x_1,x_2;y_1,y_2)\,L(y_1,y_2,y_3,y_4)\,\phi_\Lambda(y_3,y_4;x_1,x_2) \tag{3.48}$$

$$\begin{aligned}\mathcal{T}^d_{PH,\Lambda}(x_1,x_2;x_3,x_4) = -\int dy_1\ldots dy_4 \Big[&-2\phi_\Lambda(x_1,y_1;x_3,y_3)\,L(y_3,y_2;y_4,y_1)\,\phi_\Lambda(x_2,y_4;x_4,y_2)\\ &+\phi_\Lambda(x_1,y_1;y_3,x_3)\,L(y_3,y_4;y_2,y_1)\,\phi_\Lambda(x_2,y_3;x_4,y_4)\\ &+\phi_\Lambda(x_2,y_1;y_3,x_4)\,L(y_3,y_4;y_2,y_1)\,\phi_\Lambda(x_1,y_3;x_3,y_4)\Big]\end{aligned} \tag{3.49}$$

$$\mathcal{T}^{cr}_{PH,\Lambda}(x_1,x_2;x_3,x_4) = -\int dy_1\ldots dy_4 \cdot\phi_\Lambda(x_1,y_2;y_3,x_4)\,L(y_3,y_1;y_1,y_2)\,\phi_\Lambda(x_2,y_1;y_4,x_3) \tag{3.50}$$

These terms are represented graphically in Fig. 3.2. In the same way we obtain for the selfenergy $\dot{\Sigma}_L = \dot{\gamma}^n_{\Lambda,2} - \dot{Q}_\Lambda$ (see Fig. 3.51).

$$\dot{\Sigma}(x_1,x_2) = \int dy_1 dy_2\, S_\Lambda(y_1,y_2)\,[\phi_\Lambda(y_2,x_1;x_2,y_1) - 2\phi_\Lambda(x_1,y_2;x_2,y_1)]\ , \tag{3.51}$$

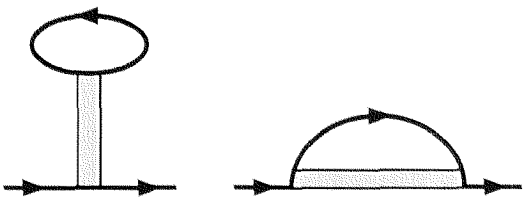

Figure 3.3: *The contributions to the selfenergy.*

Translational invariance: The last step is now the Fourier-transformation of the RG equations into frequency-momentum-space. We define

$$\begin{aligned} G_{\Lambda,2}(p_1,p_2) &= \int dx_1 dx_2 \, \exp\left[-ip_1x_1 + ip_2x_2\right] \, G_{\Lambda,2}(x_1,x_2)\,, \\ S_\Lambda(p_1,p_2) &= \int dx_1 dx_2 \, \exp\left[-ip_1x_1 + ip_2x_2\right] \, S_\Lambda(x_1,x_2) \end{aligned}$$

and

$$\begin{aligned} &\phi_\Lambda(p_1,p_2;p_3,p_4) = \\ &\int dx_1 \ldots dx_4 \, \exp\left[-ip_1x_1 - ip_2x_2 + ip_3x_3 + ip_4x_4\right] \, \phi_\Lambda(x_1,x_2;x_3,x_4)\,. \end{aligned}$$

Here the p's are 4-vectors in frequency-momentum space: $p = (i\omega_n, \vec{p})$ with $i\omega_n = (2n+1)\pi T$ and e.g. $p_x \in [-\frac{\pi}{L_x}L_x, \ldots, \frac{\pi}{L_x}(L_x-1)]$. L_x denotes the number of lattice in x-direction, the lattice constant has been set to 1. Moreover

$$\int dx = \int_0^\beta d\tau \sum_{\vec{x}} \qquad \text{and} \qquad \int dp = T \sum_{i\omega_n} \frac{1}{L_x L_y} \sum_{\vec{p}}\,.$$

From translational invariance we have

$$\begin{aligned} G_{\Lambda,2}(p_1,p_2) &= \delta(p_1-p_2) G_{\Lambda,2}(p_1)\,, \\ S_\Lambda(p_1,p_2) &= \delta(p_1-p_2) S_\Lambda(p_1) \end{aligned}$$

or, more explicitely, with the cutoff function C_Λ depending on the band energy $\epsilon(\vec{p})$,

$$S_\Lambda(i\omega_n,\vec{p}) = \frac{\dot{C}_\Lambda(\epsilon(\vec{p}))}{i\omega_n - \epsilon(\vec{p})}\,. \tag{3.52}$$

Further we obtain

$$\phi_\Lambda(p_1,p_2;p_3,p_4) = \delta(p_1+p_2-p_3-p_4) V_\Lambda(p_1,p_2,p_3)\,.$$

Note that the δ-functions have to be understood on the lattice, i.e. $\vec{k}_1 + \vec{k}_2 - \vec{k}_3 - \vec{k}_4 = 2\pi(n_x, n_y)$ with some integer number n_x and n_y. Finally the RG equations read

$$\dot{V}_\Lambda = \mathcal{T}_{PP,\Lambda} + \mathcal{T}^d_{PH,\Lambda} + \mathcal{T}^{cr}_{PH,\Lambda} \tag{3.53}$$

with

$$\mathcal{T}_{PP,\Lambda}(p_1, p_2; p_3, p_4) = - \int dp\, V_\Lambda(p_1, p_2, p)\, L(p, -p + p_1 + p_2)\, V_\Lambda(p, -p + p_1 + p_2, p_3) \tag{3.54}$$

$$\begin{aligned}\mathcal{T}^d_{PH,\Lambda}(p_1, p_2; p_3, p_4) = \\ - \int dp \Big[& -2V_\Lambda(p_1, p, p_3)\, L(p, p + p_1 - p_3)\, V_\Lambda(p + p_1 - p_3, p_2, p) \\ & + V_\Lambda(p_1, p, p + p_1 - p_3)\, L(p, p + p_1 - p_3)\, V_\Lambda(p + p_1 - p_3, p_2, p) \\ & + V_\Lambda(p_1, p, p_3)\, L(p, p + p_1 - p_3)\, V_\Lambda(p_2, p + p_1 - p_3, p) \Big]\end{aligned} \tag{3.55}$$

$$\mathcal{T}^{cr}_{PH,\Lambda}(p_1, p_2; p_3, p_4) = - \int dp\, V_\Lambda(p_1, p + p_2 - p_3, p)\, L(p, p + p_2 - p_3)\, V_\Lambda(p, p_2, p_3) \tag{3.56}$$

In these equations,

$$L(p, p') = S_\Lambda(p) G_{\Lambda,2}(p') + G_{\Lambda,2}(p) S_\Lambda(p') \,. \tag{3.57}$$

These equations form the basis for the numerical implementation. However further approximations will be necessary: most of the time we neglect the frequency dependence of of the four-point vertex completely, i.e. we replace $V_\Lambda(p_1, p_2, p_3)$ by $V_\Lambda(\vec{p}_1, \vec{p}_2, \vec{p}_3)$. Then, for obvious numerical reasons we have to coarse-grain the $\vec{p}$-dependence of V_Λ to a certain extent as discussed below, which means that we finally calculate with vertex functions $V_\Lambda(k_1, k_2, k_3)$ which are constant in small phase patches labeled by indices k_i ($i = 1, ...N$ with patch number $N = 32...96$).

3.5 The flow of the susceptibilities

3.5.1 Susceptibilities from bosonic source fields

Susceptibilities can be obtained by coupling external boson fields to the bilinears in the fermions that represent charge, spin, Cooper pair and other local densities, and by calculating the corresponding RG flow for these functions. Since the calculations are a straightforward adaptation of the ones presented above, we only state the main points. If the external field is called a, the expansion of Γ_Λ now reads

$$\Gamma_\Lambda(a, \phi) = \sum_{m,n \geq 0} \gamma^{(m,n)}_\Lambda(a, \phi) \,,$$

with

$$\gamma_\Lambda^{(m,n)}(a,\phi) = \frac{1}{m!n!}\int \mathrm{d}^m \underline{X}\, \mathrm{d}^n \underline{Y} \gamma_{mn,\Lambda}(\underline{X},\underline{Y}) a^m(\underline{X})\phi^n(\underline{Y})\,.$$

The RGDE is now derived in the same way as above. Because the a fields are external fields only, the equations for the a–independent parts γ_{0n} remain unchanged, so that $\gamma_{0n} = \gamma_n$ for all n, with the γ_n given as above. Thus the flow for the susceptibilities is driven by the flow for the coupling functions; it takes the form of a linear integro–differential equation.

Since one a field couples to a fermionic bilinear, the truncation consistent with dropping the 1PI six–point function is to leave out all m and n with $2m+n \geq 6$. Using the notation

$$\mathbf{L}(Z_1,\ldots,Z_4) = \mathbf{G}_{\Lambda,2}(Z_1,Z_2)\mathbf{S}_\Lambda(Z_3,Z_4) + \mathbf{S}_\Lambda(Z_1,Z_2)\mathbf{G}_{\Lambda,2}(Z_3,Z_4)$$

this gives the equations

$$\begin{aligned}\dot\gamma_{12,\Lambda}(X;Y_1,Y_2) &= \frac{1}{2}\int \mathrm{d}^4\underline{Z}\,\mathbf{L}(Z_1,\ldots,Z_4) \\ &\quad \gamma_{12,\Lambda}(X,Z_2,Z_3)\gamma_{04,\Lambda}(Z_4,Z_1;Y_1,Y_2)\end{aligned} \tag{3.58}$$

and

$$\begin{aligned}\dot\gamma_{20,\Lambda}(X_1,X_2) &= \frac{1}{2}\int \mathrm{d}^4\underline{Z}\,\mathbf{L}(Z_1,\ldots,Z_4) \\ &\quad \gamma_{12,\Lambda}(X_1,Z_2,Z_3)\gamma_{12,\Lambda}(X_2;Z_4,Z_1)\,.\end{aligned} \tag{3.59}$$

The initial condition on γ_{12} at $\Lambda = \Lambda_0$ determines which susceptibility is considered; in particular, it determines the symmetry of the superconducting order parameter in the case of the coupling to Cooper pairs.

In presence of charge invariance, we get separate equations for the particle–particle and particle–hole vertices, defined as

$$\begin{aligned}&\gamma_{12,\Lambda}^{pp,\epsilon}(x;(y_1,\sigma_1),(y_2,\sigma_2)) \\ &= \gamma_{12,\Lambda}(x;(y_1,\sigma_1,\epsilon),(y_2,\sigma_2,\epsilon))\end{aligned} \tag{3.60}$$

and

$$\begin{aligned}&\gamma_{12,\Lambda}^{ph,\epsilon}(x;(y_1,\sigma_1),(y_2,\sigma_2)) \\ &= \gamma_{12,\Lambda}(x;(y_1,\sigma_1,\epsilon),(y_2,\sigma_2,-\epsilon))\end{aligned} \tag{3.61}$$

By fermionic antisymmetry,

$$\gamma_{12,\Lambda}^{pp,-}(x;(y_1,\sigma_1),(y_2,\sigma_2)) = -\gamma_{12,\Lambda}^{pp,+}(x;(y_2,\sigma_2),(y_1,\sigma_1))$$

and similarly for $\gamma_{12}^{ph,\pm}$, so it suffices to consider one of the $\pm$ quantities. We now also assume spin rotation invariance; then the normal charge ($\sim \delta_{\sigma_1\sigma_2}$) and spin $\sim (\tau_3)_{\sigma_1\sigma_2}$ susceptibility (τ_3 the Pauli matrix) do not couple in the flow. The resulting equations are

$$\begin{aligned} & \dot{\gamma}_{12,\Lambda}^{pp,-}(x;(y_1,\sigma_1),(y_2,\sigma_2)) \\ = & \int \mathrm{d}u_1 \ldots \mathrm{d}u_4 L(u_1,u_2,u_3,u_4) \\ & \gamma_{12,\Lambda}^{pp,-}(x;(u_1,\sigma_1),(u_3,\sigma_2))\, \varphi(s|u_2,u_4,y_1,y_2) \end{aligned} \tag{3.62}$$

for the Cooper pair vertex,

$$\begin{aligned} & \dot{\gamma}_{12,\Lambda,c}(x;y_1,y_2) \\ = & \int \mathrm{d}u_1 \ldots \mathrm{d}u_4 L(u_1,u_2,u_3,u_4) \\ & \gamma_{12,\Lambda,c}(x;u_4,u_1) \\ & [2\varphi_\Lambda(y_1,u_2,y_2,u_3) - \varphi_\Lambda(y_1,u_2,u_3,y_2)] \end{aligned} \tag{3.63}$$

for the charge vertex, and

$$\begin{aligned} & \dot{\gamma}_{12,\Lambda,s}(x;y_1,y_2) \\ = & \int \mathrm{d}u_1 \ldots \mathrm{d}u_4 L(u_1,u_2,u_3,u_4) \\ & \gamma_{12,\Lambda,s}(x;u_4,u_1)\varphi_\Lambda(y_1,u_2,u_3,y_2) \end{aligned} \tag{3.64}$$

for the spin vertex.

After Fourier-transforming the expressions e.g. for the vertices $\gamma_{c/s}(\vec{q},\vec{k})$ describing the coupling of external spin and charge fields of electrons with wavevector $\vec{k}$ read

$$\gamma_{\Lambda,c/s}(\vec{q},\vec{k}) = \int \frac{d\vec{k}'}{(2\pi)^2}\, \gamma_{\Lambda c/s}(\vec{q},\vec{k}')\, L(\vec{k}',\vec{q}) V_{c/s}(\vec{k},\vec{k}',\vec{q}) \tag{3.65}$$

with

$$\begin{aligned} L(\vec{k}',\vec{q}) = & \sum_{i\omega_n} \Big[S_\Lambda(\vec{k}'+\vec{q})i\omega_n) G_{\Lambda,2}(\vec{k}'+\vec{q})i\omega_n) \\ & + G_{\Lambda,2}(\vec{k}'+\vec{q})i\omega_n) S_\Lambda(\vec{k}'+\vec{q})i\omega_n) \Big] \end{aligned}$$

and

$$V_c(\vec{k},\vec{k}',\vec{q}) = -2V_\Lambda(\vec{k},\vec{k}'+\vec{q},\vec{k}+\vec{q}) + V_\Lambda(\vec{k},\vec{k}'+\vec{q},\vec{k}')\,, \tag{3.66}$$

$$V_s(\vec{k},\vec{k}',\vec{q}) = V_\Lambda(\vec{k},\vec{k}'+\vec{q},\vec{k}')\,. \tag{3.67}$$

Therefore the behavior of the spin susceptibility at wavevector $\vec{q}$ is determined by the scattering processes with momentum transfer $\vec{q}$ between second incoming and first outgoing wavevector. As initial condition for the $\gamma_{\Lambda c/s}(\vec{q},\vec{k}')$ we choose a $\vec{k}$-independent value, and for the d-wave pairing vertex we use the initial condition

$$\gamma_{\Lambda_0,d-\text{wave}}(\vec{k}) = \sqrt{2}\cos 2\theta(\vec{k})\,.$$

The corresponding susceptibilities are then obtained from (3.59), e.g.

$$\chi_{c/s}(\vec{q}) = \int \frac{d\vec{k}}{(2\pi)^2}\,\gamma_{c/s}(\vec{q},\vec{k})\,L(\vec{k},\vec{q})\gamma_{c/s}(-\vec{q},\vec{k}+\vec{q})\,. \tag{3.68}$$

3.5.2 Calculation of the uniform susceptibilities

The uniform ($\vec{q}\to 0$) susceptibilities describing the response to external charges and magnetic fields cannot be calculated successively by lowering the IR cutoff as they only involve degrees of freedom very close to the FS (the width of the contributing region is given by the temperature). Hence the kernel $L(\vec{k},\vec{q}\approx 0)$ contributes to the RG flow only at lowest scales and we have to choose other methods to obtain these susceptibilities.

Uniform spin and charge couplings for theory below the cutoff: One way is to determine the responses to uniform external fields for the effective theory below the cutoff Λ with the interactions V_Λ at this scale taken as effective interactions renormalizing the coupling to the external fields via vertex corrections. More precisely we calculate the effective couplings $\gamma_i(\vec{k})$ ($i=c$ for charge and $i=s$ for spin) of quasiparticles on the FS, occurring in the Hamiltonian as

$$\int \frac{d\vec{k}}{(2\pi)^2}\,\gamma_{c/s}(\vec{k})\,(c^\dagger_{\vec{k},\uparrow}c_{\vec{k},\uparrow} \pm c^\dagger_{\vec{k},\downarrow}c_{\vec{k},\downarrow}).$$

Denoting the bare coupling as $\gamma^0_{c/s}$ we can express the effective coupling as

$$\gamma_i(\vec{k}) = \gamma_i^0(\vec{k}) + \int \frac{d\vec{k}'}{(2\pi)^2}\,\gamma_i(\vec{k})L_0(\vec{k}')V_i(\vec{k},\vec{k}') \quad i=c,\ s \tag{3.69}$$

whith $V_c(\vec{k},\vec{k}') = -V_\Lambda(\vec{k},\vec{k}',\vec{k}')+2V_\Lambda(\vec{k},\vec{k}',\vec{k})$ for the charge and $V_s(\vec{k},\vec{k}') = -V_\Lambda(\vec{k},\vec{k}',\vec{k}')$ for the spin coupling. Diagrammatically this equation is shown in Fig. 3.4. The kernel $L_0(\vec{k})$ is the $\omega=0$, and then $\vec{q}\to 0$ limit of the Matsubara sum of the product of two propagators, and given by the derivative of the Fermi function:

$$L_0(\vec{k}) = \lim_{\vec{q}\to 0}\frac{n_F(\epsilon(\vec{k}+\vec{q}))-n_F(\epsilon(\vec{k}))}{\epsilon(\vec{k}+\vec{q})-\epsilon(\vec{k}))} = \frac{dn_F}{dE}\Big|_{E=\epsilon(\vec{k})}. \tag{3.70}$$

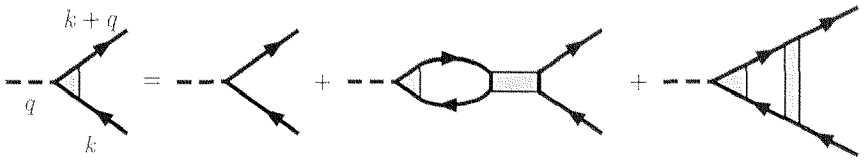

Figure 3.4: *Diagrammatic expression for the renormalization of the couplings $\gamma_{c/s}(\vec{k})$ to external charge or magnetic fields. For uniform external fields we take $\vec{q} \to 0$.*

The uniform susceptibilities are then given as

$$\kappa = -\int \frac{d^2k}{(2\pi)^2} \gamma_c^0(\vec{k})\Phi(\vec{k})\gamma_c(\vec{k}) , \tag{3.71}$$

$$\chi_s(0) = -\int \frac{d^2k}{(2\pi)^2} \gamma_s^0(\vec{k})\Phi(\vec{k})\gamma_s(\vec{k}) . \tag{3.72}$$

In absence of an instability or flow to strong coupling the coupling functions for zero momentum transfer $V_\Lambda(\vec{k},\vec{k}',\vec{k}) - \frac{1}{2}V_\Lambda(\vec{k},\vec{k}',\vec{k}')$ and $-\frac{1}{2}V_\Lambda(\vec{k},\vec{k}',\vec{k}')$ would converge to the Landau interaction functions $f_s(\vec{k},\vec{k}')$ and $f_a(\vec{k},\vec{k}')$, respectively, and the expressions for the susceptibilities obtained with the above scheme reduce to the results from Landau-Fermi liquid theory.

This scheme is formally a RPA treatment of the theory below the cutoff. Note however that upon following the results with lowering Λ vertex corrections through all kinds of parquet diagrams are included because we use the renormalized interactions in the summation. Hence the results are generally different from straightforward RPA in the bare Hubbard model.

Full integration with frozen coupling constants: Another way to obtain the coupling to uniform spin and charge fields is to analyze their change through the RG flow of the interaction V_Λ. To this end we integrate the scheme of Subsection 3.5.1 down to $\Lambda = 0$ but stop the flow of the four-point vertices V_Λ at some scale Λ_{freeze} where they reach a certain value. This allows to study the change of $\gamma_{c/s}(0)$ when the renormalization of the interactions are successively included.

This method appears to be very similar to the RPA summation below the cutoff described above. However here all modes – also those above the cutoff – are included. Moreover the typical RPA Stoner-like poles with sign changes in the denominator are absent because the perturbation series is organized differently. Here e.g. for a logarithmically diverging density of states and constant coupling constants we would obtain a power-law divergence of the uniform spin susceptibility for $\Lambda \to 0$ rather than a pole at non-zero infrared cutoff Λ_c. The flow of the interactions however prevents the power-law divergence from occurring (see Subsection 5.3.1). For the flow to strong coupling described in this thesis the two schemes give qualitatively similar results: the suppression

of uniform spin and charge susceptibility in the saddle point regime is observed with both schemes in the same parameter range but there are quantitative differences.

3.6 Further points

3.6.1 The dual interpretation of the RG flow

There are two ways to interpret the RG flow:

A The vertex functions at scale Λ define the effective action of the theory below the cutoff. This view is closely related to the Wilson's original idea of an RG transformation generating a flow in the parameter space of possible Hamiltonians. Note however that the action/Hamiltonian at scale Λ is in general not required have the same form as the original action/Hamiltonian.

B The vertex functions at scale Λ allow to obtain the connected correlation functions of the interacting theory with infrared cutoff Λ. Therefore integration down to $\Lambda = 0$ yields (in principal and if doable) the correlation functions of the full theory. Because of this second interpretation it is sensible to consider vertex functions $V_\Lambda(\vec{k}_1, \vec{k}_2, \vec{k}_3)$ for wavevectors corresponding to band energies above the cutoff.

3.6.2 Scaling

An advantage of Wilsonian RG schemes is that scale invariance is not required as the cutoff is explicitly kept in the scheme. This is particularly important for the treatment of the two-dimensional Hubbard model with the FS at the van Hove points, where the the logarithmic divergence of the density of states spoils scaling and the definition of a cutoff-independent renormalized coupling constant in the "field-theoretical" approach[Solyom 1979]. In absence of scale invariance the correspondence between temperature and energy scale becomes less strict, as the density of states or effective phase space probed at different temperatures generally varies. Problems for the interpretation arising from this are discussed at the end of the next chapter.

3.6.3 Non-zero temperature

As may have become clear in the derivation, the RG scheme formulated above is in principle a transformation of the generating functionals and can therefore be applied at any temperature T. Interpretation A in terms of an effective low energy theory however becomes artificial as soon as the RG scale Λ, equivalent to the bandwidth of the effective theory, becomes smaller than T. Then we should choose interpretation B of the RG

procedure which regards the scheme simply as a consistent way to calculate correlation functions.

Finite temperature has two effects in the one-loop flow. First it represents an infrared cutoff which damps the singularities on the FS. Second it smears out the Fermi surface and therefore the phase space restrictions through the Pauli principle become less effective. This second effect can overcompensate the first one in cases of imperfect nesting (see also Subsection 4.3.1).

3.6.4 The truncation: role of higher order vertex functions

The truncation described in the previous section is equivalent to setting all one-particle irreducible vertex function of order higher than four equal to zero. This means that the higher order correlation functions are given by one-particle reducible graphs, i.e. tree diagrams made from two- and four-point 1PI vertex functions. The neglect of the higher order irreducible vertex functions will certainly be justified if the system stays weakly coupled. Moreover all Hartree-Fock or mean-field ground states can be understood in terms of two-point and four-point vertex functions. However note that nonquadratic effective interactions between different bosonic modes would correspond to non-vanishing higher order irreducible vertex functions, thus in the case described in the following with an intrinsic coupling between AF and d-wave channel this approximation might breakdown. A proper treatment of this effect by keeping higher order 1PI vertex functions is beyond our present scope.

3.6.5 One-loop, frequency dependence and connection to perturbation theory

Although the RG equations derived above are one-loop equations, their solution contains all diagrams which can be constructed from an arbitrary number of parquet diagrams, i.e. particle-particle and particle-hole loops. The reason is that the vertices occurring in the one-loop diagrams on the right hand side of the RG equations e.g. in Fig. 3.2 are the renormalized vertices γ_Λ at that scale. When we insert the flow of γ_Λ down to scale Λ, given by

$$\gamma_\Lambda = \int_{\Lambda_0}^{\Lambda} d\Lambda' \, \dot{\gamma}_{\Lambda'} + \gamma_{\Lambda_0}$$

at one of the two vertices, this amounts to inserting another one-loop diagram, namely the right hand side of the RG equation for $\gamma_{\Lambda'}$ at this place. Repeating this process we see that the RG equation contains diagrams of any order. Since we have to integrate over all internal particles by doing as many $d\Lambda$ integrals as one-loop insertions , the solution of the RG equation[2] (3.41) down to a certain scale Λ is basically equivalent to the full par-

[2]Here we neglect the selfenergy corrections to the internal propagators.

quet perturbation series with infrared cutoff Λ. In particular ladder summations are fully reproduced by the RG equation restricted to an appropriate channel. The great advantage of RG approaches is of course, as mentioned in the beginning of this chapter, that they allow a straightforward and consistent summation of all types of parquet diagrams and that potential singularities are approached in a controlled way.

A non-trivial point is the neglect of the frequency dependence of the four-point vertices. This means that e.g. in a two-loop term the convolution of two Matsubara sums $\sum_\omega \sum_{\omega'} f(\omega-\omega')g(\omega')$ over internal frequencies is replaced by a product over two independent sums, $\sum_\omega f(\omega) \sum_{\omega'} g(\omega')$. Here f and g stand for products of two propagators and the corresponding $\vec{k}$-space integrals. This approximation will however not change the leading flow, as $g(\omega')$ is peaked around $\omega' = 0$.

3.7 Other RG schemes

Here we comment on some other related Wilson-type RG schemes used in condensed matter physics and compare them with the scheme described above.

3.7.1 Poor man's scaling

The poor man's scaling scheme is already very similar in its spirit to the modern general Wilsonian schemes in the sense that it explicitly aims at constructing a low-energy effective Hamiltonian. It was introduced by Anderson in his treatment of the Kondo problem [Anderson 1970]. One directly constructs an effective Hamiltonian for the low energy modes by integrating out high energy modes occurring in the perturbation expansion. This is achieved by writing a perturbation series for the effective low-energy interaction and inserting projection operators acting on the intermediate states which require that at least one intermediate particle in the energy shell to be eliminated. For the typical 1D applications with linear dispersion the poor man's scaling is equivalent to our 1PI scheme as long as the leading one-loop flow is considered. However the prescription of the projection operator on intermediate states with at least one particle in the energy range to be integrated out becomes questionable when one applies the scheme to problems where the intermediate particles have different energies such that low and high energy scales become coupled. Therefore it is desirable to have a more rigorously deduced scheme which consistently prescribes how the high energy states should be integrated out. In contrast to the 1PI formalism the poor man's scheme is a projection scheme where all information on correlation functions between states above the cutoff is lost.

3.7.2 The Polchinski scheme used by Zanchi and Schulz

Polchinski's RG equation is obtained from the generating functional of the connected m-point correlation functions G_m and yields a hierarchy of coupled equations for the G_m which for all applications has to truncated in some way. The main complication for the numerical treatment is that in the Polchinski equation the flow of the four-point correlation functions is given by one diagram with a self-contracted six-point function and another diagram with a four-point and a two-point function linked by a single line, such that the important one-loop contributions are hidden in the flow of the six-point vertex. Zanchi and Schulz [Zanchi 1997] solved this problem by inserting the integrated flow of the latter into the self-contracted six-point-term in the equation for the four-point vertex thus including the important one-loop contributions without having to calculate the six-point function explicitly. However this comes at the price of having an integro-differential RG equation which is non-local in the cutoff, which complicates the numerical treatment. Nonetheless the Zanchi-Schulz results with this complicated scheme agree well with our results from the simpler 1PI scheme when the same parameters are used.

3.7.3 The Wick-ordered scheme

The Wick-ordered scheme is described in Salmhofer's book [Salmhofer 1999] and was used by Halboth and Metzner in their recent study of the two-dimensional Hubbard model [Halboth 2000]. The starting point is again the generating functional for the connected m-point correlation functions, which is this time expanded into Wick-ordered monomials of the fields. This brings along an important simplification: the right hand side of the equations for the m-point functions does not contain self-contracted $m+2$-point functions anymore. Instead we get ordinary one-loop terms and other contributions. Therefore after truncating the equation by setting the six-point function equal to zero, the RG equations for the two-point and four-point vertex contains the important one-loop terms and remain local in the cutoff. This simplifies the numerical treatment considerably.

In contrast with the 1PI scheme, in the Wick-ordered scheme the internal lines are bare propagators, where one line is at the cutoff while the other propagator has its support on modes below the cutoff. On the level of approximations of our present N-patch calculation the results of Wick-ordered and 1PI scheme agree qualitatively using the same parameters for both.

Chapter 4

N-Patch RG in the t-t' Hubbard Model

In this chapter we describe the numerical implementation of the RG equation described in the previous chapter. Then we discuss some general features of the flow.

4.1 The model, the Fermi surface and parameters

The kinetic energy of the $t - t'$ Hubbard model is given by the tight-binding dispersion

$$\epsilon(\vec{k}) = -2t(\cos k_x + \cos k_y) - 4t' \cos k_x \cos k_y - \mu \tag{4.1}$$

with nearest neighbor (n.n.) hopping t, next nearest neighbor (n.n.n.) hopping t' and chemical potential μ. Typically we choose $t' = -0.3t$ which yields a small convex curvature of the FS around (π, π) at larger band fillings (see Fig. 4.1). The dispersion becomes flat at $(0, \pi)$ and $(\pi, 0)$ which leads to van Hove singularities in the density of states at the band energy of these points (see Fig. 4.2). If they are close to the FS the broad regions with similar band energy around these saddle points will be important in the RG flow, because they give large contributions to the low energy scattering processes. Another essential curve next to the Fermi surface will turn out to be the Umklapp surface (US) which connects the van Hove points with straight lines (see dashed line in Fig. 4.1). If the FS crosses this line, two particles at the FS can be scattered from one side of the US to the opposite one in an elastic process involving only low energy quasiparticles. As we will see, these additional scattering channels then enhance the energy scale for the flow to a strong coupling regime. The bare interaction is the well-known Hubbard on-site repulsion

$$H_U = U \sum_{\vec{x}} n_{\vec{x},\uparrow} n_{\vec{x},\downarrow}, \tag{4.2}$$

which is constant in k-space. For most results discussed here we take $U = 3t$. We choose this rather strong initial interaction because we are interested in the breakdown

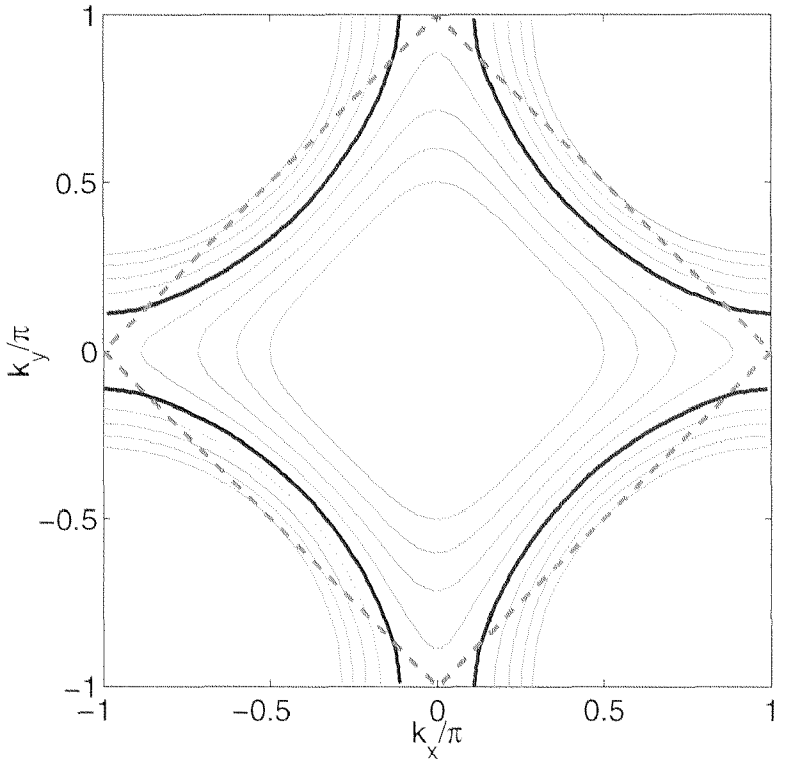

Figure 4.1: *The Fermi surface of the t-t′ dispersion given by (4.1) for* $t' = -0.3t$ *and* $\mu = -t$.

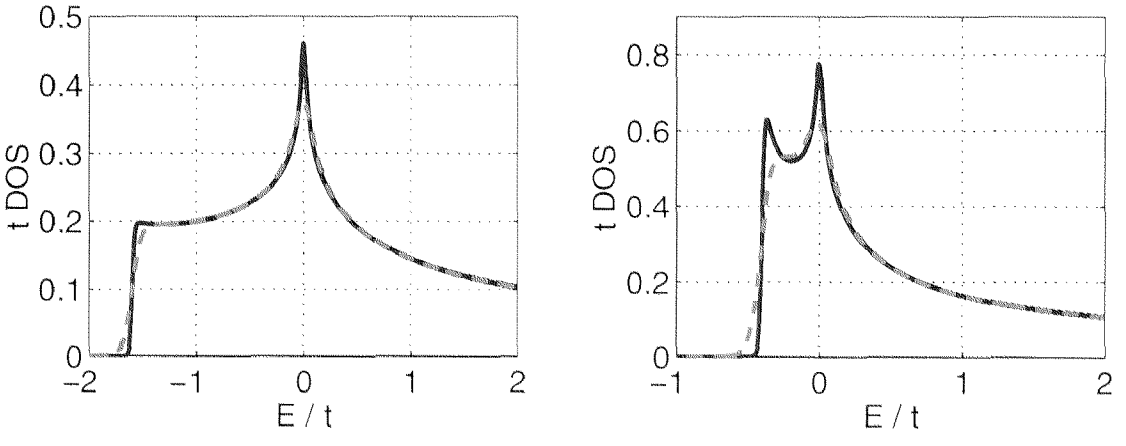

Figure 4.2: *Density of states per spin orientation at the van Hove filling for* $t' = -0.3t$, $\mu = -1.2t$ *(left plot) and* $t' = -0.45t$, $\mu = -1.8t$ *(right plot). The curves were calculated with a thermal smearing by the derivative of the Fermi function at* $T = 0.01t$ *(solid curves) and* $T = 0.04t$ *(dashed curves).*

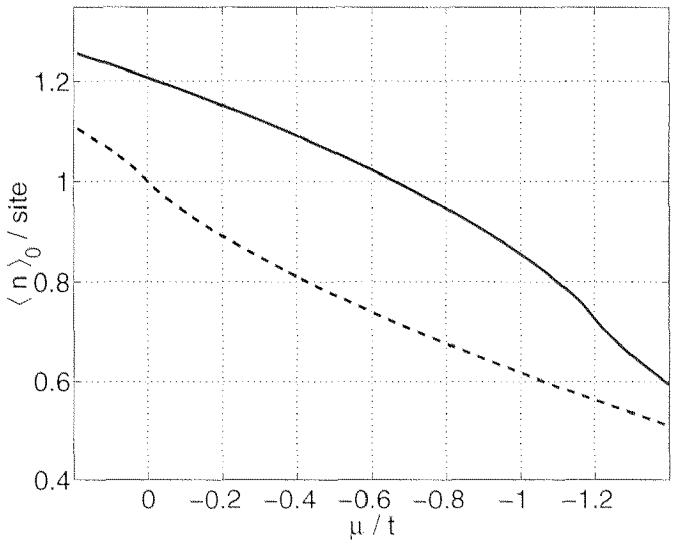

Figure 4.3: *Average electron density per site versus chemical potential, calculated for the non-interacting model. The solid curve are the values for $t' = -0.3t$, the broken curve is for $t' = 0$. The temperature used for this calculation was $T = 0.01t$*

of the Landau-Fermi liquid due to Coulomb interaction effects (keeping the cuprates in mind) and do not aim at a full classification of possible weak coupling instabilities.

(4.2) will be the initial condition for the flow of the four-point vertices,

$$V_\Lambda(k_1, k_2, k_3) = U \quad \text{at} \quad \Lambda = \Lambda_0 \,.$$

Here Λ_0 is the initial RG scale, which we take to be $4t$. With decreasing Λ the effective vertex $V_\Lambda(k_1, k_2, k_3)$ will develop a pronounced k-space structure in the RG flow.

We will mainly vary the temperature T and the particle density near and below half filling via the chemical potential μ. Primarily we will be concerned with the density range around half-filling. The van Hove filling, where the FS exactly touches the saddle points, is given by $\mu = -4t' = -1.2t$, or ≈ 0.73 electrons per site. Having in mind the Mott insulating state of the real cuprates at half band filling ($\langle n \rangle$/site $= 1$), we call the density range with $\langle n \rangle$/site < 1 the *hole-doped* side, while for $\langle n \rangle$/site > 1, we use the term *electron-doped* side. For the relation between chemical potential and non-interacting electron density see Fig. 4.3.

For a given μ the dependence of the average particle number on T is weak and irrelevant for the results. Both parameters μ and T change the effective phase space for the various scattering processes. In particular, increased temperature provides a larger phase space for particle-hole processes with momentum transfer (π, π), which play an important role. This is similar to the quasi-1D organic conductors where above a certain temperature the band curvature due to interchain hopping becomes irrelevant and 1D nesting effects determine the behavior of the system [Bourbonnais 1991].

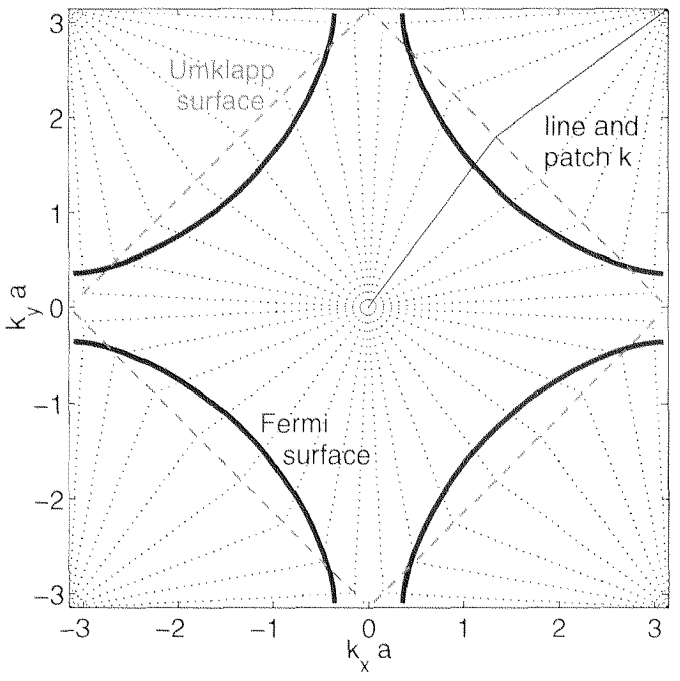

Figure 4.4: *The Brillouin zone, Fermi and Umklapp surface and the lines in the patch centers for $N = 32$. The solid dots in the patches denote the wave vectors for which the four-point vertex function is calculated. For all wave vectors inside the same patch, $V_\Lambda(\vec{k}_1, \vec{k}_2, \vec{k}_3)$ is approximated by a constant.*

4.2 The N-patch scheme

4.2.1 Lines and patches

For setting up the numerical N-patch scheme we first define a phase space discretization following Zanchi and Schulz [Zanchi 1997]. The Brillouin zone (BZ) is divided up into N segments or patches centered around N lines. Each line starts from the origin along a certain angular direction $\theta(k)$ and from the $(\pm\pi, \pm\pi)$ points so that the lines meet at the Umklapp surface (see Fig. 4.4). The reason we we choose straight lines is purely simplicity. Another possible choice would be to follow the gradient of the dispersion. This however requires more numerical steps in mapping $\vec{k}$-space points onto the patches. The phase space integrations with measure $d^2k/(2\pi)^2$ occurring in the one-loop terms are performed approximately as sums over the patches and integrations over the radial direction along a certain number n_a of integration lines per patch which also lead from the origin to the (π, π) points with a kink on the Umklapp surface. For $N = 32$ patches we typically chose $n_a = 3$ integration lines. As can be inferred from Fig. 4.5, the dependence of the flow and the critical scale is small for for $n_a \geq 3$ even at the van Hove

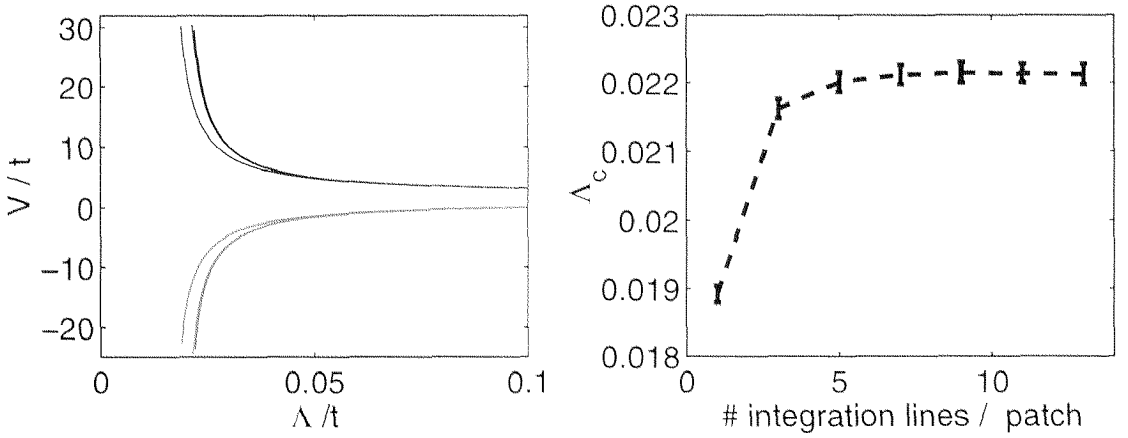

Figure 4.5: *Left flow of the g_3-like (diverging to $+\infty$) and g_4-like (diverging to $-\infty$) Cooper processes at the saddle points for $t' = -0.3t$, $T = 0.01t$ and $\mu = -1.2t$ with the FS at the van Hove singularities. The different lines correspond to different numbers of integrations lines $n_a = 1, 3, 5, \ldots 13$ inside each of the 32 patches. Right: Critical scale Λ_c where the largest coupling reaches $30t$ versus n_a. The errorbars correspond to the stepwidth used in the numerical integration.*

filling, such that we take $n_a = 3$ in the most cases. The dependence of the critical scale for the flow to strong coupling on the patch number N for $n_a = 3$ is shown for a typical case in Fig. 4.6.

4.2.2 Discretizing $V_\Lambda(\vec{k}_1, \vec{k}_2, \vec{k}_3)$

In principle the four-point vertex $V_\Lambda(\vec{k}_1, \vec{k}_2, \vec{k}_3)$ is a continuous function of the three wavevectors $\vec{k}_1$, $\vec{k}_2$ (the two incoming) and $\vec{k}_3$ (first outgoing) each ranging over the full BZ. For a numerical treatment however we have to discretize the wavevector dependence of $V_\Lambda(\vec{k}_1, \vec{k}_2, \vec{k}_3)$. The initial four-point vertex is a constant function of all three wavevectors, but this certainly changes during the flow. From the previous studies of the two-patch model it is clear that the angular variation for e.g. moving the first incoming wavevector around the FS will be relevant in the sense that it grows under reducing the energy scale Λ. Therefore we will try to keep the as much as possible of the dependence of $V_\Lambda(\vec{k}_1, \vec{k}_2, \vec{k}_3)$ on the angles of $\vec{k}_1$, $\vec{k}_2$ and $\vec{k}_3$.

What do we know about the radial variation? From power-counting arguments one can expect that the radial dependence of the couplings does not change the main features of the flow to strong coupling. The leading flow will come from one-loop contributions with energy denominators $\propto 1/\Lambda$ which become singular for $\Lambda \to 0$. If we expand the vertices $V_\Lambda(\{\vec{k}_{\rm ext}\}, \{\vec{k}_{\rm int}\})$ in a Taylor series around the set of internal wave vectors on the Fermi surface, $\{\vec{k}_{\rm int}\} = \{\vec{k}_F\}$, we observe that only the zeroth order term in this expansion really gets the large $1/\Lambda$ contribution, while all terms containing derivatives

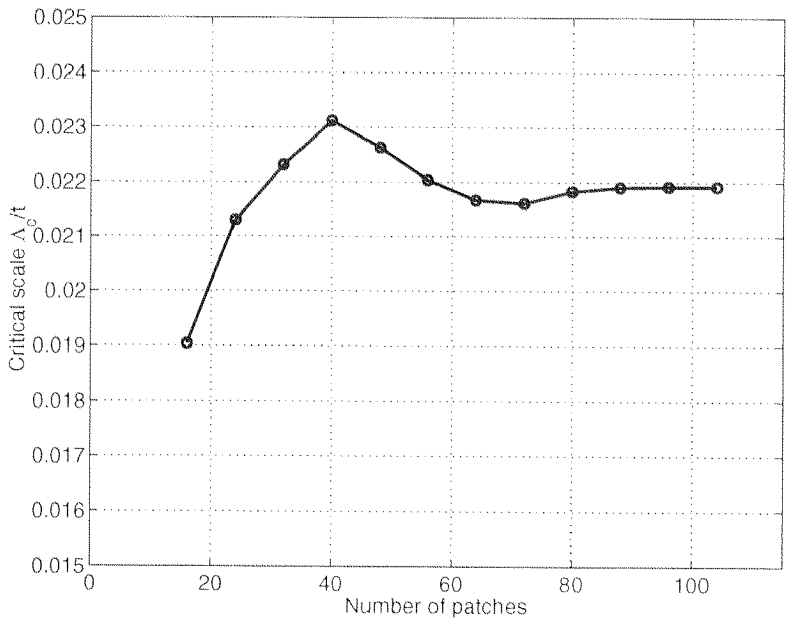

Figure 4.6: *Dependence of the critical scale Λ_c at the van Hove-filling $\mu = -1.2t$ on the number of patches N. Here for each N the intra-patch integration was performed along three lines and the flow was integrated up to $V_{\max} = 50t$.*

of $V_\Lambda(\{\vec{k}_{\rm ext}\}, \{\vec{k}_{\rm int}\})$ on the FS carry additional small factors $\sim \{\vec{k}_{\rm int}\} - \{\vec{k}_F\}$ which cancel the smallness of Λ in the denominator.

Thus one can expect that the leading flow can be calculated by using the four-point vertices with internal legs on the FS in the one-loop diagrams. In the integration over the internal particle coordinates we always project the wavevectors $\{\vec{k}_{\rm int}\}$ on the FS[1] and use the coupling function $V_\Lambda(\{\vec{k}_{\rm ext}\}, \{\vec{k}_{F,\rm int}\})$. Then, since we are interested in the four-point vertices for modes close to the FS, we can put the external wavevectors on the FS as well. This means that the set of vertex functions to be calculated reduces to the set $V_\Lambda(\vec{k}_{F,1}, \vec{k}_{F,2}, \vec{k}_{F,3})$ with a certain collection of Fermi wavevectors $k_{F,i}$ which we choose to be the intersection points of the lines in the patch centers with the FS. Thus the number of patches determines the angular resolution in the flow for the four point vertex.

In the following we will use the notation $V_\Lambda(k_1, k_2, k_3)$ denotes the value of the four point vertex with incoming wavevectors $\vec{k}_{F,1}$ and $\vec{k}_{F,2}$ and first outgoing wavevector $\vec{k}_{F,3}$.

The irrelevance of the radial dependence appears to be true as far as qualitative features are regarded. In order to obtain radial information, the phase space segments around the lines can further be split into n_r patches along the radial direction. In the following

[1]The energies of the intermediate states occurring in the denominator and the Fermi functions in the numerator are of course calculated without projection using the dispersion (4.1).

chapters, apart from the $n_r = 1$ results without any radial resolution we also show data for 32×3-systems with $N = 32$ and $n_r = 3$ where one patch per line is centered around the FS with e.g. $|\epsilon(\vec{k})| < 0.4t$, while the other two patches cover phase space regions at higher positive or negative band energy. This gives a minimal amount of radial resolution. With this method we will see that for certain cases vertices between $\vec{k}$-space regions away from the FS grow stronger than the vertices fro wavevectors at the FS. Still this does not change the general behavior, nonetheless it yields additional information on the coupling between different channels (see Subsection 7.1.1).

4.2.3 Integration of the RG equations

The numerical integration of the RG equations for the set of four-point vertices discussed above is performed with a simple forward-integration scheme with variable step width. Using discrete rotational symmetry it is sufficient to calculate $\frac{1}{8}$ of the N^3 vertex functions. One run for a given parameter set requires typically 120 steps.

We start the flow at a high scale $\Lambda_0 = 4t$ such that we integrate out the largest part of the BZ. This is the most balanced choice when we want to compare the results over a larger span in the band filling. One could argue that a comparison to the high-T_c cuprates becomes complicated through the fact that the one-band description of the copper-oxide planes only applies to low band energies. However the strong $\vec{k}$-space dependence of $V_\Lambda(k_1, k_2, k_3)$ only develops at lower energies. This is shown for a typical example in Fig. 4.7. The main process at higher energy scales is a suppression of the repulsive interaction in the s-wave pairing channel. This is a very general process which does not rely on details of the band structure. The d-wave component in the pair scattering begins to be generated by the mechanism described in Eq. 1.6) when particle-hole one-loop contributions become possible at scales $\Lambda \approx |-4t-4t'-\mu|$ (smeared by the continuous cutoff function and finite temperature), corresponding to the energy at the bottom of the band.

4.3 The flow to strong coupling and what we learn from it

In a broad density range around half-filling the RG flow of the four-point vertices leads towards strong coupling. This means that upon reducing the scale, i.e. integrating the RG differential equations, the four point vertices $V_\Lambda(k_1, k_2, k_3)$ become larger until they exceed values comparable to the bandwidth $W \approx 8t$ at a certain critical scale Λ_c. For scales lower than Λ_c the validity of the scheme becomes questionable. The reason is that selfenergy corrections and higher order irreducible vertex functions which are neglected in our scheme may become relevant. Therefore our RG flow should be stopped after

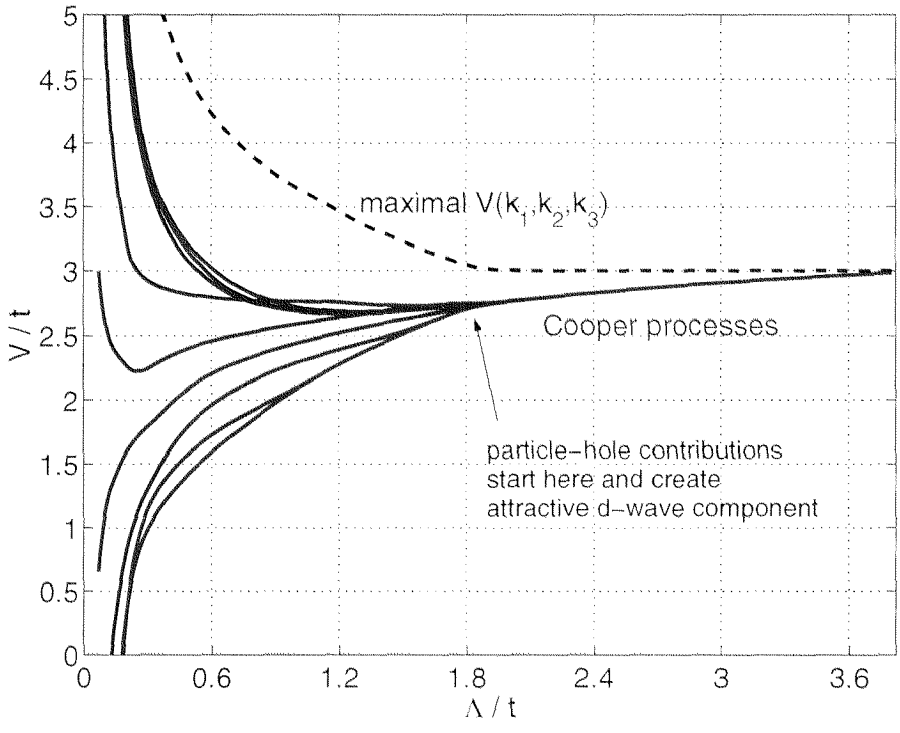

Figure 4.7: *Flow of the Cooper couplings (solid lines) and the maximal coupling* $\max[V(k_1, k_2, k_3)]$ *(dashed line) for* $t' = -0.3t$, $\mu = -t$ *and* $T = 0.04t$. *Particle-hole contributions are possible below* $\Lambda = 1.8t$.

reaching the critical scale Λ_c. Nonetheless it is possible to extract valuable information from analyzing which interactions become large and how this occurs. This will be discussed in the following, together with certain problems for the interpretation.

4.3.1 The critical scale

The critical scale Λ_c is a rough measure of the energy scale below which the quasiparticle properties will be strongly altered through the processes leading to the strong coupling flow. For example for a simple Cooper instability, the critical scale for the divergence in the particle-particle channel turns out to be half of the BCS mean-field gap,

$$\Lambda_c = \Lambda_0 \exp\left[-\frac{1}{N_F|V_0|}\right] .$$

In these logarithmic cases which also include typical quasi-1D systems it is possible to relate Λ_c to a critical temperature or cross-over temperature T_c below which the alteration of the low-energy spectrum occurs. In cases with more complex dispersion and interplay between several channels this equivalence does not hold in general. For example it

can occur that non-zero temperature enhances the coupling between different processes because it increases the number of intermediate states allowed by the Fermi functions occurring in the one-loop integrals. If the coupling is such that the distinct processes reinforce each other this can result in a non-monotonic variation of the critical scale with temperature[2]. Moreover in the numerical analysis with moderate initial interaction it is generally difficult to sharply define a critical scale or temperature because for moderate initial interactions the coupling strength exceeds the order of the bandwidth before the flow gets sufficiently steep. In addition the evolution of the couplings does not follow a simple function.

In Fig. 4.8 we plot the scales where the flow of the interaction strengths exceeds the values $10t$, $20t$ and $30t$ for a broad range of chemical potentials. The divergence of the interactions is steepest at the van Hove filling ($\mu = -1.2t$ at $t' = -0.3t$) because the density of states increases towards $\Lambda \to 0$.

4.3.2 Most divergent couplings and susceptibilities

In the clearcut cases the interactions which grow most strongly belong to a certain class of processes which drive the flow of a susceptibility related to some kind of long-range ordered ground state. For a pure superconducting instability only the Cooper processes and a corresponding pairing susceptibility diverge, and for a nesting instability only processes with the nesting wave-vector as momentum transfer become large and a certain particle-hole susceptibility will be strongly peaked at this wavevector.

It is often pointed out that RG is a powerful and unbiased method to treat problems with several singular channels. For the predictive power of the method this is true as long as these channels remain weakly coupled and in the course of the flow one channel turns out to clearly dominate the others. The conventional strategy is to classify the different channels with respect to the strength of their growth or divergence, e.g. by calculating critical exponents of the corresponding susceptibilities in the vicinity of Λ_c. If the result is unambiguous (see e.g. the electron-doped case in Chapter 7 or the Chapter 8) the RG flow to strong coupling then suggests that the true ground state of the system has long range order of the type selected by the RG. If symmetry-breaking is possible, the strong coupling state can be described in terms of Hartree-Fock or mean-field description with a mean-field corresponding to the strongest divergent susceptibility.

Again the explicit numerical analysis can be difficult due to the problems in defining the critical scale. In addition for our cases the couplings leave the perturbative range before the flow of the susceptibilities reaches its asymptotic behavior. Therefore an analysis of the strength of the divergence often depends on the scale chosen and all boundaries in

[2] Another extreme counter-example even in a simple system are Fermi-liquid $\vec{q} = 0$ instabilities. The one-loop terms leading to such instabilities are only non-zero in a small shell of width of the temperature T around the FS, therefore would cause a very steep and diverging flow at lowest scales $\leq T$. Thus $\Lambda_c \sim T$ which certainly will not give a reasonable estimate of the critical temperature in this case.

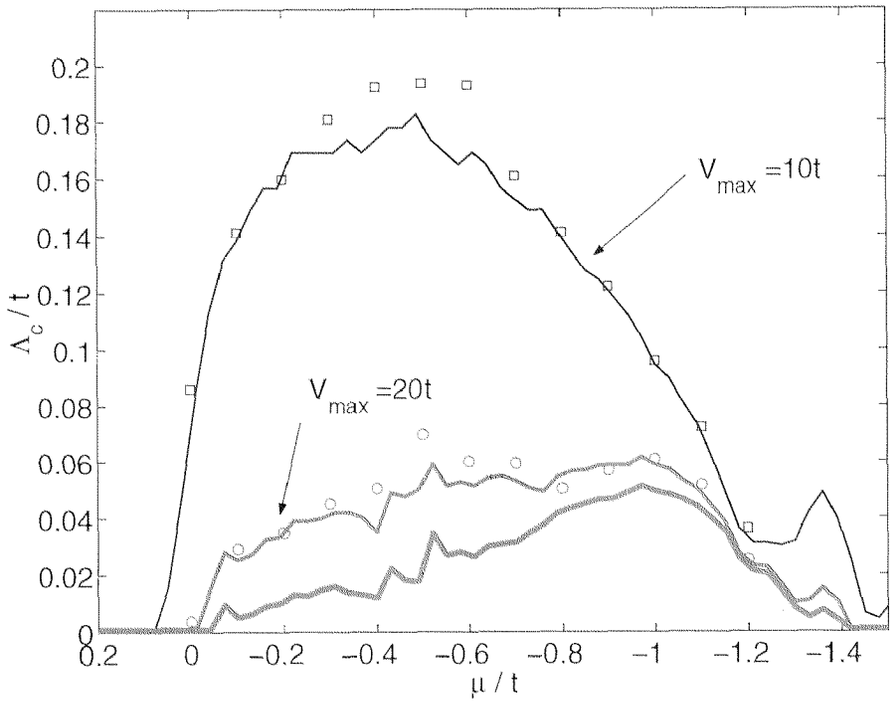

Figure 4.8: *Critical scale Λ_c versus chemical potential μ for the flow to strong coupling with initial interaction $U = 3t$. The different lines denote the scale where the largest coupling reach the values $10t$, $20t$ and $30t$ for a $N = 32$ system. The squares and circles denote the values for the same parameters in a 32×3 system. The discontinuities in $\Lambda_c(\mu)$ become weaker for larger patch numbers.*

the tentative phase diagrams come with large uncertainty.

Furthermore we here consider cases (the half-filled 2-leg ladder and the saddle point regime) where the RG flow is more complex and where due to the intrinsic coupling between several classes of interactions various susceptibilities grow with comparable strength. In particular when the coupling is reinforcing it becomes implausible that a simple mean-field theory selecting one of these classes correctly describes the strong coupling state. A proper strong coupling description of such states in spatial dimensions higher than one remains an open problem. We restrict ourselves to showing analogies between the two-dimensional case and the two-leg ladder, where a bosonization analysis clarifies the nature of the strong coupling state (see Chapter 2). Further the mutual reinforcement between AF and d-wave channel identified as the reason for the interesting flow suggests that the particular behavior is not tied to one spatial dimension but arises from the complex interplay between distinct classes of interactions also valid in two dimensions.

4.3.3 Diverging susceptibilities and the Hohenberg–Mermin–Wagner theorem

The largest parts of our results are obtained for non-zero temperature and in many cases the growth of certain susceptibilities is indistinguishable from a divergence. As stated by the Hohenberg-Mermin-Wagner theorem (see e.g. [Auerbach 1994]) in two spatial dimension long range order from breaking of a continuous symmetry is impossible, such that the real part of the static AF susceptibility $\chi_s(\pi, \pi)$ or the pairing susceptibilities should remain finite. The destruction of long range order at non-zero temperature occurs because the number of thermal fluctuations around the ordered state diverges. This effect however is not taken into account in our RG scheme, as we only couple static external fields to the electrons and do not endow them with a dynamics. The latter however is necessary in order to incorporate quantum or thermal fluctuations. A possible albeit complicated way to do better would be to couple all kinds of external fields corresponding to the fluctuations around the ordered state to the electrons. Then the RG scheme, i.e. the integrating out the fermions, is equivalent to replacing the fermionic problem by a bosonic problem with a space- and time-dependent susceptibility as propagator of the bosonic fields yielding the dynamics of the fluctuations. Furthermore it may generate interactions between the bosons which change their spectrum and destabilize an ordered state.

Chapter 5

The RG Flow to Strong Coupling on the Hole-Doped Side: The Saddle Point Regime

In this chapter we analyze the flow to strong coupling in the two-dimensional t-t' Hubbard model for particle densities $\langle n \rangle \leq 1$ per site. We will introduce three regimes with distinctive character of the RG flow. The main result is that in one of these regime, the so-called *saddle point regime* the flow to strong coupling is analogous to the flow in the half-filled two-leg Hubbard ladder and the two-patch model described in Chapter 2. This means that in this parameter range we find strong d-wave and AF correlations accompanied by a suppression of uniform spin and charge susceptibility on the FS parts close to the saddle points. This suggests the formation of an insulating spin liquid in the BZ regions around the saddle points.

We then describe how d-wave superconductivity on the remaining parts of the FS can be stabilized through the coupling to the ISL. We also analyze the one-loop FS flow. There we do not find a strong shift of the FS before the interactions become larger than the bandwidth such that the flow to strong coupling with fixed FS where our interpretations are built on should be a good approximation. Further we discuss possible Landau-Fermi liquid instabilities in the forward scattering channel.

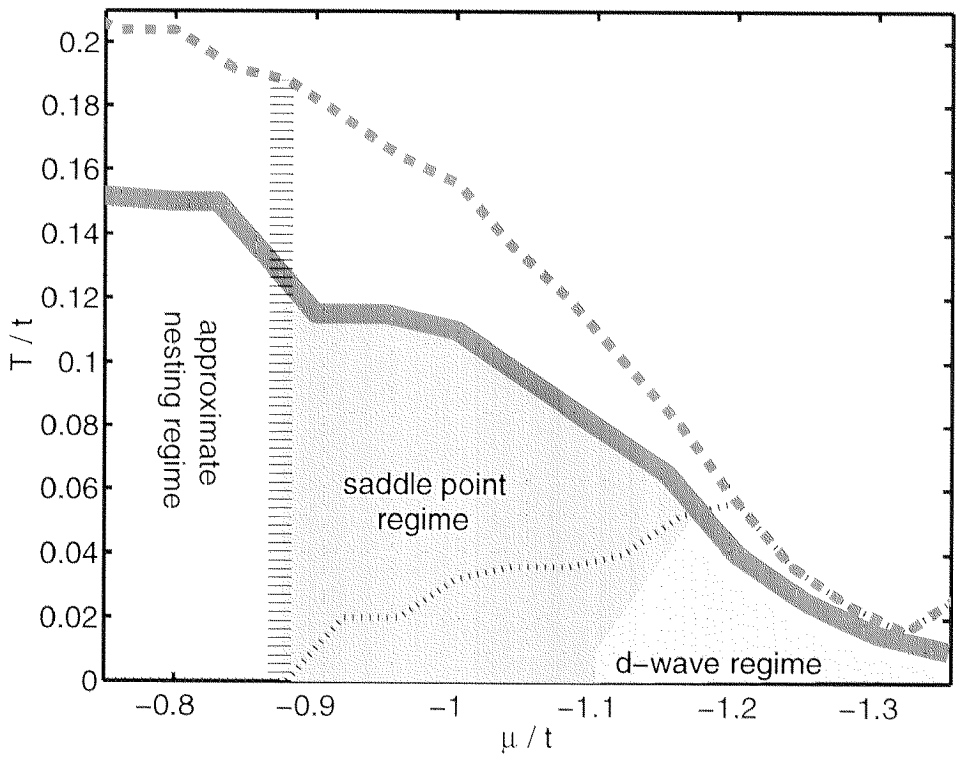

Figure 5.1: *Dependence of the flow to strong coupling on the chemical potential μ and temperature T for $t' = -0.3t$ and initial interaction $U = 3t$. Above the thick solid (dashed) line we can integrate the flow down to zero scale without that the couplings exceeed $50t$ ($30t$). Below the thin broken line the growth (i.e. the derivative with respect to Λ) of d-wave pairing susceptibility χ_{dw} exceeds the growth of the AF susceptibility $\chi_s(\pi,\pi)$ when the largest couplings have reached $12t$. Above this line, $\chi_s(\pi,\pi)$ grows faster than χ_{dw}. The darker gray region denotes the* saddle point regime *where the charge coupling of the saddle point regions goes to zero and the total charge compressibility is suppressed (the extension of this regime to $T = 0$ is discussed in the text). The lightly shaded region represents the* d-wave dominated regime. *Left to the thick vertical line the instability is increasingly dominated by couplings away from the saddle points, we refer to this region as the* approximate nesting regime.

5.1 The three regimes

In the density range from $\langle n \rangle \approx 0.966$ to $\langle n \rangle \approx 0.622$ ($\mu = -0.75t$ to $\mu = -1.32t$)) examined here, we always find a flow towards strong coupling at sufficiently low temperature. The character of this divergence of the coupling functions varies continuously with density and temperature. However we can identify three qualitatively different regimes, which we will call the *d-wave dominated regime*, the *saddle point regime* and the *approximate nesting regime*, as illustrated in Fig. 5.1. For these cases the location of the regions of low band energy around the FS with respect to the Umklapp surface (US, see the dashed line in Fig. 5.2) is different. While in the d-wave regime the Umklapp processes are only elastic in a small phase space region at the saddle points, in the saddle point regime and in the approximate nesting regime the FS intersects the US with the consequence that Umklapp processes between the intersection regions on two sides of the US enter the low energy flow in a dominant way and determine the flow to strong coupling, e.g. by generating tendencies for charge gap formation on these FS parts.

Our analysis does not allow us to draw sharp boundaries between the different regions. Rather, the character of the strong coupling flow changes in a crossover–like fashion as one moves from one region into the other[1]. We will describe the criteria for the definition of these regimes in the corresponding subsections. There, in order to show the main features, we examine the flow for three densities and temperatures typical for each regime. The Fermi surfaces and locations of the patch centers that label our coupling constants are displayed in Fig. 5.2. In Figs. 5.5 and 5.6 we show snapshots of the couplings at the scale where the largest couplings have exceeded the order of the bandwidth: we plot the dependence of the coupling $V_A(k_1, k_2, k_3)$ with the first outgoing wave vector k_3 fixed at point 1 closest to the saddle points or at point 3 closer to the BZ diagonal. In Fig. 5.3 we compare the flow of several relevant couplings as a function the RG scale and in Fig. 5.10 we plot the behavior of the d-wave pairing susceptibility χ_{dw} and the AF susceptibility $\chi_s(\pi, \pi)$. In the following we describe the three regimes in detail.

5.1.1 The d-wave dominated regime

At band fillings around the van Hove filling $\mu = -1.2t$ and low temperature $T = 0.01t$ (see right plots in Figs. 5.5, 5.6, and 5.3), the divergence of the coupling functions only occurs at a low scale and the d-wave pair scatterings are by far the most strongly divergent couplings. In Fig. 5.5, they appear as red and blue features along the lines with patch numbers $|k_1 - k_2| = N/2$ (on these lines, the incoming pair momentum is zero). Other couplings like Umklapp and forward scatterings (the red, violet and black lines in Fig. 5.3) grow, too, but are much smaller than the Cooper couplings. This is the typical

[1] Note however that in a full strong-coupling coupling description there may be true (quantum) phase transitions, i.e. by crossings of ground state energies. These tiny energy changes are however not accompanied by large alterations of the one-loop RG flow.

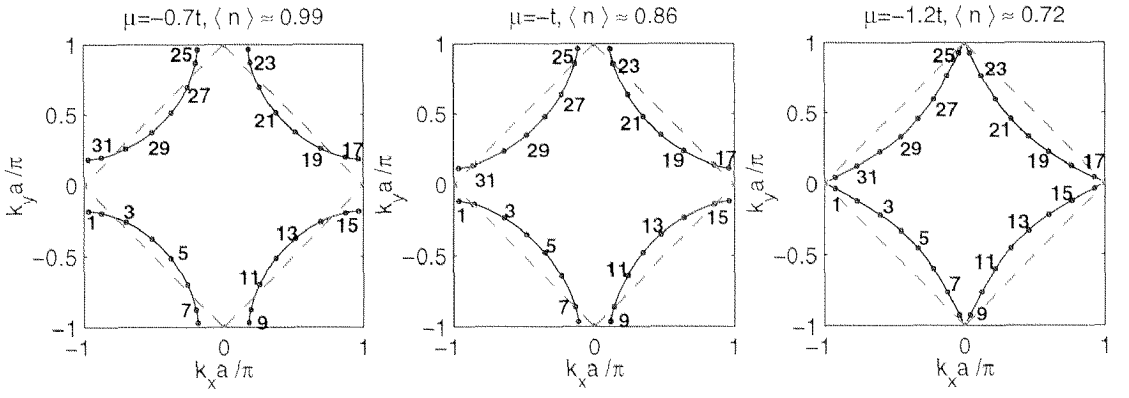

Figure 5.2: *Fermi surfaces and the 32 points for the three different chemical potentials discussed in the text. $\langle n \rangle$ denotes the average particle number per site, i.e. $\langle n \rangle = 1$ corresponds to half-filling. The dots on the FS (solid line) indicate the patch centers with patch indices given by the numbers. The dashed line denotes the Umklapp surface (US).*

flow to strong coupling in the lightly shaded regions in Fig. 5.1. At low temperatures it extends also to densities slightly higher than the van Hove density.

A closer analysis shows that the d-wave component in the pair scattering is generated at intermediate scales by the particle-hole processes with momentum transfer (π, π) as described in Chapter 1. Hence this type of flow to strong coupling can be considered as a Kohn-Luttinger-type Cooper instability where the repulsive scattering in the particle-hole between the saddle points first generates a sizable initial value for the d-wave pair scattering and is then gradually cut off at lower scales because the phase space for the (π, π)-particle-hole processes decreases due to the shape of the FS. The pair scattering amplitudes are shown in detail in Fig. 5.4.

The dominance of the d-wave Cooper scattering is also seen in the comparison of the susceptibilities: the d-wave pairing susceptibility χ_{dw} grows much faster than the AF susceptibility $\chi_s(\vec{q})$ (see Fig. 5.10).

The uniform charge susceptibility κ is somewhat suppressed at intermediate scales but very close to the instability the attractive Cooper scatterings in the forward scattering channel start to dominate the vertex corrections to the charge coupling and cause a pole in the RPA-like expression (see Eq. 3.69) for $\gamma_c(\vec{k})$ for $\vec{k}$ near the saddle points. This is shown in Fig. 5.7. From the right plot we observe that the charge coupling γ_c for modes close to the van Hove points ($\theta \approx 0$) diverges to $+\infty$ instead of being supressed to zero. This is then the reason of a sharp upturn in κ (see Fig. 5.11) as also observed by Halboth et al. [Halboth 2000]. Thus the RG flow in the d-wave regime is not consistent with a flow towards an incompressible state and does not suggest the opening of a charge gap at the saddle points.

At low scales the uniform spin susceptibility $\chi_s(0)$ is suppressed to zero by the strong

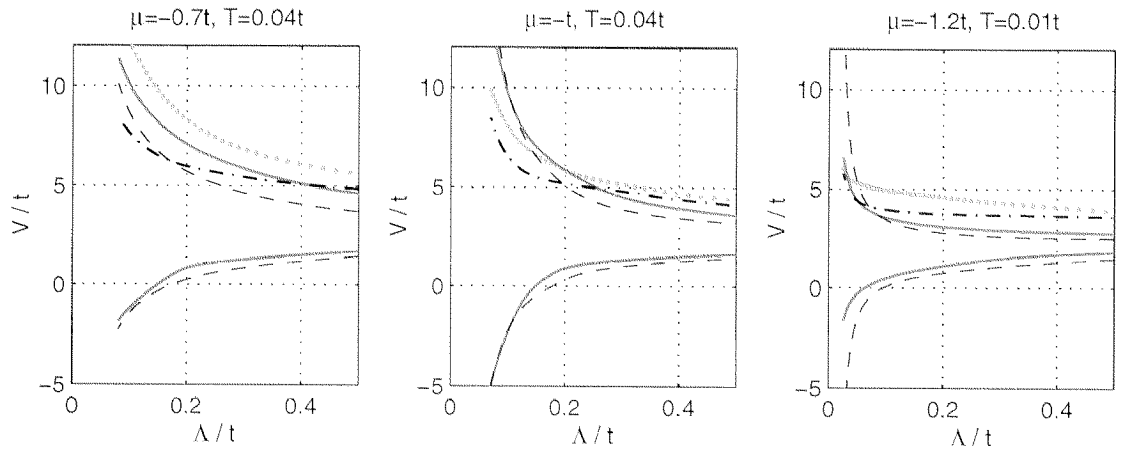

Figure 5.3: *(color) Flow of the couplings for 32-patch system: d-wave Cooper (blue dashed lines), g_3 Umklapp (e.g. $V_\Lambda(24,24,1), V_\Lambda(23,23,2)$, solid red lines), g_2 forward (e.g. $V_\Lambda(24,1,24), V_\Lambda(23,2,23)$, black dashed dotted lines), g_1 Umklapp couplings (e.g. $V_\Lambda(16,17,1)$, solid violet lines) and Umklapp scatterings $V_\Lambda(21,21,4)$ in the BZ diagonal (green) for the three different choices of chemical potential and temperature discussed in the text.*

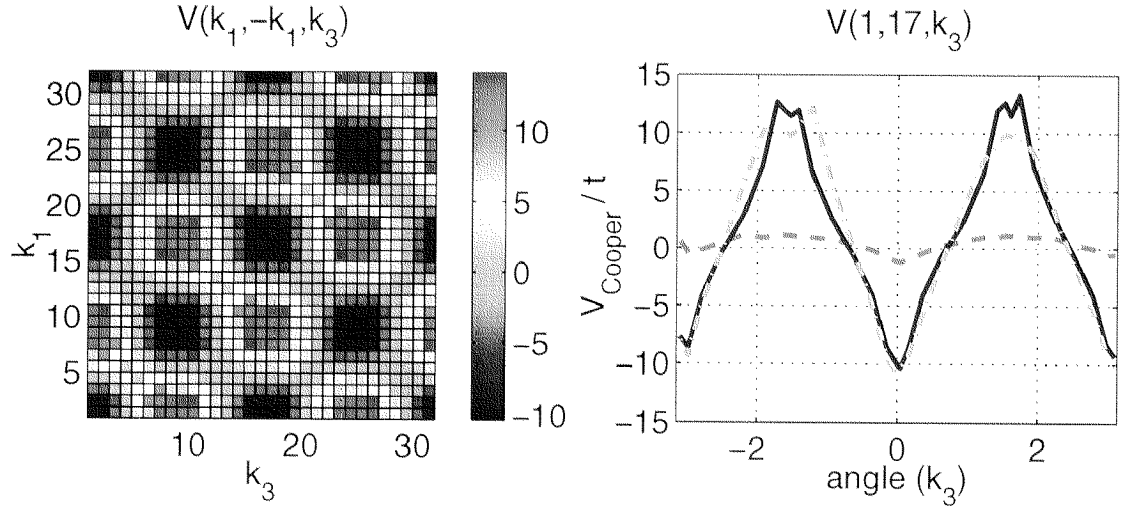

Figure 5.4: *(color) Left: Snapshot of the Cooper couplings $V_\Lambda(\vec{k}_1, -\vec{k}_1, \vec{k}_3)$ in the k_1-k_3 plane. The numbers correspond to the location of the points around the FS. The colorbars indicate the values of the couplings. Right: k_3-dependence of the pair scattering $V_\Lambda(\vec{k}_1, -\vec{k}_1, \vec{k}_3)$ with $\vec{k}_1$ fixed at point 1. The solid line stands for incoming wavevectors on the FS, the flat dashed line for wavevectors at band energy $-0.4t$, and the dashed-dotted line denotes wavevectors outside the FS with band energy $0.4t$. Both plots show data for $\mu = -1.2t$ and $T = 0.01t$.*

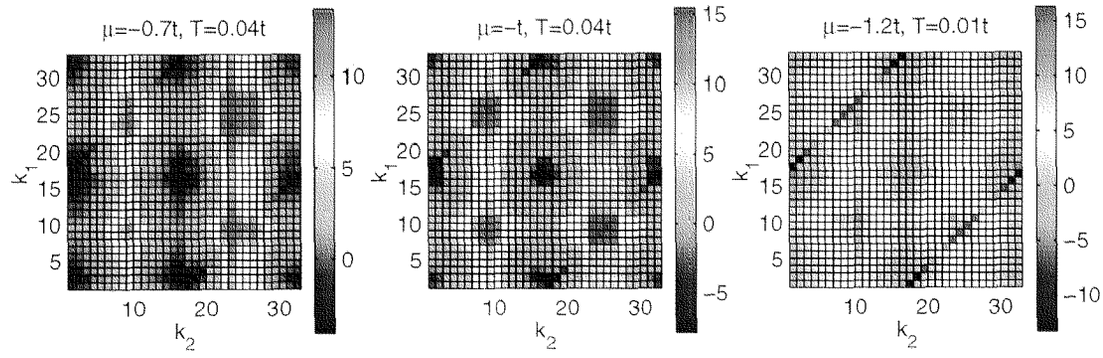

Figure 5.5: *(color) Snapshot of the couplings $V_\Lambda(k_1, k_2, k_3)$ with first outgoing wave vector k_3 fixed at point 1 (see Fig. 5.2) when the largest couplings have exceeded the order of the bandwidth for the three different choices of chemical potential and temperature discussed in the text. The colorbars indicate the values of the couplings.*

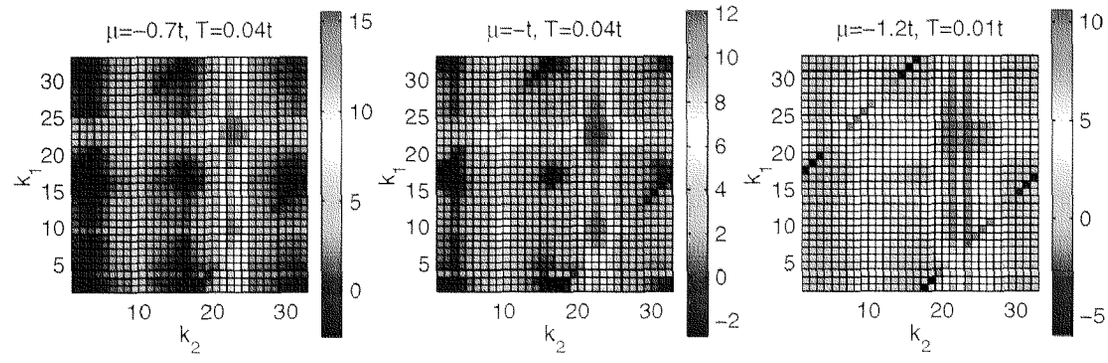

Figure 5.6: *(color) Snapshot of the couplings $V_\Lambda(k_1, k_2, k_3)$ with first outgoing wave vector k_3 fixed at point 3 (see Fig. 5.2) when the largest couplings have exceeded the order of the bandwidth for the three different choices of chemical potential and temperature discussed in the text. The colorbars indicate the values of the couplings. For $k_2 = 22$, $\vec{k}_2 - \vec{k}_3 \approx (\pi, \pi)$ for $\vec{k}_2$, $\vec{k}_3$ close to the US.*

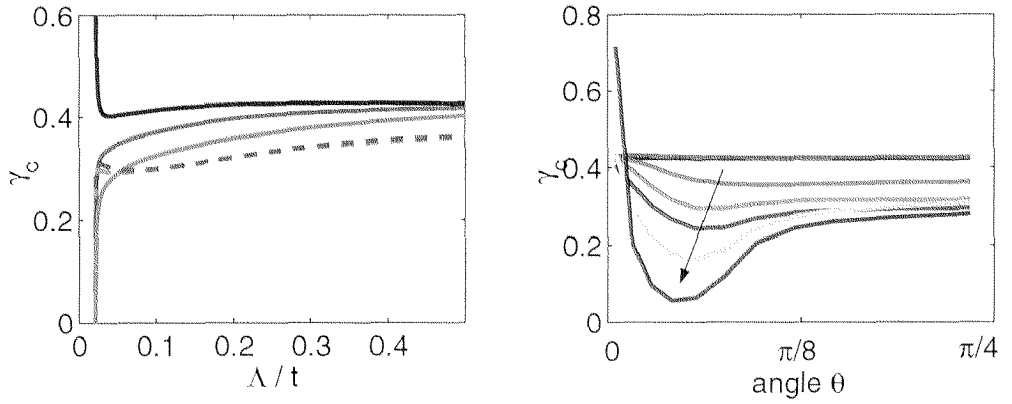

Figure 5.7: *Left plot: Change of the charge couplings $\gamma_c(\vec{k})$ for quasiparticles with different wave vectors $\vec{k}$ on the FS as the electronic interactions flow to strong coupling from a 96 point calculation in thed-wave regime at $\mu = -1.2t$ and $T = 0.01t$. The different lines are for points close to the saddle points (solid lines), and points closer to the BZ diagonal (dashed lines). Right plot: Angular dependence of the charge coupling γ_c for the effective theory below the cut-off Λ for different values of Λ, decreasing in direction of the arrow. θ measures the angle of the points on the FS. $\theta = 0$ corresponds to points at the saddle points and $\theta = \pi/4$ in the BZ diagonal. These curves were calculated using the RPA-type scheme of Subsection 3.5.2.*

attractive g_4 couplings favoring singlet formation. At higher scales, which are not related to the flow to strong coupling, the naive Stoner criterion for ferromagnetism is fulfilled due the large DOS around the van Hove filling. For reasons that will be discussed in Section 5.3 , we ignore this effect.

5.1.2 The saddle point regime

Next we choose $T = 0.04t$ and a band filling slightly above the van Hove filling such that the FS crosses the US (chemical potential $\mu = -t$). Now the scale where the couplings reach the order of the bandwidth is strongly enhanced. In Fig. 5.5 we observe that next to the d-wave pair scatterings new features have developed. The strongly repulsive interactions, for instance $(k_1, k_2) \approx (24, 25) \rightarrow (k_3, k_4) \approx (1, 17)$, correspond to g_3-type Umklapp scatterings driving the AF channel which now diverge together with the repulsive Cooper couplings. This is shown in the middle plot of Fig. 5.3. Note that this behavior is in strong analogy with the flow in the half-filled two-leg ladder, described in Chapter 2.

The forward scatterings of g_2-type also show a strong increase towards the divergence. In addition there is a general increase for couplings with momentum transfer (π, π) due to the enhanced influence of the particle-hole channel with this momentum transfer. On the other hand we also observe strongly attractive couplings emerging e.g. $(k_1, k_2) \approx$

$(16, 17) \rightarrow (k_3, k_4) \approx (1, 18)$. These processes correspond to Umklapp g_4 processes of pairs with both incoming particles at the same saddle-point and outgoing particles on opposite sides of the FS. Since these pairs have small total momentum they couple into the Cooper channel and are driven to strong attraction along with the attractive Cooper couplings with zero pair momentum. This again demonstrates that Umklapp and Cooper channel are strongly coupled. For this choice of parameters the AF susceptibility grows considerably towards the divergence and is as large as the d-wave pairing susceptibility (see Fig. 5.10).

We call this the *saddle point regime* because the flow to strong coupling is dominated by the saddle point regions. Here, the basic mechanism of the half-filled two-leg Hubbard ladder and the two-patch model described in Chapter 2 is at work: d-wave Cooper and AF processes with incoming and outgoing particles close to the saddle points diverge together at the same scale.

Further we find the other key signatures of a flow to an ISL as well: the charge and spin gap tendencies. The diverging g_3-type Umklapp scattering between the saddle point regions drives the forward scattering of g_2-type to strong repulsion, correspondingly the coupling $\gamma_c(\vec{k})$ of external charge fields to these FS parts and thus their contribution to the charge compressibility κ is increasingly suppressed as we approach the instability. This can be seen in Figs. 5.8 and 5.11. In contrast to the FS parts near the saddle points regions, which tend to incompressible i.e. insulating behavior, for $\vec{k}$ in the BZ diagonal the charge coupling $\gamma_c(\vec{k})$ is more or less unchanged. Certainly this is not a proof of a partial charge gap, but given the analogy to the half-filled Hubbard ladder this strongly suggests that at wavevectors near $(\pi/2, \pi/2)$ gapless charge excitations will remain while near the saddle points the FS will be truncated. We use this particular behavior of the $\vec{k}$-space local charge compressibility to define the saddle point regime (darker gray regions in Fig. 5.1): Here the charge couplings around the saddle points continue to go to zero if we integrate the flow far out of the perturbative range without any indication of the upturn in κ that we found in the d-wave dominated regime. However we repeat that from the flow of the four-point vertices the border between saddle point and d-wave dominated regime appears as a continuous cross-over.

In our earlier calculations [HSFR 1999] using the RPA-type scheme for the theory below the cutoff the suppression of the charge couplings γ_c at low temperatures was only weak and we did not extend the saddle point down to zero temperature. With the "frozen interactions"- scheme described in Subsection 3.5.2 the suppression of the charge couplings at the saddle points also holds at lowest T. This is shown in Fig. 5.9 for $\mu = -1.1t$ and $T = 0.006t$. Therefore this method suggests the formation of incompressible regions also in the ground state.

The breaking up of the FS into a part where it is replaced by an ISL and another part where it remains is further discussed in Subsection 5.2. The distinctive behavior of the two FS parts is also visible in the quasiparticle scattering rates (Chapter 6).

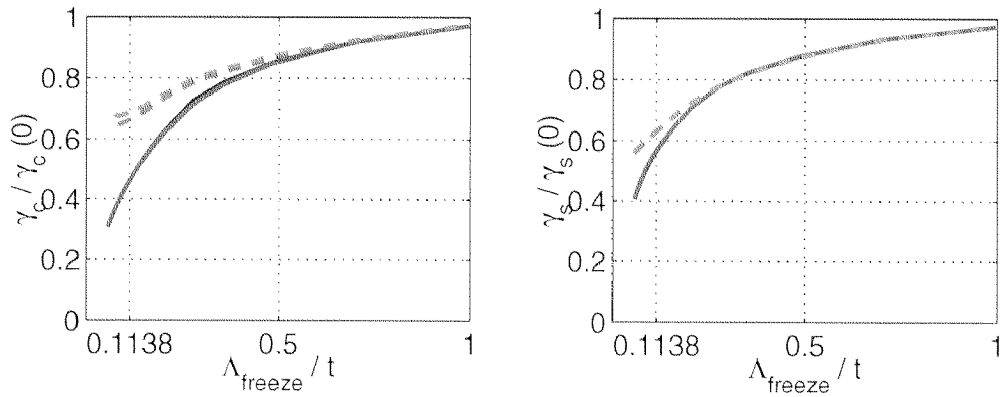

Figure 5.8: *Change of the charge $\gamma_c(\vec{k})$ (left plot a)) and spin couplings $\gamma_s(\vec{k})$ (b)) normalized to their initial values for quasiparticles with different wave vectors $\vec{k}$ on the FS as the electronic interactions flow to strong coupling from a 64 point calculation in the saddle point regime at $\mu = -t$ and $T = 0.04t$. The different lines are for points close to the saddle points (solid lines), and points closer to the BZ diagonal (dashed lines). At $\Lambda = 0.1138t$, the largest couplings exceed $10t$.*

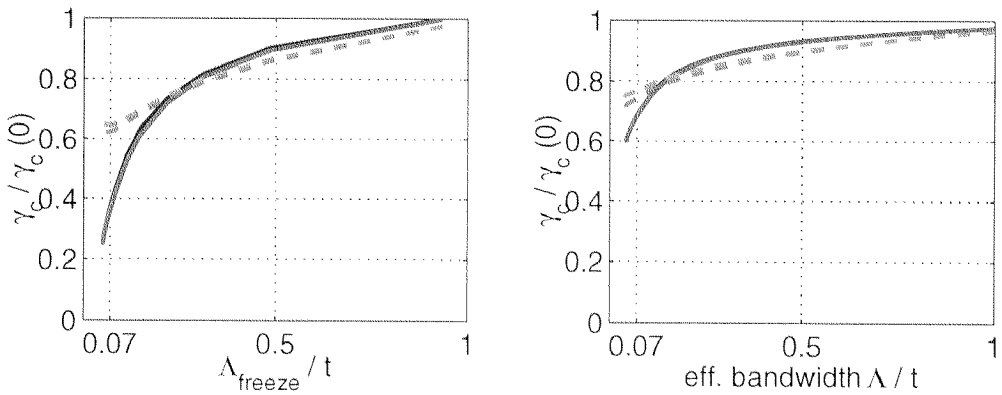

Figure 5.9: *Change of the charge $\gamma_c(\vec{k})$ normalized to their initial values as the electronic interactions flow to strong coupling at $\mu = -1.1t$ and $T = 0.006t$. The curves in the left plot were calculated with freezing the flow of the interactions below $\Lambda_{\rm freeze}$, the curves in the right plot are calculated using the RPA-type scheme for the theory below the cutoff Λ. Again the different lines are for points close to the saddle points (solid lines), and points closer to the BZ diagonal (dashed lines). At $\Lambda = 0.07t$, the largest couplings exceed $10t$.*

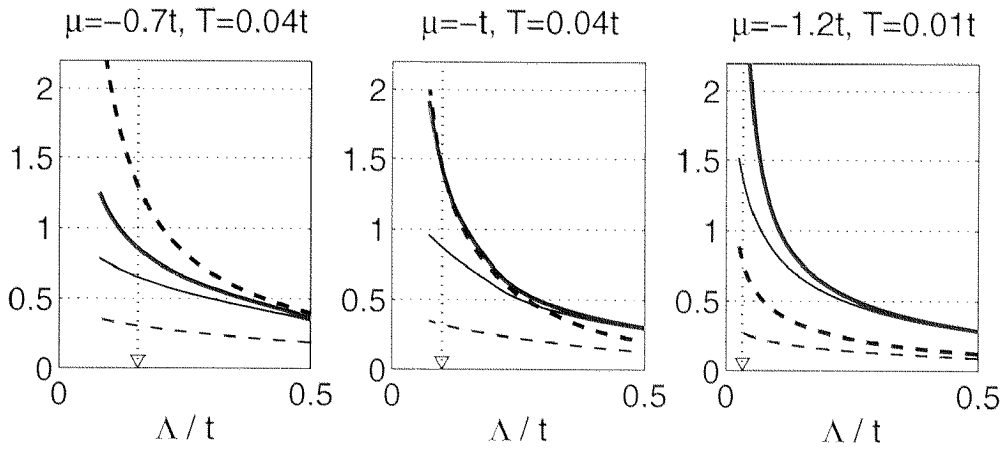

Figure 5.10: *d-wave (heavy solid line) and AF susceptibility(heavy dashed line) for the three different choices of chemical potential and temperature discussed in the text. The thin lines denote the flow of the bare susceptibilities without vertex corrections. The mark at the Λ-axis indicates the scale, where the largest coupling reaches* $10t$.

The uniform spin susceptibility exhibits a similar suppression (see Figs. 5.11 and 5.8) when we approach the instability in this saddle point regime. On the one hand this is plausible because the rapid growth of the d-wave susceptibility signals strong singlet pairing tendencies. On the other hand the AF susceptibility $\chi_s(\pi,\pi)$ seems to diverge as well, from which one might expect long range AF order, i.e. a strong coupling state with nonzero $\chi_s(0)$. Since the RG flow points in a different direction, we argue that for the saddle point regime the more likely candidate is a insulating spin liquid state with strong short range AF correlation but nonzero spin gap. The flow to strong coupling in this regime is caused by the coupling and mutual reinforcement of the d-wave pairing and the Umklapp processes between the broad saddle point regions. Therefore the strong coupling state should feature the singlet pairing of the d-wave channel *and* a strong enhancement of $\chi_s(\vec{q})$ for $\vec{q} \approx (\pi,\pi)$. This is exactly what we observe for χ_{dw} and $\chi_s(\vec{q})$. Moreover due to the extension of the saddle point regions the peak of $\chi_s(\vec{q})$ is very broad around (π,π) and does not sharpen significantly in the flow. Therefore we expect a rather short AF correlation length of 2-3 lattice spacings. This is in contrast to the $t' = 0$ case very close to half filling, where we find sharp peaks in $\chi_s(\vec{q})$ developing around $\vec{q} = (\pi,\pi)$ and where one would expect AF long range order at $T = 0$ (see also Chapter 8).

5.1.3 The approximate nesting regime

The plots on the left in Figs. 5.5, 5.6, and 5.3 show the flow for a higher filling ($\mu = -0.7t$). In this case the leading interactions are Umklapp couplings between the BZ regions where the FS intersects the US and in the BZ diagonals (see red features in Fig.

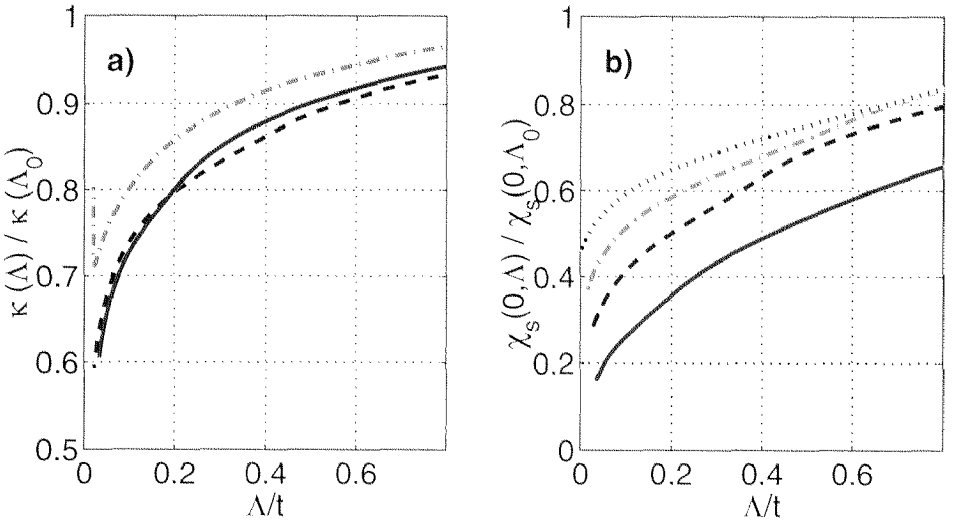

Figure 5.11: *a) Flow of the charge compressibility κ normalized to their value at the initial scale $\Lambda_0 = 4t$ for $\mu = -1.2t$ (dashed dotted line), $\mu = -t$ (solid line) and $\mu = -0.8t$ (dashed line). b) Flow of the uniform spin susceptibilities normalized to their initial values for $\mu = -t$ (solid line), $\mu = -0.8t$ (dashed line), $\mu = -0.6t$ (dashed-dotted line), and $\mu = -0.4t$ (dotted line). For increasing electron density, $\chi_s(0,\Lambda)/\chi_s(0,\Lambda_0)$ is less suppressed at low scales. For all data $T = 0.04t$. These curves were calculated using the RPA scheme for the effective theory below the cutoff.*

5.6 and the green lines in the left plot in Fig. 5.3) while the importance of the vicinity of the saddle points decreases. We call this the *approximate nesting regime*. Here, due to the higher band filling, the dominating FS regions are now further away from the saddle points. As a consequence the coupling between Umklapp and pairing channel decreases and the d-wave pairing processes become less relevant. This can be seen best from the weaker flow of the attractive Cooper couplings in Fig. 5.3. Now the AF susceptibility clearly exceeds the d-wave pairing susceptibility (Fig. 5.10). This signals increasing AF ordering tendencies which are in accordance with sharper (π, π) features in the interactions (see Fig. 5.6), decreasing suppression of $\chi_s(0)$ relative to its initial value (see Fig. 5.11), and a sharper peak of $\chi_s(\vec{q})$ around (π, π). The charge susceptibility is also suppressed like in the saddle point regime, however the FS regions with smallest charge couplings stay fixed to the US and therefore move towards the BZ diagonal if we increase the filling.

5.1.4 Additional remarks on the flow

Importance of the next nearest neighbor hopping: We emphasize that in our RG treatment of the two-dimensional Hubbard model the next nearest neighbor hopping t' is

important for the existence of a sizable saddle point regime. For zero or very small t' the FS is closer to the US in the BZ diagonals and the (π, π) scattering between the rather flat FS faces dominates even more strongly than in our approximate nesting regime with more FS curvature. If we now decrease the band filling, at some point, as pointed out by Zheleznyak et al.[Zheleznyak 1997] and explicitly shown for the two-dimensional case by Zanchi [Zanchi 1997], these processes are cut off at low scales and can only serve as generators of an attractive d-wave initial condition. With t' very small the system crosses rather sharply from a nesting regime into a d-wave dominated regime without going through a saddle point regime in between. A similar transition occurs in electron-doped case discussed in Chapter 7.

Differences to the two-patch flow: A difference to the two-patch analysis of Furukawa et al. is that the saddle point regime, where we observe the ISL signatures in our N-patch calculation, is found at positive temperatures and densities slightly higher than the van Hove density assumed in the two-patch analysis. The reason is that in the N-patch flow the FS parts away from the saddle points reinforce mainly the Cooper channel. Only if the FS really crosses the US there is sufficient low energy phase space for the Umklapp processes which then act together with the Cooper processes leading to the unusual strong coupling flow.

For similar reasons in the 2D system nonzero temperature is helpful for the saddle point regime, although at least the "frozen interactions"-scheme described in Subsection 3.5.2 shows the charge gap tendencies at lowest temperatures as well. Moderate T smears out the FS and provides additional phase space for both the particle-particle processes with small total momentum and the particle-hole processes with momentum transfer (π, π). Especially due to the latter there is a certain temperature range where this thermal phase space gain outweighs the ordinary decrease of the one-loop contributions for increasing T and the critical scale Λ_c is enhanced with respect to its $T = 0$ value.

Apart from the suppression of the total charge compressibility described above there are other potential instabilities in the forward scattering channel. These are described in Section 5.3.

5.2 The ISL scenario

In the last section we have shown that in the saddle point regime the numerical results is consistent with the formation of an insulating spin liquid around the saddle points. Yet we cannot calculate the opening of spin and charge gaps within our one-loop RG scheme. Therefore we will now offer an interpretation of the RG flow by assuming that there exist charge and spin gaps truncating the FS around the saddle points and discuss the consequences of this insulating spin liquid (ISL) scenario.

The stabilization of the ISL in the vicinity of the saddle points opens up a novel channel

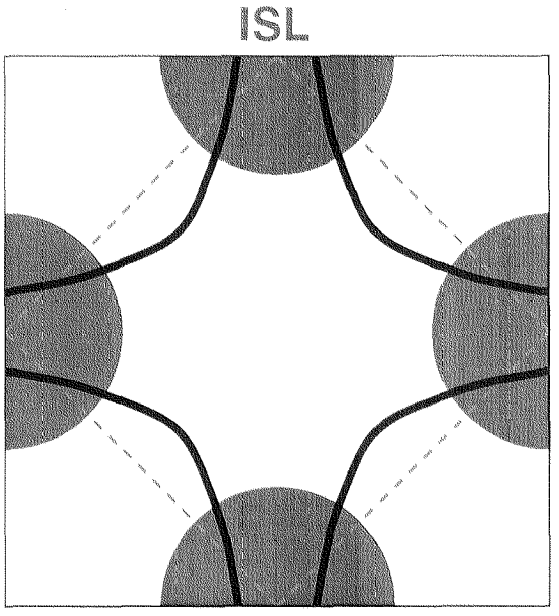

Figure 5.12: *The ISL scenario: The FS is truncated in the semicircles around the saddle points where spin and charge gaps form and it remains open in the BZ diagonals.*

to enhance Cooper pairing on the open parts of the FS. A similar mechanism was recently proposed by Geshkenbein et al. [Geshkenbein 1997] who examined a model with infinite mass preformed pairs existing at higher temperatures also in the vicinity of the saddle points. Let us assume that the ISL has formed in a region (called the A region) around the saddle points at an energy scale $\Lambda_{\rm ISL}$. Then the dominant coupling between the ISL and the open FS parts (called the B regions) will occur through the exchange of zero momentum hole pairs in the Cooper channel. Further it will occur in the d-wave pairing channel, because the flow at scales above $\Lambda_{\rm ISL}$ has already generated a sizable component of this symmetry in the pair scattering. We denote this pair scattering matrix element between the ISL in the A-regions and the open B regions of the FS at the scale $\Lambda_{\rm ISL}$ by V_{AB} . Further let ϵ_A be the energy relative to the chemical potential to add a hole pair to the ISL. Then, at energy scales $\Lambda < \Lambda_{\rm ISL}$, an additional attraction V_{BB} is generated between pairs in the open B regions, which has a pole at

$$\begin{aligned} \Lambda_c^B &= \Lambda_{\rm ISL} \exp\left(-\frac{\epsilon_A}{N_{AB}}\right) , \qquad (5.1) \\ N_{AB} &= n_A \int_{\rm B-FS} \frac{dk}{(2\pi)^2} \frac{V_{AB}^2(\vec{k})}{v_F(\vec{k})} . \end{aligned}$$

Here the integral is over the Fermi surface of the B regions and n_A denotes the number of intermediate states with two additional particles in the A regions per lattice site. This means that although the saddle point regions are insulating they give rise to a d-wave

superconducting instability on the open parts of the FS. There will be two energy scales, a higher one, $\Lambda_{\rm ISL}$, where the ISL forms, and a lower one with a real superconducting transition at Λ_c^B.

Although we do not have a full theory of the strong coupling phase, it is plausible to assume that in the A-regions the charge gap spreads out along the US when the density is increased towards half-filling. This is in analogy to ladder systems which when lightly doped show simultaneously channels with and without charge gap [Rice 1997, Ledermann 2000].

How is the evolution of Λ_c^B with decreasing the doping? It is clear that the charge gap ϵ_A will become larger when we move closer to the Mott state and the number of states n_A in the insulating regions increases. Moreover we should assume that the average V_{AB}^2 does not grow because its flow in the Cooper channel has less scale range to develop due to the increased $\Lambda_{\rm ISL}$ and the B range is limited to a narrowing FS around the nodes of the d-wave. This also decreases the integration range in N_{AB}, so that the exponent ϵ_A/N_{AB} should finally become larger when we approach the Mott state. Therefore from this rough model we expect that Λ_c^B which we associate with the real superconducting T_c will be largest at the band filling where the charge gap just opens up.

Another salient feature of the ISL scenario is the variation of the superfluid weight ρ_s with changes in the doping. As the saddle point regions are insulating, ρ_s will be exclusively given by the size of the open parts of the FS. Therefore ρ_s should be maximal at densities where the ISL starts to form and decrease when we move closer to the half-filled Mott state. The same reasoning holds for the condensation energy which is released at the superconducting transition. However note that a precise calculation would require a true strong coupling theory for the ISL.

5.3 Instabilities in the forward scattering channel

As described in the last sections, the strong coupling flow is mainly dominated by the rapidly growing d-wave and AF processes. Apart from the instabilities associated with these fluctuations, it is worthwhile to analyze other potential singularities of more conventional Landau-Fermi liquid type in the forward scattering channel. In the RG treatment there arises a technical problem for the comparison of these instabilities with the tendencies described in the previous section. The particle-hole bubble at $\vec{q} \approx 0$, which determines the occurrence of instabilities in the forward scattering channel, e.g. in a Stoner description of ferromagnetism, does not contribute to RG flow at scales $\Lambda > T$. For the same reason we have to choose somewhat different methods to obtain the corresponding susceptibilities, as described in Section 3.5.2.

5.3.1 Ferromagnetism

Although nowadays mostly used as a toy model exhibiting strong antiferromagnetic tendencies, the Hubbard model was initially proposed independently by Gutzwiller, Kanamori and Hubbard in order to understand the itinerant ferromagnetism in 3D transition metals (for a review on metallic ferromagnetism, see [Tasaki 1998, Vollhardt 1999]). Generally itinerant ferromagnetism is favored by a large density of states at the FS, as is already clear from the simple Stoner criterion. Therefore one might wonder whether the t-t' Hubbard model with the FS close to the van Hove singularities actually has a ferromagnetic instead of a d-wave superconducting, antiferromagnetic or more complex ground state. Such a state however should be signaled by a divergence of the uniform spin-susceptibility. This is definitely not the case, as one can see from the flow of $\chi_s(0)$ in Fig. 5.8. The flow of the couplings suppresses the uniform spin susceptibility rather than enhancing it. This holds as well in the regions where the Stoner criterion[2] $U\times$density of states ≥ 1 for ferromagnetism is fulfilled for to the bare values of the interaction: if we run the flow down to a certain scale Λ and then calculate the RPA series with the renormalized couplings, $\chi_s(0)$ becomes a finite positive number and gets suppressed to zero with further decrease of Λ. The spin gap tendencies are shown unequivocally by both calculation methods described in Subsection 3.5.2.

The physical reason for this suppression of ferromagnetism are the strong singlet pairing tendencies in the d-wave channel: a small part of the attractive Cooper processes, namely the most attractive ones $\approx (\vec{k}, -\vec{k}) \rightarrow (-\vec{k}, \vec{k})$ enters the forward scattering channel as well. This decreases the average repulsion (which would be U in the simplest isotropic Stoner case) of the processes which enter the RPA denominator. This increasingly narrows the density interval around the van Hove filling where the DOS is large enough to cause a Stoner instability. In fact as the Cooper channel diverges like $\log^2(\Lambda/\Lambda_0)$ at the van Hove filling we expect that it will always dominate the divergence in the forward scattering channel, which is only $\propto \log(\Lambda/\Lambda_0)$. Thus the RG treatment suggests that there is no stable region for ferromagnetism at $t' = -0.3t$. The situation for larger absolute values of t' is discussed in Chapter 8.

5.3.2 Pomeranchuk instabilities

As pointed out by Halboth and Metzner [Halboth 2000], there appears to be a strong tendency towards Labbé-Friedel or Pomeranchuck (for a description inside Landau-Fermi liquid theory, see e.g. [Pines&Nozières]) FS deformations which break the square symmetry of the FS. These are mainly rectangular deformation modes which split the degeneracy of the saddle-points.

In the two-patch model they arise because the flow of interactions is such that the forward

[2] The Stoner criterion typically overestimates the tendency towards ferromagnetism. We show here that even this upper bound for possible ferromagnetism becomes suppressed to zero by the RG flow.

scattering for two incoming particles at the same saddle point (g_4 in the notation of Section 2.3) becomes increasingly attractive while it flows to strong repulsion if the particles are at different saddle points ($2g_2 - g_1$):

$$g_4 \to -\infty \quad \text{and} \quad g_2 \to +\infty \,,$$

g_1 diverges more slowly to $+\infty$.

A uniform external field coupling to the electron charge density at wavevector $\vec{k}$ will be renormalized by Eq. (3.69),

$$\begin{pmatrix} \gamma_c(A) \\ \gamma_c(B) \end{pmatrix} = \begin{pmatrix} \gamma_c^0(A) \\ \gamma_c^0(B) \end{pmatrix} - N_0 \begin{pmatrix} g_4 & (2g_2 - g_1) \\ (2g_2 - g_1) & g_4 \end{pmatrix} \begin{pmatrix} \gamma_c(A) \\ \gamma_c(B) \end{pmatrix} ,$$

where N_0 denotes the density of states at each of the patches A and B. When we invert this equation for $\gamma_c(A)$ and $\gamma_c(B)$, we encounter a singularity if the determinant of the matrix

$$\begin{vmatrix} 1 + N_0 g_4 & N_0(2g_2 - g_1) \\ N_0(2g_2 - g_1) & 1 + N_0 g_4 \end{vmatrix} = (N_0 g_4 + 1)^2 - N_0^2 (2g_2 - g_1)^2$$

becomes zero. From the flow of the forward scatterings described above it is clear that this will be the case for some Λ sufficiently close to Λ_c. This singularity however occurs in the odd channel $\gamma_c^0(A) = -\gamma_c^0(B)$ and does therefore not affect the suppression of the uniform charge compressibility κ in the channel $\gamma_c^0(A) = \gamma_c^0(B)$.

The same result is obtained when we write a Landau functional [Hlubina 1997]

$$\delta E = \frac{1}{2} \sum_{i=A,B} N_0 \Delta_i^2 + \frac{1}{2} \sum_{\substack{i=A,B \\ j=A,B}} N_0^2 f_{ij}^s \Delta_i \Delta_j \tag{5.2}$$

for a $\vec{k}$-space local change Δ_i of the chemical potential at saddle point i. With $f_{AA}^s = g_4$ and $f_{AB}^s = (2g_2 - g_1)$ the energy minimum $\Delta_A = \Delta_B = 0$ becomes unstable against FS deformations with $\Delta_A = -\Delta_B$ for $N_0(2g_2 - g_1 - g_4) > 1$.

For our analysis we will ignore these deformation tendencies because the leading flow to strong coupling occurs in the d-wave and AF channel and not in forward scattering channel which is only driven by the two mutually reinforcing former ones. This means that the energy functional (5.2) is incomplete and does not contain the most important terms, such that we cannot draw conclusions from minimizing (5.2). The consequence from the leading flow of AF and d-wave processes is that the uniform spin and charge couplings are increasingly suppressed and that the forward scattering acquires an anisotropy of the type described above. A FS deformation cannot be ruled out in our approach, yet it appears implausible that this side-effect will determine the strong coupling state of the system. In the saddle point regime when we use the scheme for the modes below the cutoff explained in 3.5.2 the Pomeranchuk pole in $\gamma_c(\vec{k})$ only occurs at scales where the

couplings V_Λ have already exceeded the order of the bandwidth. Further the connection to large-U features of the Hubbard model points towards a destruction rather than a deformation of the FS.

Nonetheless we have checked that a moderate deformation of the FS that breaks the square symmetry and leads to saddle point splittings of the order of the critical scale $\sim 0.1t$ does not invalidate the results described above.

5.4 The one-loop selfenergy and the Fermi surface shift

So far we have completely neglected possible selfenergy corrections to the flow of the interactions. A complete analysis including the full selfenergy is far too complicated, therefore we here restrict ourselves to showing that the shift of the FS caused by the real part of the selfenergy does not become large before the interactions flow to strong coupling. A similar statement can be made for the scattering rate on the FS, discussed in Chapter 6. Here we give a short overview of the results for the RG flow of the Fermi surface with fixed particle number.

In order to obtain the FS flow we calculate in every RG step the change of the one-loop selfenergy given by the contributions in Fig.3.3. Due to the approximations made for the couplings this selfenergy is constant over a single patch and only yields a patch-dependent shift of the Fermi surface. For the modes which to be integrated out in the next RG step there are two choices: One can use the scheme introduced in Chapter 3 and integrate out the modes with respect to their bare dispersion. Then for large FS shifts it might happen that the movong FS hits the energy shell being integrated out and we encounter singularities which one originally intended to avoid by using RG. The other possibility is to use the renormalized dispersion including the scale-dependent FS shift in the cutoff-function, i.e. for the Green's function occurring in the one-loop integrals we write

$$G_{\Lambda,2}(i\omega_n,\vec{k}) = \frac{C\left(\epsilon(\vec{k})+\Sigma_\Lambda(\vec{k})\right)}{i\omega_n-\epsilon(\vec{k})+\Sigma_\Lambda(\vec{k})}\,.$$

This leads to an additional contribution to the single-scale propagator (3.52), which then reads

$$S_{\Lambda,2}(i\omega_n,\vec{k}) = \frac{\dot{C}_\Lambda\left(\epsilon(\vec{k})+\Sigma_\Lambda(\vec{k})\right)+\dot{\Sigma}_\Lambda(\vec{k})\frac{dC_\Lambda}{d\Sigma_\Lambda}}{i\omega_n-\epsilon(\vec{k})+\Sigma_\Lambda(\vec{k})}\,.$$

Here we use this second variant. In order to keep the particle number fixed we adjust the chemical potential after each step. Quite generally we find that the FS parts which have the strongest repulsive scatterings with momentum transfer close to (π,π) develop positive self-energies and are therefore are shifted inwards during the RG flow. The reason for that becomes clear if one considers a model interaction which is sharply peaked and

repulsive at $\vec{Q} = (\pi, \pi)$. For the selfenergy $\Sigma(\vec{k})$ of a particle with wave vector $\vec{k}$ on the FS one primarily has to examine the Hartree term (first term in Fig. 3.3), which is the main contribution for the typical divergence of the couplings. This diagram contains a propagator with a differentiated cutoff function and gives a positive contribution if the state $\vec{k} + \vec{Q}$ is occupied and zero contribution otherwise. After subtraction of the FS average of $\Sigma(\vec{k}_F)$ (or more precisely a constant which keeps the particle number fixed) this yields a positive selfenergy $\Sigma(\vec{k}) > 0$ for particles outside the US (because then in general the state $\vec{k}+\vec{Q}$ is occupied for a FS with the densities and t' values we are interested in) and a negative shift $\Sigma(\vec{k}) < 0$ for states inside the US. In our case the interaction only has a broad peak around (π, π), therefore in general also FS points inside the BZ can be pushed inwards provided they are more affected by this repulsion than the average FS (this happens in the overdoped $\mu = -1.3t$ case). The flow of the the selfenergies with fixed FS close to the instability is shown in Fig. 5.13 b) for different positions on the FS: for the FS points near the saddle points $\Sigma_\Lambda(\vec{k})$ flows to positive values, while for $\vec{k}_F$ in the BZ diagonal it becomes negative. The resulting movement of the FS points if we include $\Sigma_\Lambda(\vec{k})$ in the dispersion, i.e. allow the FS to move, can be seen in Fig.5.13 a). In both cases the density is kept fixed at $\langle n \rangle \approx 0.88$ per site. The data reveal that down to the energy scale where the growth of the couplings exceeds the bandwidth, the movement of the FS is rather small such that it does not affect the qualitative conclusions drawn in the previous sections. One can observe a slight tendency of the FS to become flat, thus remaining in the vicinity of the Umklapp surface and increasing the influence of the Umklapp processes[3].

Our RG results are in qualitative agreement with calculations using a model interaction due to AF spin fluctuations [Yanase 1999] and the FLEX (fluctuation exchange) approximation [Morita 1999].

We note that the one-loop flow of the FS gave no signs of a breaking of the square symmetry related to the potential Pomeranchuk instability described in Section 5.3.

5.5 Discussion and conclusions

With our N-patch renormalization group analysis of the two-dimensional Hubbard model we find indications that the path from a Landau-Fermi liquid-like state to the Mott insulating state may pass through a spin liquid phase with partially truncated FS and incompressible regions around the saddle points. Certainly the above results have to be interpreted with care and are only qualitative as they are an attempt to learn about possible strong coupling states from extrapolating weak–coupling flows. However they demonstrate that the breakdown of a Landau-Fermi liquid through an ISL state with partially

[3] In the $t' = 0$ case close to half filling the states in the BZ diagonal are slightly more affected by the strong (π, π)-repulsion than the states at the saddle points. Therefore the FS expands towards the saddle points, although the trend is weaker than for $t' = 0.3t$.

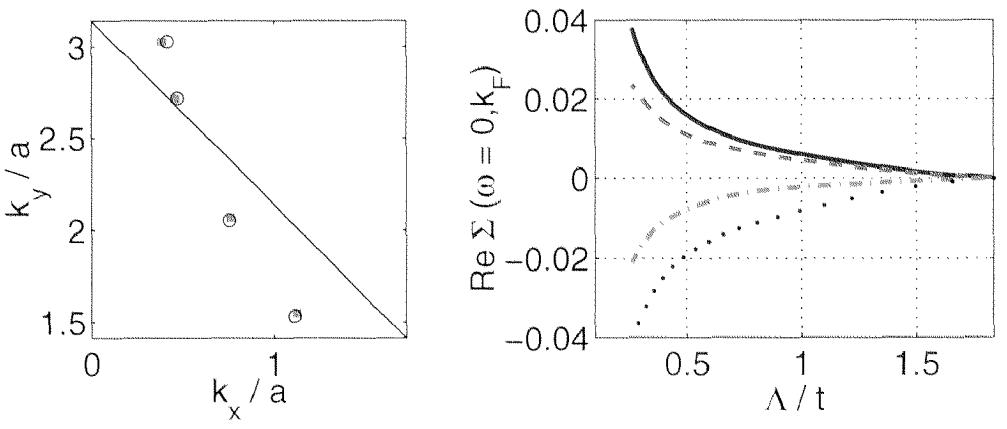

Figure 5.13: *Left: Initial (open circles) and final (squares) FS for* $t' = 0.3t$ *and* $\langle n \rangle \approx 0.88$ *per site. Right: Flow of the selfenergy on the FS (solid line: point closest to the saddle points, dotted line: point closest to BZ diagonal). The flow was stopped when the largest coupling reached the bandwidth* $8t$.

truncated FS is a viable concept, because in the saddle point regime the qualitative features of the ISL, e.g. spin and charge gaps, are visible as tendencies in our weak coupling approach. The essential phenomenon which can be identified as the cause for the ISL in the half-filled two-leg Hubbard ladder and the two-patch model, namely the coupling of AF Umklapp and pairing channel, is found to exist in a sizable temperature and density range also in our improved RG calculation, which includes the entire Fermi surface. We believe that this behavior is robust because it only requires sufficiently large low energy phase space around the saddle points but does not rely on further details of the interaction or dispersion relation.

What remains to be clarified in future work is when this interplay between pairing and Umklapp processes, which frustrates symmetry-breaking tendencies and thus leads to an ISL, indeed represents an energetically favorable situation for the system. Another interesting and related aspect is the question of the precise conditions for which the overlap between the channels becomes too small, such that at $T = 0$ the system can still undergo a transition into a symmetry-broken state with presumably renormalized properties. In our calculation such symmetry-broken states are suggested on either side of the saddle point regime, e.g. in the d-wave dominated phase or closer to half-filling in the approximate nesting regime.

Our approach certainly bears some appealing features when compared to the high-T_c cuprates, briefly discussed in Subsection 5.2. The most attractive point of the ISL is that it can describe the crossover from a system where the superfluid density ρ_s is determined by the number of electrons to a system with ρ_s given by the size of the open parts of a truncated FS which scales with the number of holes.

However note that especially very close to half filling, in the approximate nesting regime, our description will be much too simple, as interaction effects which are not taken into account will become large. On the other hand further away from half filling, in the saddle point regime, we are convinced to give a reasonable qualitative description of the driving forces for the breakdown of the Landau-Fermi liquid. Due to the mutual reinforcement between Cooper and Umklapp channel d-wave pairing correlations appear in a natural way at an enhanced scale on the threshold to the Mott state. If the insulating tendencies are strong enough they will lead to the ISL formation around the saddle points.

Finally we note that the ISL concept might provide a microscopic basis for understanding the ARPES results on the cuprates which clearly show the truncation of the FS around the saddle points [Norman 1998] and also for phenomenological models [Ioffe 1998] which have proven to be plausible descriptions of the transport properties of the normal state of the underdoped high-T_c cuprates. These points will be discussed in the next chapter.

Chapter 6

Quasiparticle Scattering Rates

In the previous chapter we have argued that in the saddle point regime the Fermi surface becomes truncated around the saddle points while it appeared that the quasiparticles in the BZ diagonals persist, mainly because the charge compressibility of these FS parts did not show signs of strong suppression. Such a partial destruction of the Fermi surface should also be observable in the selfenergy on the FS. A calculation of the full self-energy $\Sigma(\vec{k},\omega)$ is beyond our possibilities, in this chapter we restrict ourselves to the qualitative behavior of the imaginary part of the electronic selfenergy $\mathrm{Im}\Sigma(\vec{k}_F,\omega=0)$ on the FS. Above the critical temperature where the partial charge gap has not opened up, $\mathrm{Im}\Sigma(\vec{k}_F,\omega=0)$ gives the scattering rate for the quasiparticles.

According to model calculations by Ioffe and Millis [Ioffe 1998] most transport experiments of the optimally doped cuprates can be properly described by assuming a strong anisotropy in the scattering rate. The anisotropy is such that the quasiparticles around the saddle points scatter strongly and their spectral weight becomes smeared out while the quasiparticles in the BZ diagonal are only subject to a weak Fermi-liquid-like scattering. Our RG flow to strong coupling with ω independent divergent coupling constants can certainly not give reliable information about the frequency dependence of the self-energy, nevertheless its $\vec{k}$-space resolution is rather good. Therefore we should observe a strong angular dependence of $\mathrm{Im}\Sigma(\vec{k}_F,\omega=0)$ as result of our calculations.

Angular resolved photoemission allows to measure the temperature dependence of Im $\Sigma(\omega=0,\vec{k}_F)$ directly from the width of the quasiparticle peaks. For optimally doped Bi 2212, Valla et al. [Valla 2000] found a linear-T dependence almost everywhere on the FS. For a comparison we calculate the quasiparticle scattering rates at high temperatures, where the RG flow does not diverge.

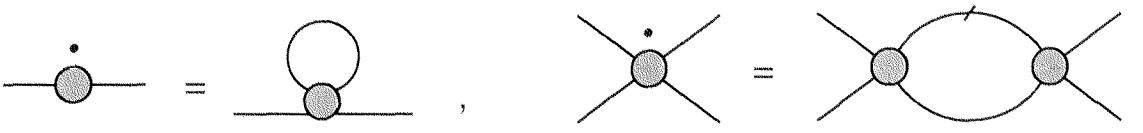

Figure 6.1: *The one-loop RG equations for two - and four-point vertex function.*

6.1 How to obtain Im Σ from the RG flow

The truncated RG equations for the selfenergy and the four-point vertex are shown again in Fig. 6.1. We want to calculate the imaginary part of the selfenergy. Here the technical problem is that we have neglected all frequency dependencies of the four-point vertex, hence the $\gamma_{4,\Lambda}$ occurring in the one-loop term contribution for Σ at scale Λ is a real quantity and the diagram does not give an imaginary part. We can repair this deficiency to a large extent if we insert the solution of the RG equation for $\gamma_4(\Lambda)$ for the approximate vertex. This effectively yields a two-loop term which corresponds to a two-particle–one-hole intermediate state and which, after analytical continuation gives a non-vanishing imaginary part. Moreover we find that these contributions are the leading ones, for all neglected contributions from further insertions of one-loop diagrams at the vertices have intermediate states with a number of intermediate particle larger than 3 which can be expected to give only small contributions due to phase space restrictions. If we ignored the flow of the coupling constants and we integrated the obtained expression down to $\Lambda = 0$, we would obtain the two-dimensional Landau-Fermi liquid selfenergy.

Formally this reads as follows (compare Eq. (3.51):

$$\Sigma_{\Lambda=0}(\vec{k}_F, i\omega) = \int_{\Lambda_0}^{0} d\Lambda \int \frac{d^2k'}{(2\pi)^2} \sum_{i\omega'} \left[-2V_\Lambda(\vec{k}_F, \vec{k}', \vec{k}_F) + V_\Lambda(\vec{k}_F, \vec{k}', \vec{k}')\right] S_\Lambda(\vec{k}', i\omega')$$

For V_Λ we substitute the integrated version of Eqn.(3.53), corresponding to inserting the one-loop diagram on the right side of Fig. 6.1 into the self-energy graph on the left side. Then we get a second integral over $d\Lambda'$:

$$\Sigma_{\Lambda=0}(\vec{k}_F, i\omega) = \int_{\Lambda_0}^{0} d\Lambda \int_{\Lambda_0}^{\Lambda} d\Lambda' \sum_{\substack{\text{internal wavevectors} \\ \text{frequencies} \\ \text{diagrams}}} V_{\Lambda'} G_{\Lambda'} S_{\Lambda'} S_\Lambda V_{\Lambda'} \qquad (6.1)$$

In order to keep it simple we have suppressed the arguments of the four-point vertices and propagators in this expression. The integrand contains two four-point vertices $V_{\Lambda'}$, one single scale propagator $S_{\Lambda'}$ and one full propagator $G_{\Lambda'}$ at scale Λ'. The only Λ-dependence is in the differentiated cutoff-function $\dot{C}(\Lambda)$ of the original single-scale

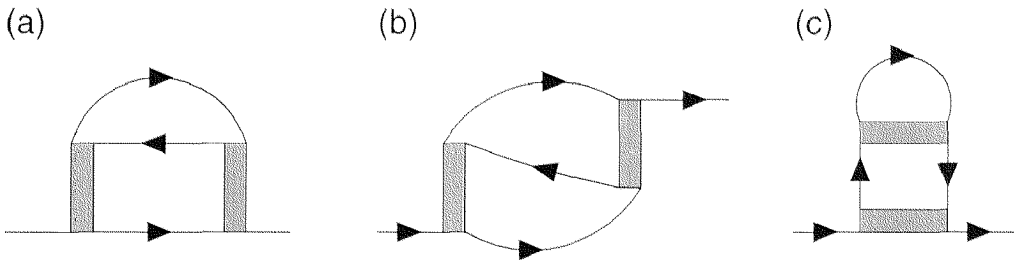

Figure 6.2: *The different diagrams for the two-loop selfenergy. Diagrams (a) and (b) give contributions to the imaginary part of the selfenergy, contributions of type (c) are real for external frequency $\omega + i\delta$. There are 3 other diagrams of type (c) with different orientation of the vertices which are not shown here.*

propagator S_Λ. Therefore (6.1) has the structure

$$\Sigma_{\Lambda=0}(\vec{k}_F, i\omega) = \sum_{\substack{\text{internal wavevectors}\\ \text{frequencies}\\ \text{diagrams}}} \int_{\Lambda_0}^{0} d\Lambda\, \dot{C}(\Lambda) \int_{\Lambda_0}^{\Lambda} d\Lambda'\, R(\Lambda')\,.$$

The double integral is numerically expensive, but we can get rid of it by a partial integration, resulting in

$$\Sigma_{\Lambda=0}(\vec{k}_F, i\omega) = \sum_{\substack{\text{internal wavevectors}\\ \text{frequencies}\\ \text{diagrams}}} \int_{\Lambda_0}^{0} d\Lambda\, \left[C(0) - C(\Lambda)\right] R(\Lambda)\,. \tag{6.2}$$

The remainder $R(\Lambda)$ contains one single scale propagator at Λ and a propagator for modes above Λ. The difference of cutoff functions in the rectangular brackets means that the third of the three internal lines has its support on modes below the cutoff. The form (6.2) only contains a single Λ-integral and the vertex functions at Λ. Therefore it can be integrated along with the flow of the four-point vertex. Note however that for consistency with (6.1) we should always integrate out the full scale range.

Diagrammatically the insertion of the one-loop flow into the one-loop diagram for the selfenergy yields three topologically different diagrams which are shown in Fig. 6.2. Each of these three diagrams gives 6 contributions: one of the internal line contains modes above Λ, another modes at Λ, and the third below Λ.

Since we are interested in the imaginary part of the selfenergy we perform an analytical continuation onto the real frequency axis: the integrand of the two diagrams (a) and (b) in Fig. 6.2 contains the factor

$$\frac{1}{i\omega - \epsilon_1 - \epsilon_2 + \epsilon_3}$$

which upon replacing $i\omega \to \omega + i\delta$ with $\omega = 0$ yields an imaginary part $\propto \delta(\epsilon_1 + \epsilon_2 - \epsilon_3)$. The δ-function is smeared with a width $\approx 0.2T$ for the numerical treatment.

One can show that for constant vertices this scheme is equivalent to the calculation of the bare two-loop diagram. Thus for a non-divergent flow we would obtain two-dimensional Fermi-liquid results. In our case the flow goes to strong coupling, and this leaves two possibilities for the analysis: either we choose a high temperature such that the couplings do not become too large, then we can apply the above scheme down to zero scale and obtain an estimate for the imaginary part of the selfenergy above the strong coupling phase. The other option is, if we want to analyze the situation in the strong coupling regime, to stop the flow of the couplings at some scale Λ_{freeze} and integrate the flow down to zero scale with fixed couplings. We can then vary Λ_{freeze} and thus obtain the change in the imaginary part of the selfenergy due to the flow of the couplings. This will tell us on which FS parts the interaction destroys the quasiparticles most and we will e.g. find that the quasiparticles in the BZ diagonals are not affected by strong scattering.

6.2 Results for high temperatures

Typical result for the saddle point regime above the critical temperature are shown in Fig. 6.3. The temperature was chosen such that the couplings V_Λ do not become too large, for the lowest T shown the maximum coupling reaches $\approx 11.5t$. This is already larger than the bandwidth, but this high value is only reached at low scales and most couplings remain smaller. Therefore the results should be qualitatively correct.

In Fig. 6.3 the anisotropy in the scattering rate is clearly observable but not too pronounced, the maximum ratio between Im Σ at the saddle points and in the diagonals at $\pi/4$ is ≈ 2.

The temperature dependence of Im $\Sigma(\vec{k}_F, \omega = 0)$ is shown in Fig. 6.4 for $\mu = -1.1t$ which is above the saddle point regime and close to the van Hove doping at $\mu = -1.2t$. All curves for the different positions on the Fermi surface show an almost linear increase with T. This behavior is qualitatively consistent with the ARPES results by Valla et a. [Valla 2000] mentioned in the beginning. In comparison with the model assumptions in [Ioffe 1998] we note that our calculations at temperatures above the flow to strong coupling yield a smaller anisotropy in the scattering rates and no T^2 behavior for the quasiparticles in the BZ diagonal. Our data resemble more FLEX[1] results obtained by Altmann et al. [Altmann 1997] and Kontani et al. [Kontani 1999]. The latter group was able to describe resistivity and Hall coefficient in qualitative agreement with the experiments. For high temperatures the similarity between FLEX calculations and our RG analysis is not accidental because for $T > T_c$ when the flow does not diverge, the main scattering occurs in the (π, π) spin fluctuation channel where the typical FLEX

[1] FLEX stands for fluctuation exchange approximation. It is an iterative calculation of RPA charge and spin fluctuations using Green's functions containing a selfenergy obtained with an interaction including the bare repulsion and the exchange of spin and charge fluctuations. In this scheme Cooper pair fluctuations are not included.

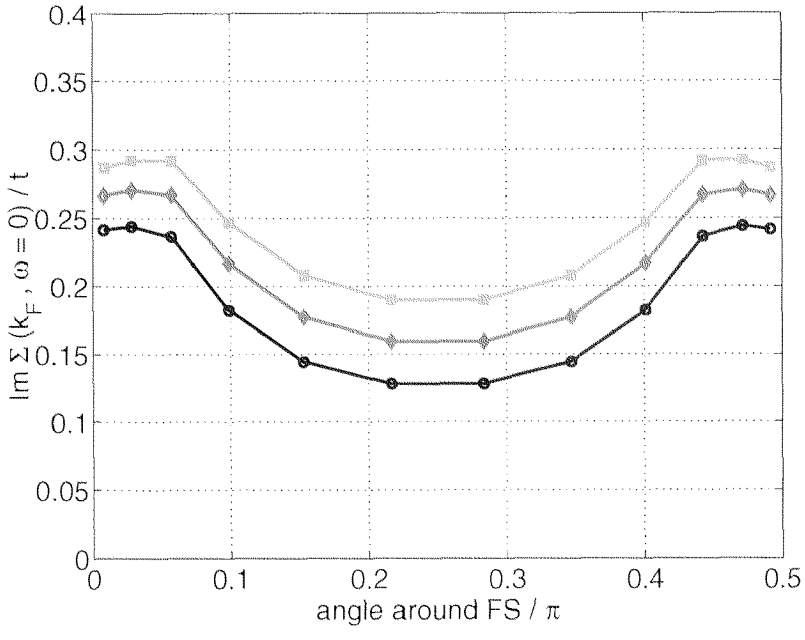

Figure 6.3: *Imaginary part of the selfenergy versus angle around the FS in the saddle point regime at $\mu = -1.1t$ for different temperatures above the instability. The lower line (circles) corresponds to $T = 0.15t$, the middle line (diamonds) to $T = 0.18t$ and the upper line is at $T = 0.21t$. For $T = 0.15t$ the largest coupling at $\Lambda = 0$ is $\approx 11.5t$, for $T = 0.21t$ they reach $\approx 8.9t$. The saddle points are located at angles 0 and $\pi/2$.*

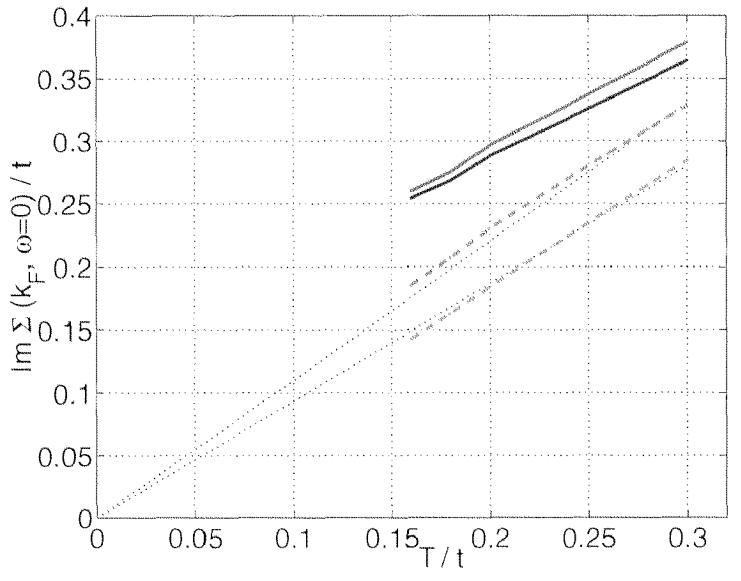

Figure 6.4: *Temperature dependence of imaginary part of the selfenergy at four different positions on the FS, for* $\mu = -1.1t$ *and* $t' = -0.3t$. *The dashed lines belong to points in the BZ diagonal, the solid lines to points closer to the saddle points.*

schemes focus on.

From a theoretical point of view the linear-T dependence is not too surprising because already the bare two-loop diagram with unrenormalized couplings yields this behavior if the band filling is sufficiently close to the van Hove filling. Hence it should be considered as an effect of the van Hove singularities and does not immediately imply a breakdown of Landau-Fermi liquid theory in the sense that the low energy excitations can still be particles with the same quantum numbers as non-interacting electrons, only their width (which remains smaller than πT) does not decrease faster than temperature for $T \to 0$. As recently pointed out by [Kastrinakis 2000] in a Fermi-liquid model the linear-T dependence holds for $T > (\mu - \mu_{\text{vanHove}})/4$, where μ_{vanHove} is the chemical potential at the van Hove filling. Our calculation shows that the RG flow of the interactions does not change this T-linearity.

These results give estimates for the quasiparticle lifetime. No attempt was made to calculate transport lifetimes determining the conductivity which would require computing the vertex corrections for coupling to charged currents through the effective interaction. However for densities close to the van Hove filling the unrenormalized velocities of the quasiparticles close to the saddle points are small and will be further diminished by the scattering between the saddle point regions. Thus we expect that the in-plane transport will be mainly given by the quasiparticles in the BZ diagonals and - if the vertex corrections do not introduce additional temperature dependencies[2] - follow a similar

[2]FLEX calculations [Kontani 1999] show that vertex corrections are important for the T-dependence

temperature dependence as the scattering rates in these regions.

6.3 Results in the strong coupling regime

For lower temperatures the couplings flow to strong coupling at a non-zero critical scale Λ_c . Therefore we cannot integrate the flow down to zero scale and thus do not obtain a good approximation for Im Σ. For energies below the Λ_c the selfenergy diverges together with the couplings and we expect that the quasiparticles will be at least partially destroyed.

Although we cannot really access this strong coupling region, we can gain some insight on how this quasiparticle destruction takes place by considering the change in the two-loop selfenergy through the flow of the couplings by the method described in the previous section. The result for $\mu = -t$ and $T = 0.04t$ is shown in Fig. 6.5. If we freeze the flow of the four point vertices V_Λ already at high scales, we basically obtain the bare two-loop selfenergy. There, the anisotropy between saddle point regions and BZ diagonals due to density-of-states effects is small. If we now subsequently include the flow of V_Λ, the scattering rate for quasiparticles around the saddle points grows strongly. For the quasiparticles in the BZ diagonals the scattering rate is not much affected by the flow of the couplings. Thus again again the most plausible interpretation of the RG results is a breaking up of the FS into two distinct regions, just like in the calculation of the charge coupling in the last chapter: around the saddle points, the quasiparticles are subject to divergent scattering processes, there we also find the strong suppression of the compressibility. In the BZ diagonals which appeared to remain compressible, the scattering rate stays in the weak coupling range, thus we expect that the FS remains untruncated in these regions.

of the Hall coefficient but do not change the qualitative behavior of the in-plane resistivity.

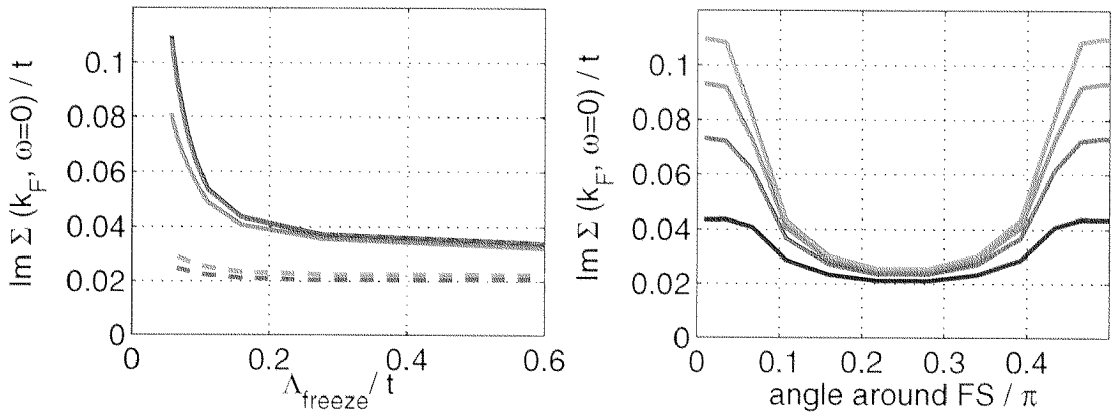

Figure 6.5: *Left: Change of the scattering rate through the flow of the interactions V_Λ for different positions on the Fermi surface. Λ_{freeze} is the scale below which the interactions are kept constant. Right: Angular variations of Im $\Sigma(\vec{k}_F, \omega = 0)$ with $\vec{k}_F$ varying on the FS from one to the next saddle point. The different lines shows $\Sigma(\vec{k}_F, \omega = 0)$ with the couplings stopped at $V_{\Lambda,\max} = 6t$ (bottom line), $9t$, $12t$ and $15t$ (top line). For both plots parameters are chosen to place the 48×3 system in the saddle point regime: $\mu = -1.1t$ and $T = 0.04t$.*

Chapter 7

The Flow to Strong Coupling for Densities Larger than One

In this chapter we analyze the numerical results for the strong coupling flow at band fillings larger than one electron per lattice site. The value of the next nearest neighbor hopping is kept at $t' = -0.3t$. This has the consequence that for $\langle n \rangle > 1$ the FS is far away from the saddle points, therefore the intrinsic coupling between d-wave and AF processes does not occur at the FS (yet it is still present as we will see). Thus on the electron-doped side the flow to strong coupling does not lead to an ISL but is a simple crossover: either dominated by AF processes in the BZ diagonal, which become large at a high energy scale, or, if they get cut off further away from half-filling, by $d_{x^2-y^2}$ Cooper pair processes diverging at a low energy scale. We will focus on a small range of chemical potentials around $\mu = 0$ ($\sim 20\%$ electron doping) because for this the value the FS loses its intersection with the US upon further increase of the electron density, and this changes the strong coupling flow significantly.

7.1 The flow to strong coupling around $\mu = 0$

7.1.1 Flow of the couplings

Again we start the RG flow at $\Lambda_0 \approx 4t$ with initial value $U = 3t$ for the interaction. Two typical examples for the flow of d-wave and AF couplings are shown in Fig. 7.3. As in the hole-doped case we find a flow to strong coupling at high energy scales as long as the FS intersects the US. Now the leading flow over the the largest part of the scale range arises from couplings in the BZ diagonal, where the FS is close to the US. The couplings which grow fastest are Umklapp and other processes which involve momentum transfer (π, π) and drive the AF susceptibility. They give rise to a sharp nesting feature as can be seen in Fig. 7.3.

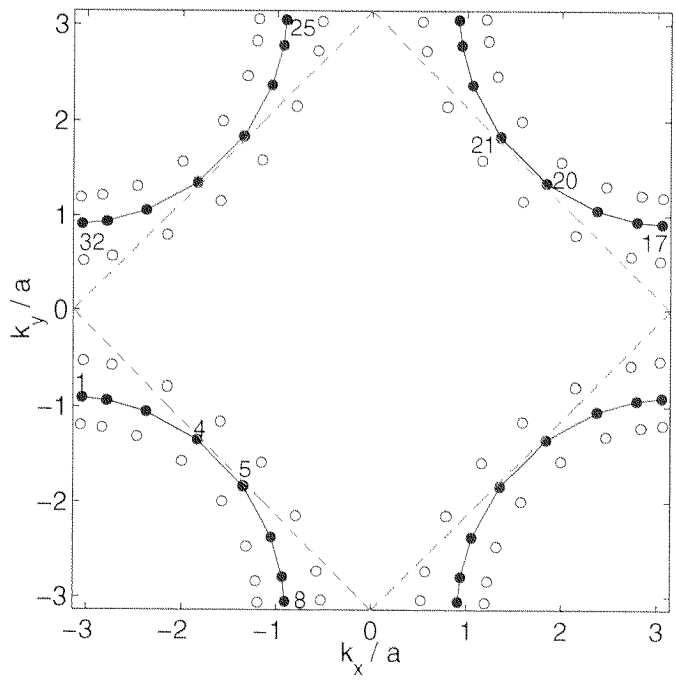

Figure 7.1: *Fermi surface in electron-doped regime at $\mu = -0.04t$ for which the flow is analyzed in detail below. The filled and empty circles show the 32×3 points for which the flow is calculated. The FS intersects the US (red dashed line) for $\mu \leq 0$.*

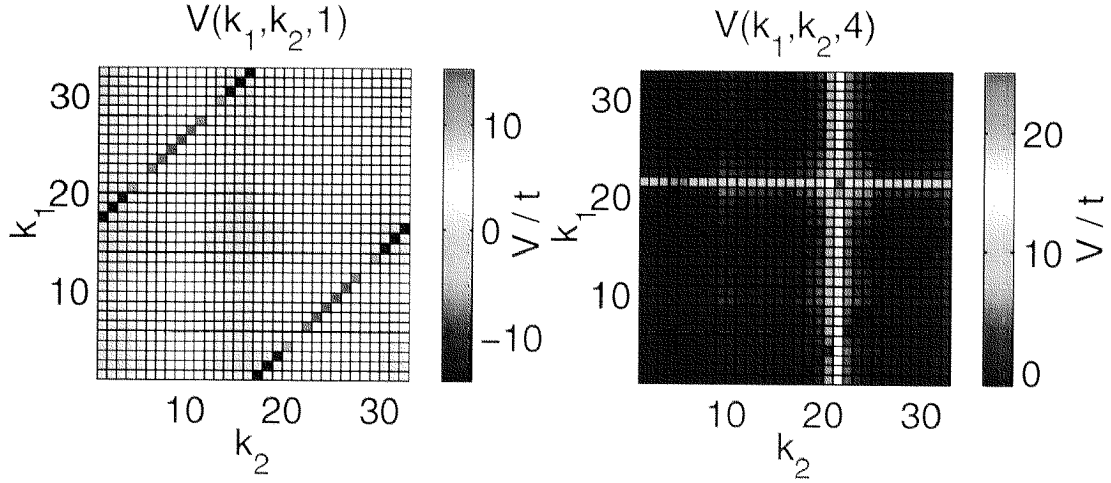

Figure 7.2: *Snapshot of the couplings $V_\Lambda(k_2, k_2, k_3)$ on the electron-doped side at $\mu = 0.04t$ (left plot, first outgoing wavevector k_3 fixed at point 1) and $\mu = -0.06t$ (right plot, first outgoing wavevector k_3 fixed at point 4 in the BZ diagonal), $T = 0$ in both cases. The colorbars denote the strength of the coupling. The diagonal features in the left plot belong to $d_{x^2-y^2}$ Cooper processes with $\vec{k}_1 + \vec{k}_2 = 0$. The sharp vertical nesting feature in the right plot occurs for $\vec{k}_2 - \vec{k}_3 \approx (\pi, \pi)$.*

The flow of the AF couplings consistently continues the behavior observed in the approximate nesting regime for small hole-doping. Nonetheless it should be noted that although for initial interaction $U = 3t$ these AF couplings flow out of the perturbative range at rather large scales (see also Fig. 4.8), if we continue the RG scheme, the flow does not diverge as rapidly as it does in the hole-doped parameter region. We attribute this behavior to the FS curvature which with decreasing scale subsequently reduces the available phase space for the (π, π) processes.

In the electron-doped case for $\mu \approx 0$ the saddle points are already at sizable band energy $\approx 4t'$ below the Fermi energy such that one would not expect them to participate in the RG flow at low scales. Yet the opposite appears to be the case, as one can see from Fig. 7.3. When we increase the band filling such that the FS loses its intersection with the US, the AF couplings between the BZ diagonals (solid lines in the left plot) get cutoff. Then the only processes diverging at comparably low scales ($\Lambda_c \sim 10^{-5}t$) are the d-wave Cooper processes. The dashed lines denote the d-wave processes between points on the FS. The leading flow is now given by vertices connecting the BZ regions directly at the saddle points, shown as dotted lines, still with a $d_{x^2-y^2}$ form factor, as shown in Fig. 7.4. The reason is clear: these vertices have zero incoming total momentum, i.e. are driven by the particle-particle loop with intermediate particles on the FS. But they also have their external legs at the saddle points, hence they couple into the AF channel, which leads to an additional enhancement with respect to the Cooper processes on the FS which do not couple to the (π, π) channel.

These findings indicate that for the given situation the special location of the saddle points with the coupling to both AF and d-wave channel starts to dominate over the underlying energy landscape and determines the flow and the correlations developing at low scales[1]. For the excitations at the FS the *off-shell* processes play a similar role as the ISL regions at the saddle points described in section 5.2: they provide a pool of virtual Cooper pairs which enhances the flow of the *on-shell* processes between points on the FS. On the other hand, since the Umklapp processes between the saddle points are off-shell, they do not give rise to a reduced compressibility at the FS. Similarly the growth of the d-wave processes now takes place at much lower energy scales than the mutual reinforcement in the saddle point regime, where the coupling to the AF channel occurs on-shell. From this perspective in the electron-doped case the $d_{x^2-y^2}$ component appears to be far from being the optimal symmetry for an unconventional pairing being driven by the AF processes, but Fig. 7.4 shows that the pair scattering is still dominated by this symmetry. A d_{xy} component with maximum gap in the BZ diagonals does not occur because in order to generate such a component the predominant repulsive scattering should arise around the momentum transfers $(0, \pi)$ and $(\pi, 0)$ and not for (π, π) as is the case for obvious reasons.

[1] Yet it should be noted that from our study we cannot tell whether the modes at the saddle points are still well defined in view of their distance to the FS. We calculate amputated vertices, while observable correlations involve full propagators at the external legs of the vertices.

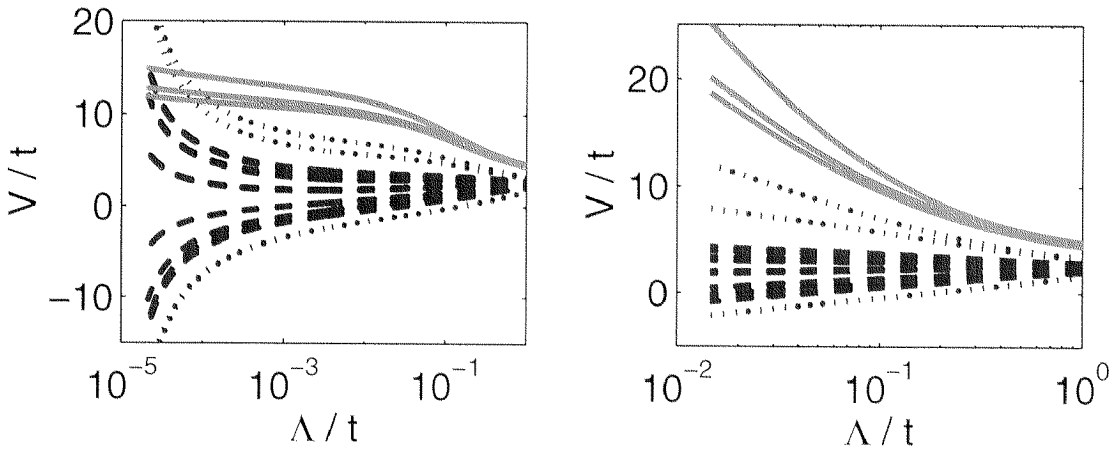

Figure 7.3: *Flow on the electron-doped side at $T = 0$ for $\mu = 0.04t$ (left plot) and $\mu = -0.06t$ (right plot, closer to half-filling). The solid curves show Umklapp and other AF processes between the BZ diagonals, the dashed curves are Cooper processes on the FS and the dashed-dotted curves denote Cooper processes between the saddle point regions inside the FS.*

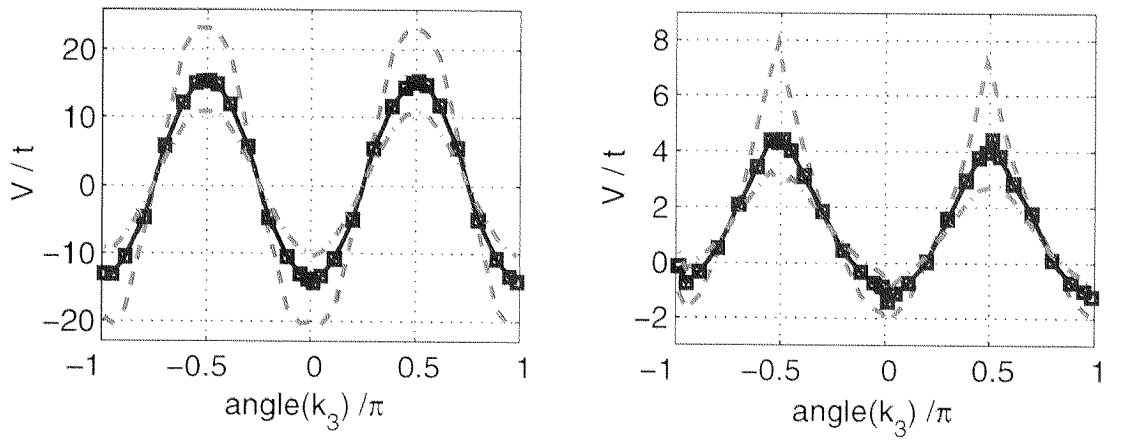

Figure 7.4: *k_3-dependence of the pair scattering $V_\Lambda(\vec{k}_1, -\vec{k}_1, \vec{k}_3)$ with $\vec{k}_1$ fixed at point 1. The solid line stands for incoming wavevectors on the FS, the flat dashed line for wavevectors at band energy $-0.4t$, and the dashed-dotted line denotes wavevectors outside the FS with band energy $0.4t$. The plot on the left (right) side is for $\mu = 0.04t$ ($\mu = -0.06t$) and $T = 0$.*

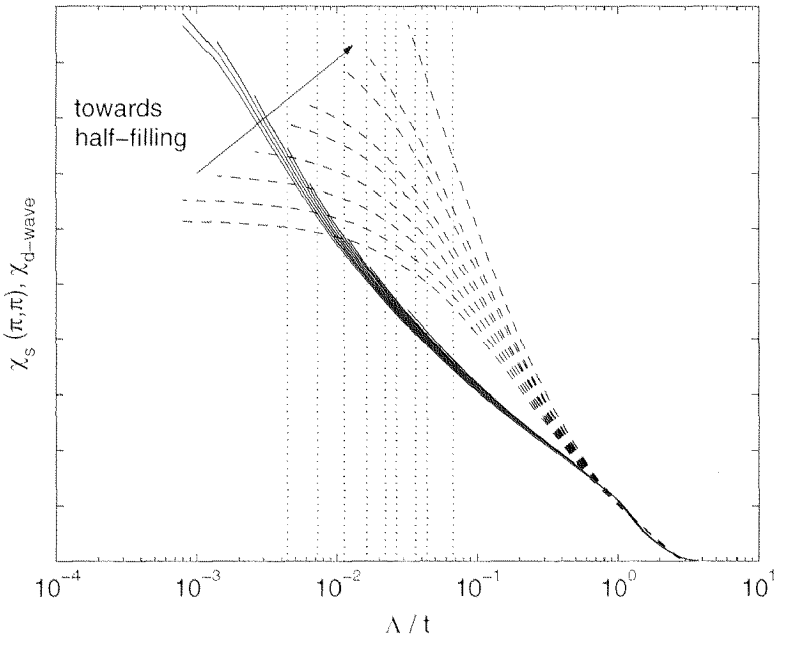

Figure 7.5: *Flow of d-wave (solid line) and AF (broken line) susceptibilities in electron-doped regime at* $T = 0.001t$. *The different lines correspond to values of the chemical potential between* $\mu = 0.08t$ *and* $\mu = -0.01t$. *For the latter value which is closest to half-filling,* $\chi_s(\pi, \pi)$ *grows most strongly.*

7.1.2 Flow of the susceptibilities

As already foreshadowed in the flow of the couplings the competition between AF and d-wave susceptibility is a very unequal one. If the FS intersects the US the nesting AF processes flow to strong coupling before the FS becomes noticeable and the d-wave component is irrelevant. Only if the FS loses contact with the US or is sufficiently curved the growth of the AF processes is slowed down and cut-off at low scales, the d-wave component will determine the low-energy physics. This can be nicely seen from the flow of AF and d-wave susceptibilities, shown in Fig. 7.5. With increasing chemical potential or distance to half-filling, the growth of the AF susceptibility becomes weaker and weaker. The actual range of chemical potentials where this cutoff occurs is rather small, $0 \leq \mu \leq 0.1t$, for initial $U = 3t$ and $t' = -0.3t$: the flow is very sensitive to the location of the FS with respect to the US. The d-wave susceptibility is only weakly coupled to the AF channel and thus does not change much within this small doping range. If μ is sufficiently large, the growth of $\chi_{d-\text{wave}}$ will exceed the growth of $\chi_s(\pi, \pi)$ when the magnitude of the couplings reaches the bandwidth.

In the saddle point regime of the hole-doped case the suppression of the uniform spin and charge susceptibilities around the saddle points lead us to the suggestion that spin and charge gaps will open up in the true strong coupling phase. In the electron-doped filling range, no such particular behavior is found. In Fig. 7.6 we show the flow of the coupling

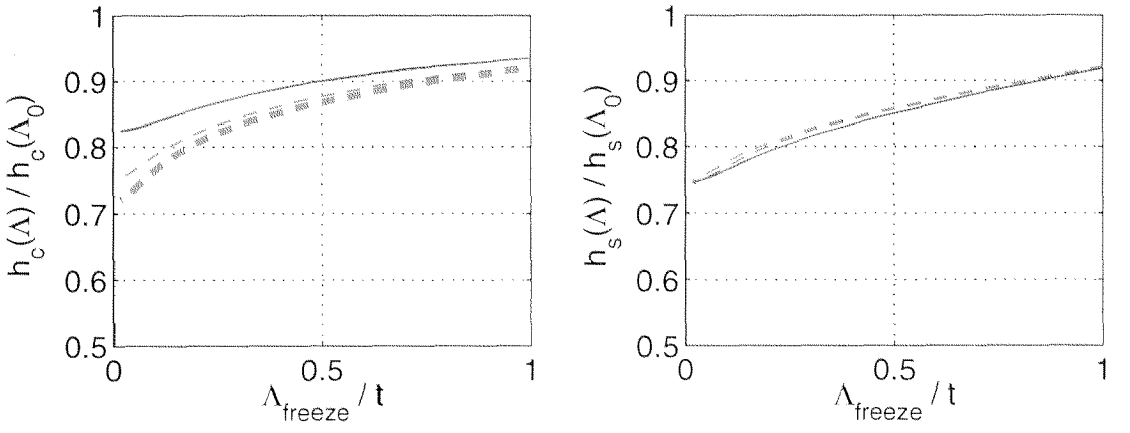

Figure 7.6: *Change of the charge $\gamma_c(\vec{k})$ (left plot) and spin couplings $\gamma_s(\vec{k})$ (right plot) normalized to their initial values of quasiparticles with wave vector $\vec{k}$ on the FS as the electronic interactions flow to strong coupling from a 32×3 point calculation at $\mu = -0.1t$ and $T = 0.04t$. The different lines are for points close to the saddle points (solid lines), and points closer to the BZ diagonal (dashed lines).*

to uniform charge and spin fields for different points on the FS. Nowhere on the FS there are signs for spin or charge gaps. Due to the dominance of Umklapp processes between the BZ diagonals, the charge coupling in the BZ diagonals is somewhat smaller than the values away from the diagonals, but the suppression is very weak. To summarize the flow of the susceptibilities is less complex than in the saddle point regime. The behavior of the uniform susceptibilities does not question scenarios for the true strong coupling state based on the flow of the AF and d-wave susceptibilities only.

7.2 Results for the quasiparticle scattering rate

The quasiparticle scattering rate can be analyzed by the method described in Chapter 6. In Fig. 7.7 we briefly show the results obtained at higher temperatures where the flow does not exceed the order of the bandwidth. There are several striking differences compared to the results obtained in the saddle point regime: first the overall magnitude of $\mathrm{Im}\Sigma(\vec{k}_F, \omega = 0)$ at a given temperature is much smaller, almost by an order of magnitude. We attribute this to the comparably small density of states around the FS, the van Hove singularities are far away from the FS. Second the temperature dependence is far from being linear and appears to consistent with a T^n $(n > 1)$ behavior at low temperatures if the flow would not exceed the bandwidth. Further the FS parts which feel the strongest scattering are now in the BZ diagonal (see right plot in Fig. 7.7 for angular dependence). This is consistent with the flow of the interactions which grow fastest in these regions. The anisotropy of the scattering rate is however less pronounced than in the hole-doped case.

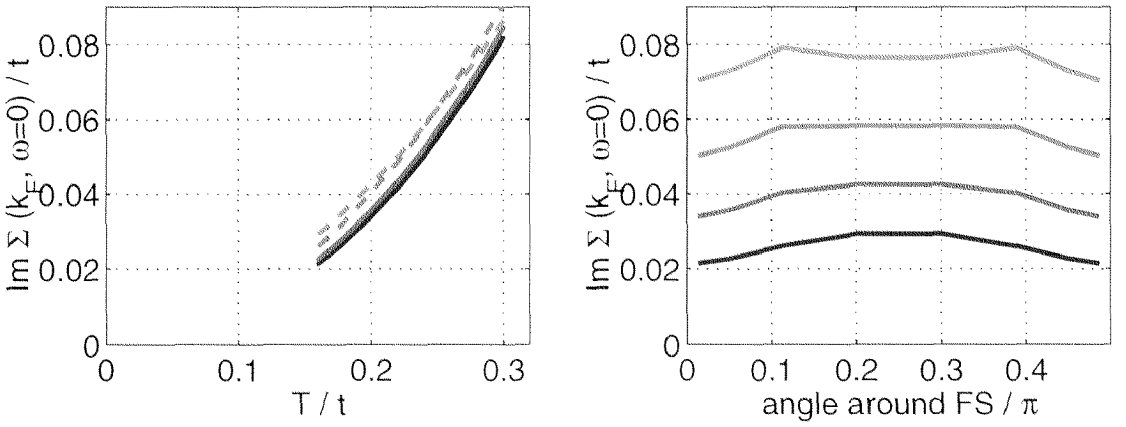

Figure 7.7: *Left: Temperature dependence of imaginary part of the selfenergy at four different positions on the FS. The dashed lines belong to points in the BZ diagonal, the solid lines to points closer to the saddle points. Right: Angular variations of Im* $\Sigma(\vec{k}_F, \omega = 0)$ *with* $\vec{k}_F$ *varying on the FS from one to the next saddle point. The different lines show* $\Sigma(\vec{k}_F, \omega = 0)$ *at different temperatures from* $T = 0.16t$ *(bottom line) to* $T = 0.28t$ *(top line). The data in both plots is obtained by a* 32×3 *system with* $t' = -0.3t$ *and* $\mu = 0$.

7.3 Summary and discussion

The flow to strong coupling on the electron-doped side of the t-t'-Hubbard model with $t' = -0.3t$ turns out to be very different from the flow on hole-doped side. In the latter case we found a saddle point regime with intrinsically coupled d-wave and AF channels diverging at the same high energy scale, accompanied by signs for spin and charge gap formation around the saddle points. In contrast with that the flow on the electron-doped side is an extreme case of an unequal competition of two weakly coupled channels with different characteristic energy scales.

In Fig. 7.8 we summarize the dependence of the instability on temperature and chemical potential. For chemical potential $\mu < 0.03t$ (which corresponds to $\langle n \rangle \approx 1.21$ per site) we find an AF dominated instability with comparably high critical temperature T_c (above T_c we can integrate down to $\Lambda = 0$ with all couplings staying smaller[2] than $15t$.). For larger chemical potential the instability is d-wave dominated. The criterion we used for the distinction was the derivative of $\chi_{d-\text{wave}}$ and $\chi_s(\pi, \pi)$ when the maximal coupling grows larger than $12t$. Note however that this distinction does not allow any quantitative predictions for the true phase diagram. In contrast to the hole-doped case the strong coupling flow seems to slow down at small scales and based on our method we cannot definitely decide whether this flow really leads to a breakdown of the Landau-Fermi liquid for the given parameters. In particular the d-wave component is very weak and its

[2]This criterion has to interpreted with care because the coupling which first reach this threshold value do not necessarily belong to the channel with the strongest growth of the susceptibilities, see Fig. 7.3.

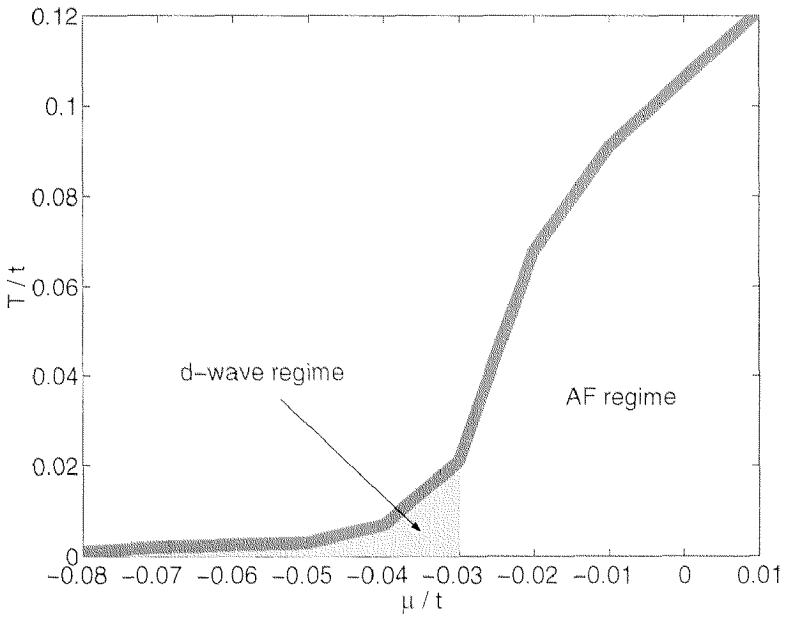

Figure 7.8: *Dependence of the strong coupling flow on μ and T in the electron-doped regime. The thick line denotes the critical temperature above which we can integrate down to $\Lambda = 0$ with all couplings staying smaller than $15t$. In the d-wave dominated regime χ_{dw} grows stronger, while in the AF regime $\chi_s(\pi, \pi)$ dominates.*

critical scale is practically zero for the chosen parameters. The qualitative and physically transparent conclusions we can draw from our analysis are the following:

- There is a competition between the imperfectly nested AF channel growing strongly at high energy scales over a large span in electron densities, and a weak $d_{x^2-y^2}$ component with a low characteristic energy scale which is generated by the weak coupling to the AF channel.
- If the AF processes flow to strong coupling the strong coupling phase is entirely determined by these and the influence of the d-wave channel on the excitations on the FS is negligible. Only if the AF processes become cut-off at lower energy scales, the d-wave processes can diverge in the particle-particle channel. Therefore this d-wave instability can be regarded as an example of Kohn-Luttinger superconductivity.
- There is no regime with a mutual reinforcement between AF and d-wave channel and the signatures of an ISL. We do not find any signs of FS truncation around the saddle points.

Therefore the flow in electron-doped case with $t' = -0.3t$ is much closer to the results of previous RG weak-coupling studies for smaller absolute values of t' [Zanchi 1997, Halboth 2000]. The flow towards an insulating spin liquid of Chapter 5 only occurs when

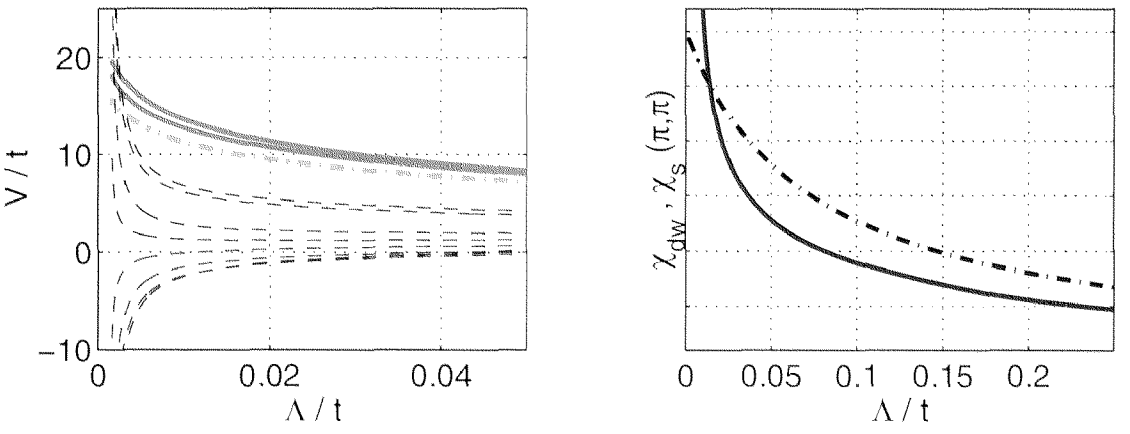

Figure 7.9: *Left: Flow of d-wave processes (dashed lines) and Umklapp processes between the BZ diagonals (solid lines) for $t' = 0$, initial $U = 2t$ and $\mu = 0.17t$. Right: Flow of d-wave pairing (solid line) and AF spin (dashed line) susceptibility for the same parameters.*

the FS is close to the saddle points *and* away from the US in the BZ diagonal. Although for smaller values of $|t'|$ and fixed band filling the coupling between d-wave and AF channel gets stronger again as the FS moves closer to the saddle points, the nesting in the BZ diagonals becomes better as well. This increases the energy scale for the strong coupling flow of the AF processes considerably such that qualitative behavior of the flow remains unchanged. In Fig. 7.9 we show data for $t' = 0$, initial $U = 2t$ and $\mu = 0.17t$ which are qualitatively similar to the electron-doped case with $t' = -0.3t$, only the scales are enhanced. Again the Umklapp processes between the BZ diagonals become large but are then cut-off at lower scales and the d-wave Cooper processes diverge, this time definitely at non-zero Λ_c.

The uniform spin and charge susceptibilities behave rather normally and are not strongly suppressed towards the instability. In particular the non-vanishing charge compressibility opens the possibility to interpret the d-wave regime found at higher electron doping as signature of a d-wave superconducting ground state. The critical scale however is very small, but a smaller absolute value t' will change this.

The question whether the wide AF dominated regime can be related to some Néel-ordered state in a layered system becomes complicated by the slowing down of the flow at low scales, where the FS curvature starts to decrease the available phase space. However in a broad range of band fillings this slowing down only occurs when the interactions have exceeded the bandwidth and self-energy and higher order corrections could change the flow at these scales. At half-filling and $t' = -0.2t$ (see next chapter) we can compare our findings to QMC results [Duffy 1996] which show an AF insulator above a critical U.

Therefore we expect the following picture for a sufficiently 3D-coupled system when we increase the filling away from half-filling: as long as the Umklapp processes in the

BZ diagonals flow to strong coupling the system exhibits AF long-range order. When these Umklapp processes become cut-off at some critical doping the ground state will be a d-wave Kohn-Luttinger superconductor. We note that there will be no FS truncation in the doping region where d-wave superconductivity dominates because all Umklapp processes are cut-off at low scales. The superfluid weight should scale with the number of electrons. All precursors of the Mott state at half-filling which are signaled by Umklapp scatterings flowing to strong coupling are hidden in the AF dominated regime. As a consequence the boundary between d-wave regime and AF regime should correspond to an ordinary quantum critical point between two different kinds of LRO.

Comparing this scenario with the experiments on electron-doped compounds we first note that the critical scale for d-wave superconductivity comes out far too small in our study with $t' = -0.3t$. There is increasing experimental evidence [Tsuei 2000, Prozorov 2000] that the superconducting state in NCCO and PBCO is indeed $d_{x^2-y^2}$ as we find unequivocally, but the superconducting T_c is only by an order of magnitude smaller than the Néel temperatures for antiferromagnetism. In our case the energy scales for both channels differ much more. As mentioned above this can be improved by choosing a smaller absolute value[3] for t' (see e.g. Fig. 7.9). Reducing $|t'|$ for better agreement with the experiment is also suggested by the particle density where the transition between d-wave and AF ground state occurs, in our case at more than 20% electron doping. The AF insulating phase in the $Nd_{2-x}Ce_xCuO_4$ extends to $x \approx 0.12$[Plakida 1995]. Still it is more robust than the AF phase on the hole-doped side. From our RG treatment it is clear that a material-dependent but non-negligible value of t'/t with the same sign can be the reason of this inequivalence between hole-doped and electron-doped cuprates.

Further there do not seem to be any experimental reports on pseudogaps in the relevant doping range, such that the scenario of a direct quantum phase transition between d-wave superconductivity and antiferromagnetism has a good chance of being correct. Also the normal state resistivity at optimal doping above the superconducting T_c seems to be more Landau-Fermi liquid-like and shows a T^2 dependence[4] above T_c [Fournier 1998, Tsuei 1989]. Due to this difference the electron-doped cuprates have been classified as intrinsically overdoped. Again from our perspective this distinct behavior of hole- and electron-doped appears to be plausible, because on the electron-doped side the van Hove points are away from the FS and no anomalous scattering processes flow to strong coupling in the d-wave regime.

[3] We took $t' = -0.3t$ for better comparison with the hole-doped side.

[4] It should be noted however that when superconductivity is suppressed by strong magnetic fields of $12T$, the resistivity becomes linear blow $10K$ [Fournier 1998].

Chapter 8

Miscellenea

Here three short sections regarding related issues. First we consider the case of a half-filled band with square Fermi surface ($t' = 0$). Then we will analyze the half-filled case with nonzero t' and compare the U-dependence of the flow with numerical results obtained by QMC. In a third section we analyze the case of large absolute value of $t' \leq -0.4t$ where we find a novel g-wave instability.

8.1 The half-filled $t' = 0$ case

The case of hopping between nearest neighbors only has been analyzed using similar methods by Zanchi and Schulz [Zanchi 1997] and Halboth and Metzner [Halboth 2000]. For the case of half-filling and $N = 16$ they found that the instability is strongly dominated by AF processes. This is also the result of our analysis on a 32×3 system. The FS with the 32 points is shown in Fig. 8.1, together with the dependence of the critical scale Λ_c on the initial interaction U. Assuming that the AF channel alone causes the flow to strong coupling, one would expect a U-dependence for Λ_c of the form

$$\Lambda_c \propto \exp\left(\frac{-1}{N_{\rm eff} U}\right) \tag{8.1}$$

with some effective density of states $N_{\rm eff}$. For small initial U however, the critical scale is small and the BZ region which is integrated out before the coupling exceed the bandwidth approaches the van Hove singularities. Therefore $N_{\rm eff}$ varies considerably for small initial values of the interactions and we find deviations from Eq. (8.1).

In Fig. 8.2 we show the main features of the strong coupling flow for $U = 2t$. The Umklapp processes between opposite sides of the US represent the strongest divergent couplings. Moreover , as one can observe from the lower plots their dependence on the position on the FS is rather weak. The interaction in the critical regions can be modeled by a sum of two repulsive contributions: a larger term which is strongly peaked

at $\vec{k}_2 - \vec{k}_3 \approx (\pi, \pi)$ and a smaller term strongly peaked at $\vec{k}_1 - \vec{k}_3 \approx (\pi, \pi)$. These two yield the vertical and horizontal line-like features in the lower plot of Fig. 8.2. Note that here the leading interaction only depends on the momentum transfer between incoming and outgoing wavevectors and not on their individual position on the FS. This behavior is assumed in various other approaches to strongly correlated systems like typical FLEX (fluctuation-exchange approximation) applications.

The flow of the d-wave processes is only weak apart from one type of processes, represented by $V_\Lambda(1, 17, 8)$ as the separately rising (as $\Lambda \to 0$) dashed line in the upper plot of Fig. 8.2. Here we have another example of the coupling between AF and d-wave processes at the saddle points: the pairing process $V_\Lambda(1, 17, 8)$ involves momentum transfer (π, π) between point 17 (k_2) and point 8 (k_3) and is therefore driven by the AF channel. However since the AF processes in the $t' = 0$ half-filled case becomes large on the whole FS, they diverge at a high critical scale already before the coupling to the pairing channel at the saddle points only can create a sizable d-wave component. Thus the d-wave channel – disadvantaged by its nodes in the BZ diagonals and zero initial component in the bare interaction – remains subdominant and cannot alter the strong coupling flow as it does in the saddle point regime of the $t' = -0.3t$ case. Moreover in a careful analysis it becomes clear that although the d-wave component is generated by the (π, π) scattering in the AF channel, it is also partially suppressed by the same class of processes: e.g. for $N = 32$ the Cooper process $V_L(4, 20, 4)$ should flow to $-\infty$, but due to its momentum transfer $\vec{k}_3 - \vec{k}_2 \approx (\pi, \pi)$ it is initially enhanced through the AF channel and does not reach negative values before the flow leaves the perturbative region.

We note that according to the numerical data the behavior described above appears to hold for arbitrarily small U. Below $U = 0.3t$ the critical scale becomes smaller than $0.0001t$, but even for $U = 0.1t$ the nesting features are discernible and have the structure described above. Therefore for the half-filled Hubbard model with $t' = 0$ our results are consistent with a AF ordered ground state for all U and rule out a d-wave superconducting ground state. This is in contrast with the half-filled $t' \neq 0$ case which will be described next.

8.2 The half-filled $t' \neq 0$ case: curvature versus critical scale

Next we analyze the case of a half-filled band and $t' = -0.2t$. Here we focus on the dependence of the flow to strong coupling on the strength of the initial interaction U. From the RG point of view this case of a weakly curved FS is interesting because we expect a curvature-dominated regime at small U, where the nesting between opposite FS sides is cut-off, and a approximate nesting regime at larger U with a strong coupling

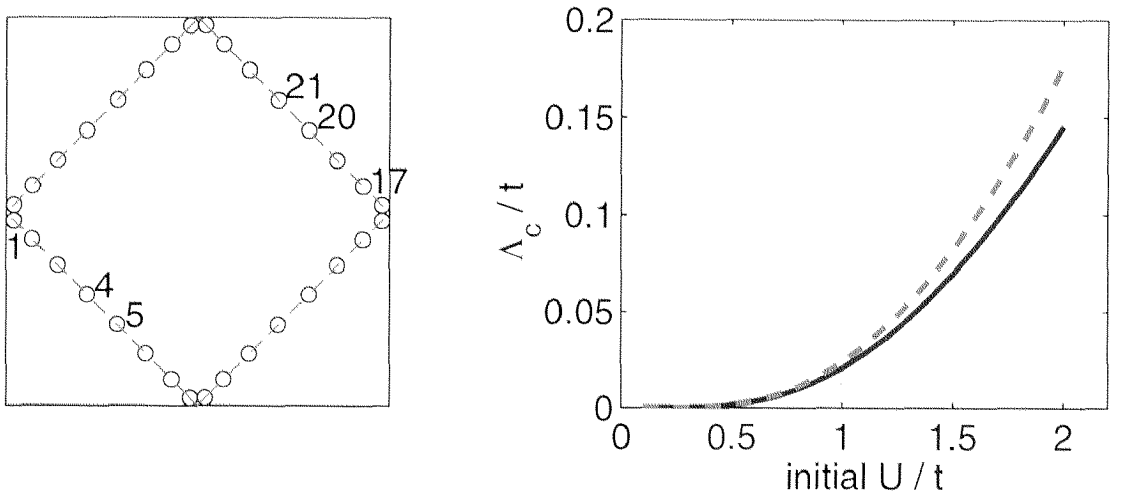

Figure 8.1: *Left: The Fermi surface at $t' = 0, \mu = 0$ (filled dots, equivalent to the Umklapp surface, dashed line) and the 32 points on the FS used in the RG calculation. Right: Critical scale Λ_c for the flow to strong coupling vs. strength of the initial interaction U. The dashed (solid) line denotes the scale, where the largest couplings reach $15t$ ($30t$).*

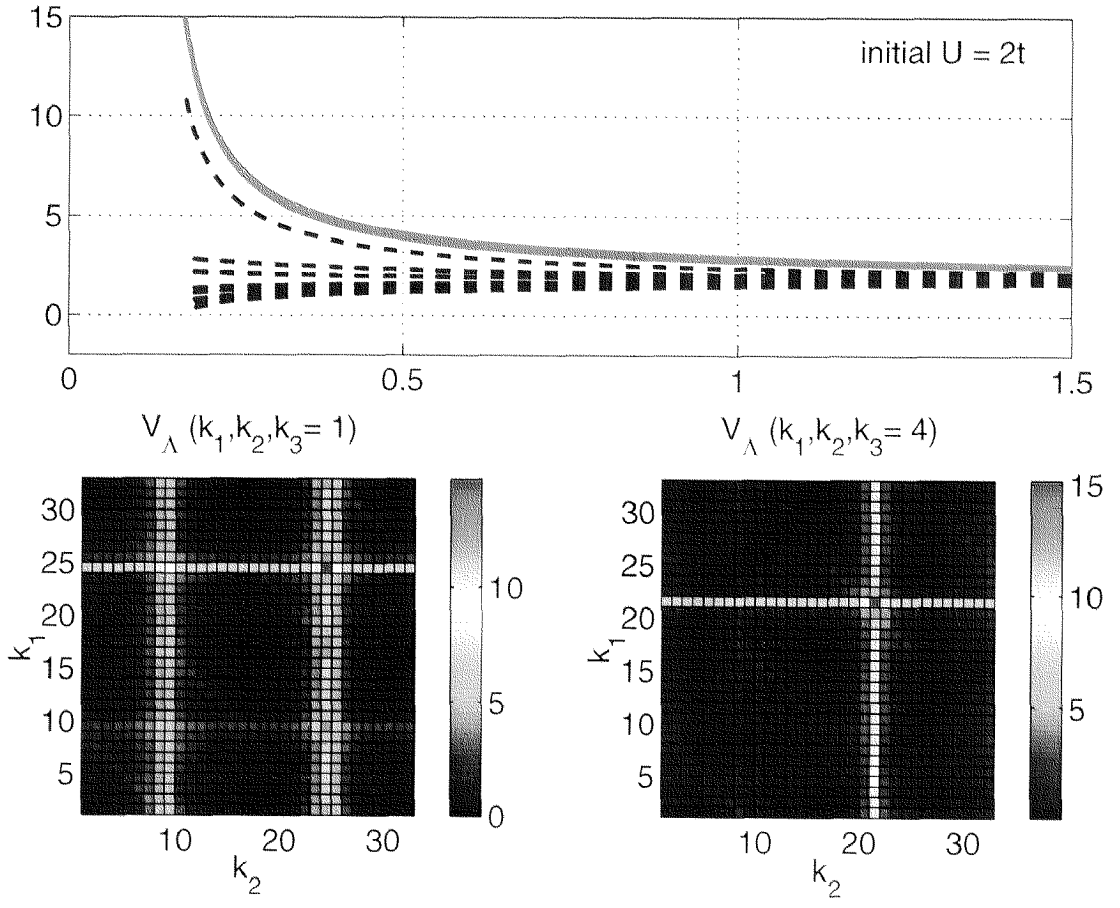

Figure 8.2: *Strong coupling flow for $t' = 0, \mu = 0$: the upper plot shows the flow of Umklapp processes between the BZ diagonals ($V_\Lambda(21, 21, 4)$ and $V_\Lambda(21, 21, 4)$ (solid lines) and the d-wave pairing processes (dashed lines). Lower plots: snapshots of the k_1-k_2 dependence with first outgoing wave-vector fixed at point 1 (left) and 4 (right plot). The 32 point are numbered counterclockwise around the FS (see Fig. 8.1).*

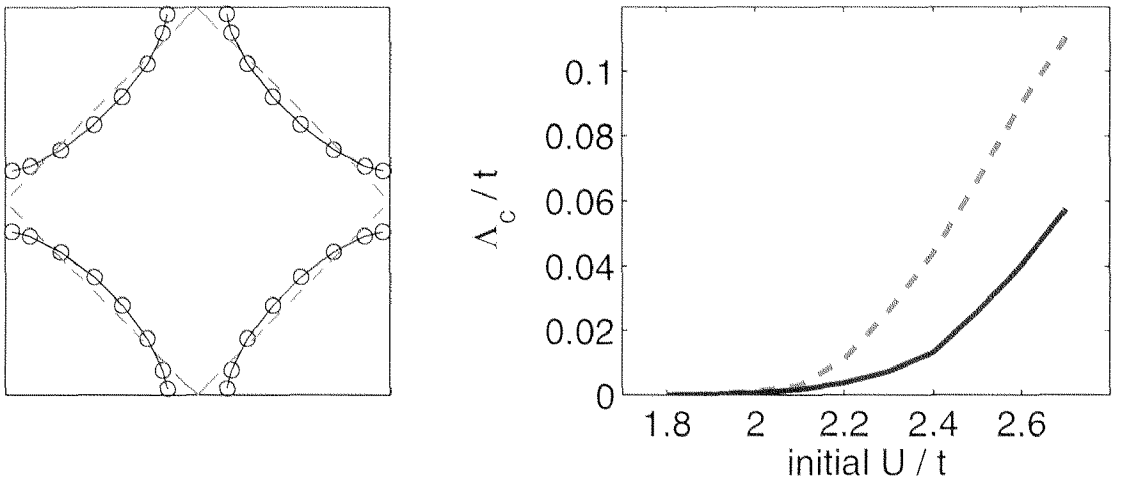

Figure 8.3: *Left: The Fermi surface for $t' = -0.2t$ and $\mu = -0.48t$ (half-filling). The circles show the 32 points used in the N-patch RG calculation. Right: Critical scale for the flow to strong coupling at half-filling and $t' = -0.2t$ versus strength of the initial interaction U. The dashed line denotes the scale, where the largest couplings reach $15t$. At the scale corresponding to the solid line the largest couplings exceed $30t$.*

flow dominated by antiferromagnetic processes involving momentum transfer (π, π)[1]. This has been described by Zheleznyak et al [Zheleznyak 1997] using a parquet approach for a simplified model. Furthermore there exist mean-field studies [Duffy 1996, Hofstetter 1998] and finite-size quantum Montecarlo results [Duffy 1996] for the t-t' Hubbard model with the same parameters such that we can compare the RG flow with these. The mean-field studies give a critical $U_c = 2t$ required for stabilization of an antiferromagnetically ordered ground state, while the quantum Montecarlo on 8×8 clusters T down to $t/8$ showed long-range tails in the staggered spin-spin correlation for $U_c = 2.5 \pm 0.5t$.

In Fig. 8.3 we plot the FS with $N = 32$ points used in the RG calculation and the critical scale of the flow to strong coupling versus strength of the initial interaction. Below $U \approx 2t$, the critical scale is very small, $\Lambda_c \leq 0.002t$. In Fig. 8.4 we show the RG flow of d-wave and AF processes at $T = 0.001t$. It can be clearly observed how the AF Umklapp processes between the BZ diagonals get cut-off at lower scale if the initial coupling is smaller than $U_c^{AF} \approx 2.4t$. Note however that for $U \geq 1.8t$ they still become larger than the bandwidth, so that the validity of our scheme is not guaranteed. For $U \geq 2.4t$ the growth of the Umklapp processes does not show signs of deceleration at lower scales, such that the instability is dominated by the AF processes. This can also seen from Fig. 8.5, where we plot the flow of AF and d-wave susceptibilities. For initial $U \geq 2.4t$, χ_{dw} overtakes $\chi_s(\pi, \pi)$ only when the interactions have flown far out of the perturbative

[1] For simplicity we do not analyze any tendencies towards formation of incommensurate spin density waves.

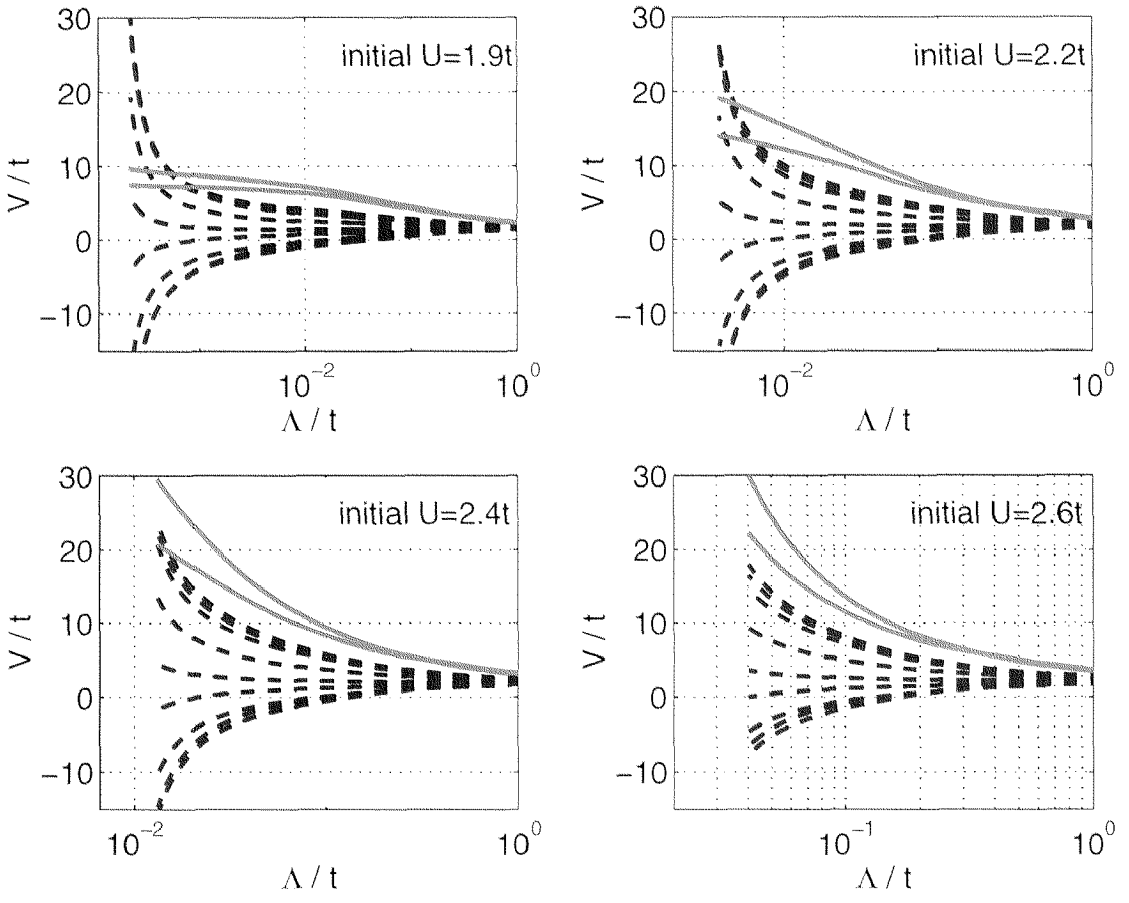

Figure 8.4: *Strong coupling flow at $t' = -0.2t$, $T = 0.001t$ and $\mu = -0.48t$ (half-filling) for different initial interaction U. The solid lines denote Umklapp processes between the BZ diagonals, the dashed lines show d-wave pairing processes.*

region ($\approx 30t$). Again the RG does not allow to determine sharp boundaries, but for $U \geq 2.4t$ our results are consistent with an AF ordered ground state, as suggested by the mean-field and QMC studies mentioned above.

The RG flow for U-values smaller than $2.4t$ is dominated by a strong growth in the d-wave channel at low scales, which can be regarded as a realization of a Kohn-Luttinger instability. The Cooper channel is not cut off, and supports the flow of an initially small d-wave component in the pair scattering generated at higher energy scales by the repulsive (π, π) processes. For increasing U the magnitude of this d-wave component becomes larger as the AF processes get stronger. This in turn enhances the critical scale for a d-wave dominated instability. At $U = 2.2t$ the critical scale is $\approx 0.005t$.

We finish this subsection with the conclusion that with our RG treatment we find qualitative agreement with mean-field and QMC studies that a AF ordered ground state should exist for values of $U \geq 2.4t$. For smaller values of the initial interaction the strong

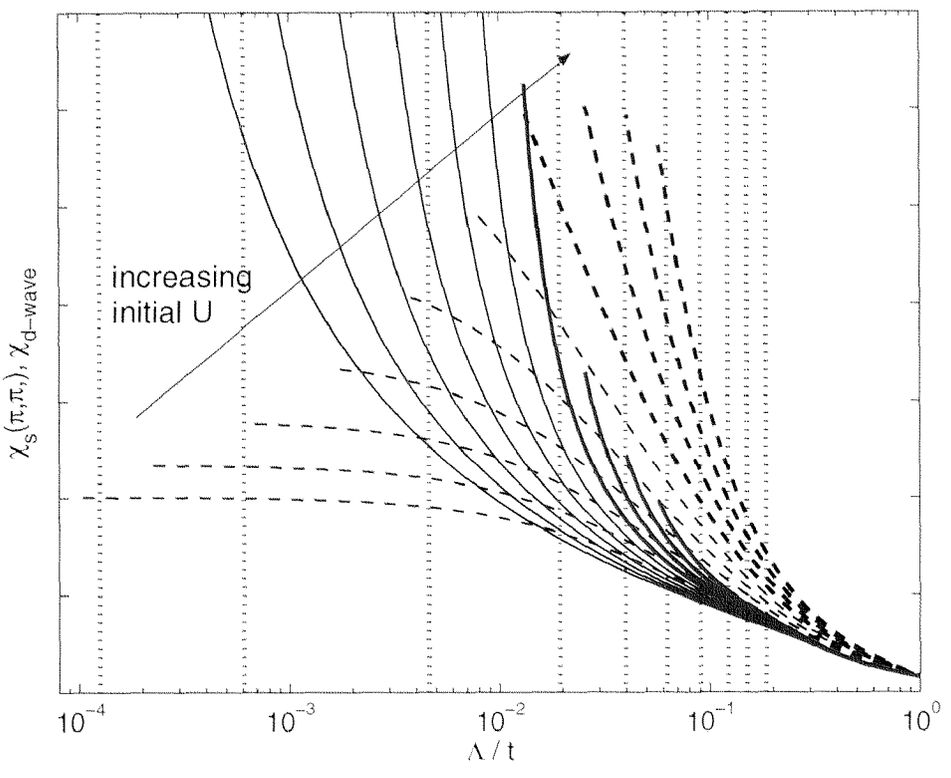

Figure 8.5: *Flow of $d_{x^2-y^2}$ (solid line) and AF (dashed line) susceptibility at $t' = -0.2t$, $T = 0$ and $\mu = -0.48t$ (half-filling) for different initial interaction U ranging from $U = 1.8t$ (smallest critical scale/lowest curves) to $U = 2.7t$ in steps of $0.1t$. The curves for $U \geq 2.4t$ have thicker lines. The vertical lines denote the scales where the largest couplings reach $10t$.*

coupling flow is dominated by the $d_{x^2-y^2}$-pairing channel at however rather low critical scales. Nonetheless it would be interesting to compare mean-field ground state energies for AF order and $d_{x^2-y^2}$-pairing (with an appropriate ansatz for the pair scattering, e.g. from the RG) in this parameter region.

8.3 Surprises at $t' < -0.4t$: the g-wave instability

So far the symmetry of the pair scattering in the flow of to strong coupling was always $d_{x^2-y^2}$. In this section we will give an example that there is also a parameter range where a g-wave instability occurs with a $\cos 4\theta$-variation of the pair scattering around the FS. It should be noted that according to the classification into irreducible representations of the tetragonal symmetry group this type of pair scattering transforms like the trivial s-wave representation because all symmetry operations of the square lattice leave $\cos 4\theta$ invariant. Nevertheless since it arises from approximate nesting between FS parts connected by incommensurate wavevectors which splits the extrema of the d-wave angular dependence $\cos 2\theta$, it appears to be more natural to use the term g-wave rather than extended s-wave.

8.3.1 Occurrence and origin of the g-wave component

Let us consider the van Hove filling where the FS contains the $(0,\pi)$ and $(\pi,0)$ points and vary the value of the next-nearest neighbor hopping t'. In Fig. 8.6 we plot the pair scattering $V_\Lambda(\vec{k},-\vec{k},\vec{k}')$ for different positions $\vec{k}$ of the incoming pair as function of the outgoing pair $\vec{k}'$. For values $t' \leq -0.36t$ the pair scattering has a typical $d_{x^2-y^2}$-form with 2 maxima and 2 minima for $\vec{k}'$ moving around the FS. This changes when we increase the absolute value of t': the pair scattering develops small dips at the angles corresponding to the extrema for the pure d-wave case. Each maximum and minimum splits up in two extrema. The separation between the split peaks grows with further increase of $|t'|$, and for $t' \leq -0.4t$ the pair scattering is better described by a $\cos 4\theta$ variation, which corresponds to g-wave. In Fig. 8.7 we compare the flow of d-wave and g-wave susceptibilities which clearly shows the change in the pairing symmetry for $t' \leq -0.4t$.

For this type of g-wave pair scattering the most repulsive part of the scattering is between pairs in the BZ diagonal and pairs in the saddle point regions. The reason why such a pair scattering occurs becomes clear in an analysis of the bare particle-hole bubble $\chi_{\rm PH}(\vec{q})$ as function of the wavevector flowing through it, shown in Fig. 8.9. For $|t'| = 0$, $\chi_{\rm PH}(\vec{q})$ is peaked around (π,π) and when the FS is inside the US the most repulsive pair-scattering arises for processes exchanging pairs between the saddle points. There is also a peak at $\vec{q} = 0$ arising from the diverging density of states, its role is discussed in a following subsection. When we increase $|t'|$ the (π,π)-peak in $\chi_{\rm PH}(\vec{q})$ moves away

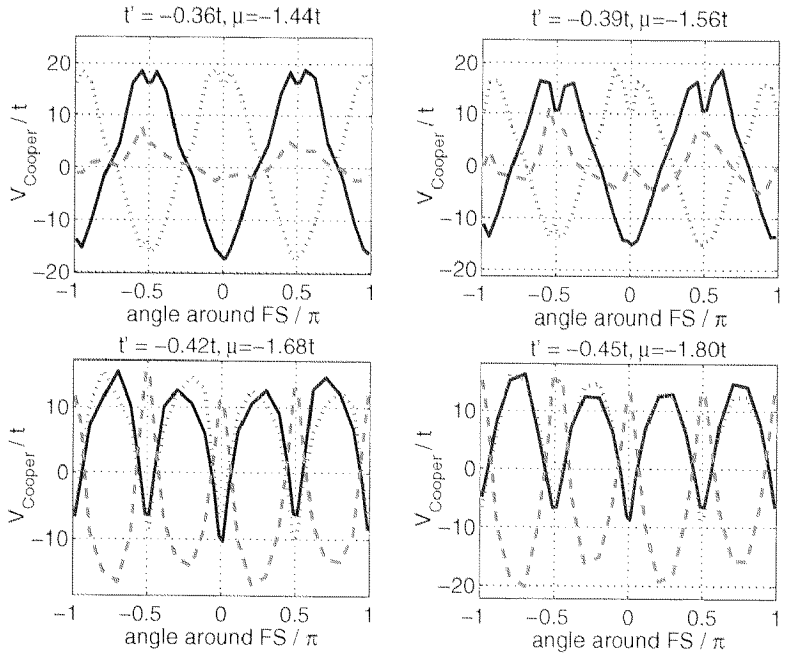

Figure 8.6: *Pair scattering $V_\Lambda(\vec{k}, -\vec{k}, \vec{k}')$ versus the angle of $\vec{k}'$ around the FS for different values of t'. The solid line ($\vec{k}$ at point 1 for $N = 32$) and the dotted line (point 8 for $N = 32$) denote the processes with $\vec{k}$ fixed at inequivalent saddle points. For the dashed line $\vec{k}$ is located in the BZ diagonal (point 4).*

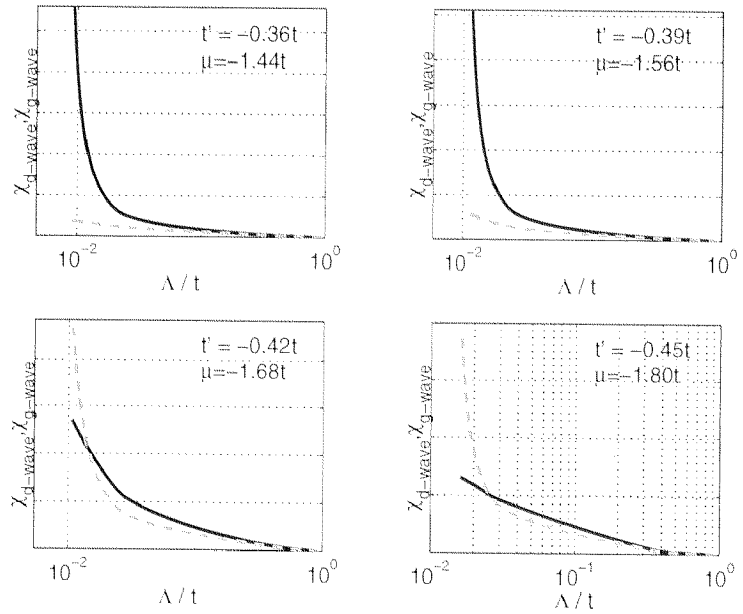

Figure 8.7: *Flow of d-wave (solid line) and g-wave (dashed line) susceptibilities for different values of t' at van Hove filling and $T = 0.005t$.*

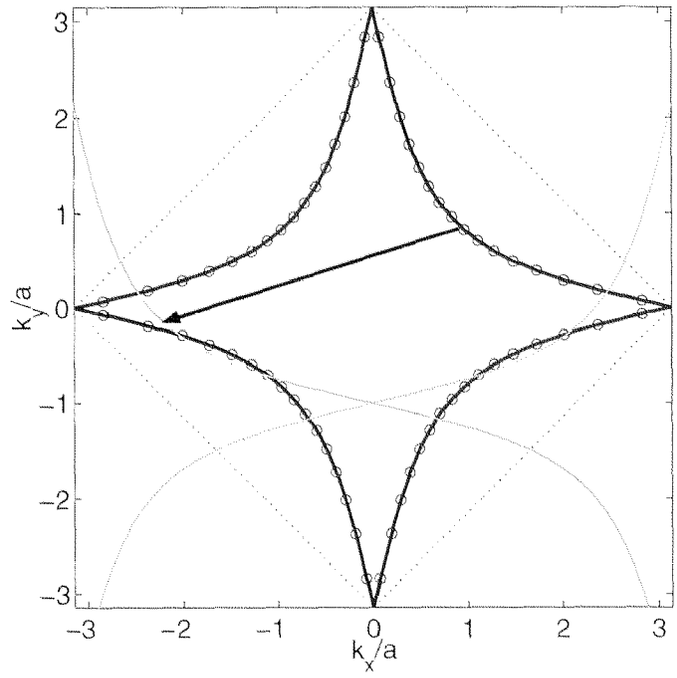

Figure 8.8: *Fermi surface (thick line) and its translate (thin line) by the approximate nesting vector* $\vec{q}_p = (\pi, 1)$ *for* $t' = -0.45t$ *and* $\mu = -1.8t$.

to $(\pi - \delta, \pi)$ and $(\pi, \pi - \delta)$. For $t' = -0.45t$ due to the absence of strong nesting the $\vec{q}$-dependence of $\chi_{\rm PH}(\vec{q})$ is not too pronounced, yet it is peaked around $\vec{q}_p \approx (\pi, 1)$ and $(1, \pi)$. These wavevectors connect the FS parts in the BZ diagonals with the flat low energy regions closer to the saddle points (see Fig. 8.8), and the scattering processes $V_{\rm A}(\vec{k}_1, \vec{k}_2, \vec{k}_3)$ with momentum transfer $\vec{k}_1 - \vec{k}_3 \approx \vec{q}_p$ between these regions will be enhanced by the crossed particle-hole diagram. As described in Eq. (1.6) in Chapter 1 this generates an anisotropy in the Cooper pair scattering as well because among the processes between the BZ diagonals and the saddle points which are increased there are also pair scattering processes with $\vec{k}_2 = -\vec{k}_1$, while all other Cooper processes will be initially suppressed through the particle-particle channel. Thus, since there are four BZ diagonals and four saddle point regions as function of the angle around the FS, the pair scattering obtains a four-fold symmetry, the g-wave component. Since the nesting between the FS regions connected by $\vec{q}_p$ is imperfect the most normal processes involving this momentum transfer do not diverge when we decrease the scale and saturate at some value. This is different of course for the g-wave Cooper processes which are not cut-off and diverge a finite critical scale. As can be seen from Fig. 8.7 the critical scale does not vary much when we change t'.

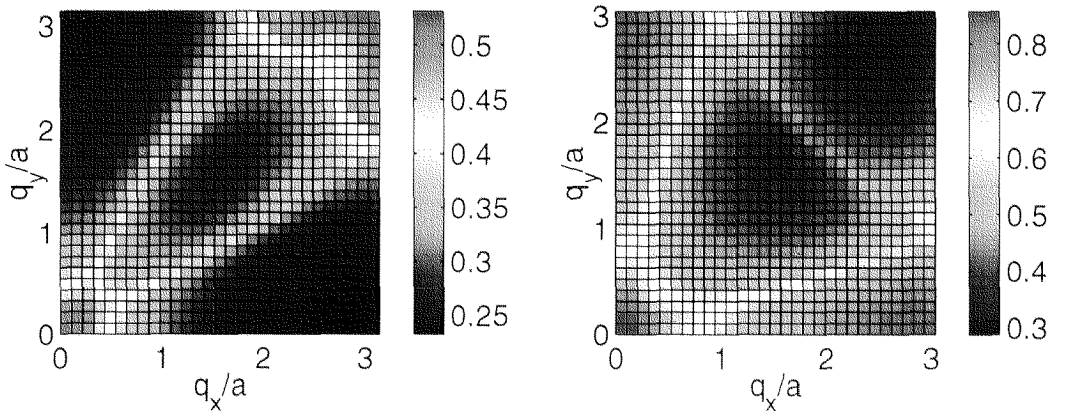

Figure 8.9: *Particle-hole bubble* $|\chi_{\rm PH}(\vec{q})|$ *at* $T = 0.005t$ *for* $t' = -0.3t$ *(left plot) and* $t' = -0.45t$ *(right plot). The band filling in both cases is the van Hove filling with* $\mu = 4t'$.

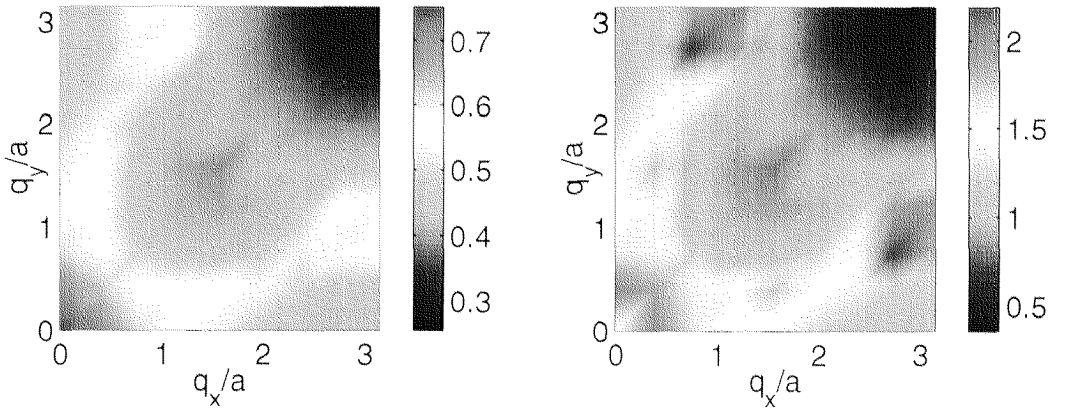

Figure 8.10: *Left:* $\vec{q}$*-dependence of the bare spin susceptibility* $\chi_s^0(\vec{q}) = \chi_{\rm PH}(\vec{q})$. *Right:* $\vec{q}$*-dependence of the interacting spin susceptibility* $\chi_s(\vec{q})$ *calculated with the RG scheme. For both cases we used a* $N = 32$*-system at* $t' = -0.45t$, $\mu = -1.8t$ *and* $T = 0.015t$. *For these parameters, the flow of the couplings stays in the range* $[-1.15t\ 3.75t]$.

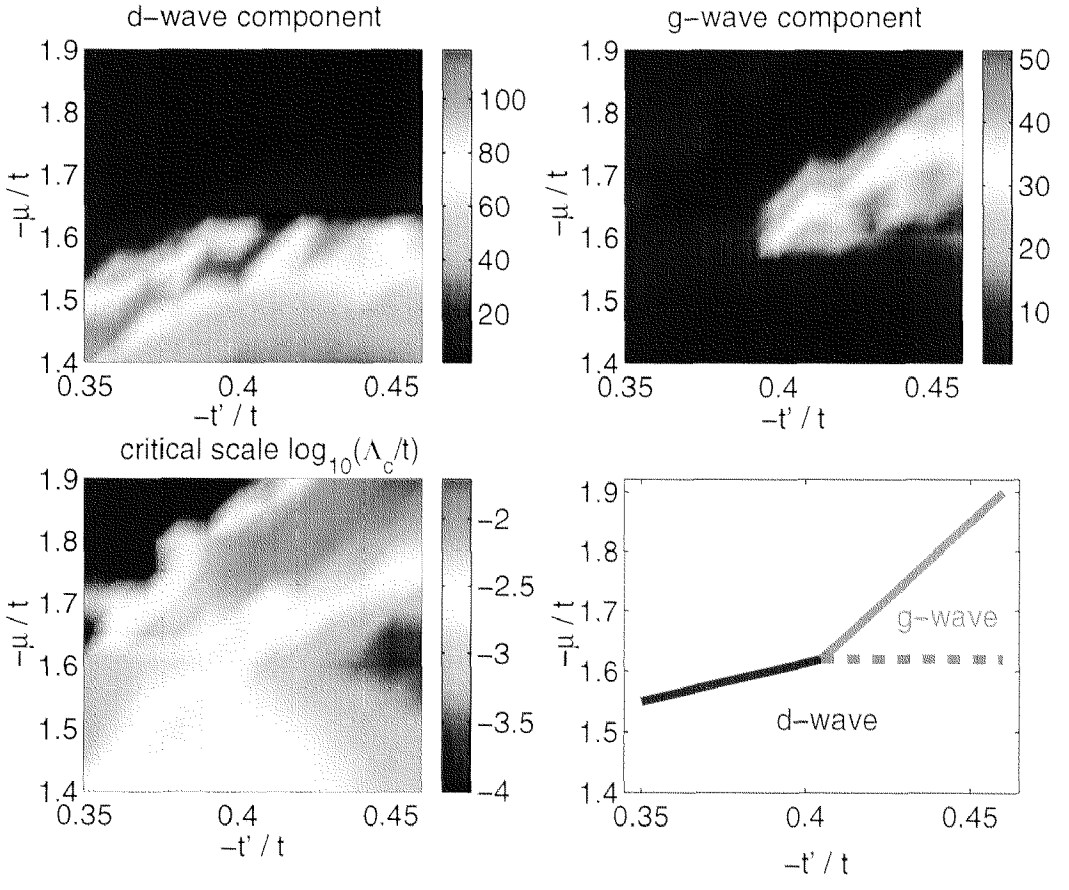

Figure 8.11: *Upper plots:* $\cos(2\theta)$ *(d-wave) and* $\cos(4\theta)$ *(g-wave) components in the pair scattering for different values of* t' *and* μ*. Lower plots: Critical scale where the largest coupling reach* $20t$ *vs.* t' *and* μ *(left plot) and schematic phase diagram (right plot).*

8.3.2 The parameter region for the g-wave instability

Keeping the FS fixed at the van Hove points, the g-wave dominated instability occurs for $t' < -0.4t$ (see Figs. 8.6 and 8.7).

For larger band filling, $\mu \geq -1.6t$, the $d_{x^2-y^2}$ component prevails. In Fig. 8.11 we show the $\cos(2\theta)$ (d-wave) and $\cos(4\theta)$ (g-wave) components in the pair scattering for a broader range of chemical potentials and values for t', calculated for a $N = 64$ system with initial $U = 2.5t$. The lower plot shows the dependence of the critical scale Λ_c on these parameters. In the lower right plot of Fig. 8.11 we summarize these data in a schematic $T = 0$ phase diagram. We mark three distinct regions: a $d_{x^2-y^2}$ regime, the novel g-wave regime and another region where no divergent pairing correlations develop down to very low scale ($\Lambda \sim 10^{-1}t$). There we still find a flow to strong coupling for fillings closer to the van Hove filling, mainly due to approximate nesting between flat FS parts.

For $t' = -0.45t$ and van Hove filling the g-wave instability starts to develop at critical scales $\Lambda_c \geq 0.001t$ for initial interaction strength $U \geq 2t$. The tentative phase diagram in Fig. 8.11 does not strongly depend on the value of the initial interaction. Further we checked the results on several 32×3 systems with minimal amount of radial resolution for the couplings different parameters.

8.3.3 Ferromagnetism and p-wave superconductivity

Flat bands close to the Fermi surface can lead to ferromagnetism (for reviews, see e.g. [Tasaki 1998, Vollhardt 1999]). Therefore several methods have been applied to analyze the stability of ferromagnetism for the two-dimensional Hubbard model with large $|t'/t|$. By projection Montecarlo with Gutzwiller trial wavefunctions Hlubina et al. [Hlubina 1997] found a stable ferromagnetic phase for $t' = -0.47t$ and $U = 4t$, in consistency with T-matrix approximation calculations. In contrast with that using our RG scheme we find again a g-wave instability for the same t'/t-ratio and $U = 2.5t$. Since this involves the formation of singlet Cooper pairs, the uniform spin susceptibility $\chi_s(0)$ becomes increasingly suppressed towards lower scales, just like in the $t' = -0.3t$ case with the d-wave pairing tendencies.

In RPA the uniform spin susceptibility diverges at the van Hove filling because of the logarithmic singularity in the density of states. Again the divergence in the Cooper channel is stronger ($\log^2$) as the particle-particle bubbles in the ladder sum provide an additional small energy denominator. On the other hand the g-wave component in the pair scattering is only generated during the flow through one-loop particle-hole corrections to the pair scattering. If we further increase the ratio $|t'/t|$ towards $\frac{1}{2}$ (the flat band limit) with the FS fixed at the van Hove points the particle-hole phase space gets considerably reduced because the Fermi surface moves towards the bottom of the band. This in turn weakens the initial condition for the g-wave component in the pair scattering

($V_l \to 0$), and it has less scale range to develop in the Cooper channel ($\omega_D \to 0$). Thus there may be a critical $|t'/t|$ where the potential energy gain through the Kohn-Luttinger instability becomes less than the energy gain through ferromagnetism which does not require any phase space for particle-hole excitations. The parameter region very close to $t' = -0.5t$ with the sharply peaked FS is however not accessible for the N-patch scheme in its present form.

Next we comment on the possibility of a p-wave Kohn-Luttinger instability. At zero temperature the van Hover singularities cause a divergence of $\chi_{\rm PH}(\vec{q})$ at $\vec{q} = 0$. According to the Kohn-Luttinger analysis of the second order particle-hole corrections to the pair scattering in Chapter 1 this should lead to a large p-wave component in the pair scattering. In particular at low temperatures the p-wave component generated by particle-hole processes should exceed possible g-wave components generated by non-divergent approximate nesting as $\chi_{\rm PH}(\vec{q} = 0)$ is not bounded for $T \to 0$. Indeed the explicit Kohn-Luttinger calculation for small U [Hlubina 1999] yields a p-wave instability e.g. for the saddle-point filling with $t' = -0.45t$.

In principle RG represents a more powerful method for detecting weak-coupling instabilities than the analysis of the second order particle-hole diagram. Nonetheless one difficulty in comparing p- and g-wave components in the pair scattering with RG arises from the fact that the peak of $\chi_{\rm PH}(\vec{q})$ at $\vec{q} = 0$ which causes the attractive p-wave component only contributes to the RG flow at scales $\Lambda \approx T$ as it occurs due to the diverging density of states at the FS. In contrast with that the approximate nesting contributions generating the g-wave part start to be included in the RG flow at scales $\Lambda > T$ already. Thus we have to resort to temperatures above the critical temperature for the flow to strong coupling. Then we can integrate out all modes and get the $\vec{q} = 0$ contributions as well. Doing this we still find a predominant g-wave component, while the p-wave component remains repulsive.

These observations suggest that in the case of a large $|t'| < 0.47t$ the particle-particle bubble and the other three non-crossed particle-hole diagrams (see Fig. 3.2) which for the Hubbard interaction cancel in second order and are therefore absent in the conventional Kohn-Luttinger analysis change the effective pair scattering considerably through higher order diagrams generated by the RG scheme. They enhance the g-wave component through approximate nesting and suppress the p-wave tendencies. Indications for this come from comparing the bare spin susceptibility $\chi_s^0(\vec{q}) = \chi_{\rm PH}(\vec{q})$ with the interacting susceptibility $\chi_s(\vec{q})$ calculated with the N-patch RG scheme by integrating out all modes at temperature $T = 0.015t$ and initial $U = 1.8t$ where the flow does not diverge. This is shown in Fig. 8.10: while the bare spin susceptibility (left plot) is peaked at $\vec{q} = 0$, the RG susceptibility in the right plot has its maxima at $\vec{q} \approx (3, 1)$ (the $\vec{q}$-space resolution in this calculation is only $\pm 0.2/a$) and symmetry-related points.

These issues have to be analyzed further. Increasing $|t'|$ towards $t/2$ will enhance $\chi_{\rm PH}(\vec{q} = 0)$ with respect to the approximate nesting features such that the p-wave tendencies might become strengthened this way. It might also be that for smaller initial

interaction the approximate nesting gets reduced such that the p-wave component dominates at low scales. Finally the N-patch scheme has to be improved in order to obtain more resolution for the sharply peaked FS at the saddle points such that we can better exclude errors by the patch discretization of the four-point vertex[2] and can approach the limiting case $t' = -0.5t$ closer.

[2] Although calculations with 32×3 systems with minimal amount of radial resolution do not give qualitative differences.

Chapter 9

Instabilities at 110 Surfaces of $d_{x^2-y^2}$ Superconductors

The results in this chapter were obtained in collaboration with M.Sigrist. The main part of what follows was published in [HS 2000].

9.1 Introduction

A large number of experiments have established that the Cooper pair wavefunction has $d_{x^2-y^2}$-wave symmetry in high-temperature superconductors. Decisive information came from probes which are sensitive to the internal phase structure of the pair wavefunction. Besides experiments based on the Josephson effect [van Harlingen 1995] also the surface Andreev bound states (ABS) [Hu 1995] observable in quasiparticle tunneling can be counted among the strongest experimental tests of this type. For a superconductor with pure $d_{x^2-y^2}$ symmetry these ABS should be most pronounced at [110] surfaces and lie exactly at the Fermi energy (zero energy). They lead to a rather sharp zero-bias anomaly in the I-V tunneling characteristics which reflects the surface quasiparticle density of states (DOS) [Greene 1997]. In addition low temperature anomalies in the penetration depth have been interpreted as evidence for the existence of the zero-energy ABS [Walter 1998]. An interesting twist in the view of the ABS occurred when Covington et al. [Covington 1997] observed the spontaneous split of the single zero-energy peak (ZEP) into two peaks at finite voltage equivalent to an energy of approximately 10% of the superconducting gap below $T = 7K$. Fogelström et al. [Fogelström 1997] interpreted this in terms of a time-reversal symmetry breaking (TRSB) by the admixture of a sub-dominant s-wave component close to the surface. The split ABS is the result of the opening of a small gap in the quasiparticle spectrum at the surface and can be interpreted as a Fermi surface (FS) instability. [Sigrist 1998, Fogelström 1998] TRSB is not the only way to shift the ZEP to finite energies. Many local FS instabilities could

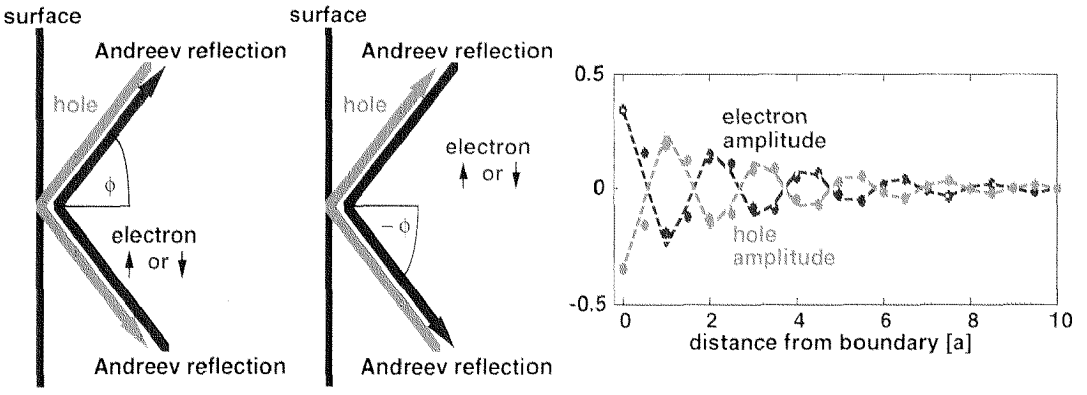

Figure 9.1: *Left: the four degenerate bound states for a given angle ϕ of the trajectory. Right: electron and hole amplitudes of the bound state wave function.*

yield the same effect and the one with the largest energy gain, i.e. the highest critical temperature, would finally govern the surface state. If we think in terms of trajectories of quasiparticles involved in the ABS at an ideal (specularly reflecting) [110] surface (see Fig. 9.1), there is a simple classification of the ways the degeneracy can be lifted. In the pure d-wave state, bound states with electrons and holes moving on the same trajectory at the surface are degenerate and they have two possible spin orientations. Hence we can either lift the charge (or directional) or the spin degeneracy. Both will lead to a TRSB surface state.

In this chapter we discuss the instability due to correlation effects among the quasiparticles. The zero-energy ABS consists of degenerate states with a charge current running parallel to the surface (in-plane) in both directions (the *directional degeneracy*) and with both spin up and down (the *spin degeneracy*). The TRSB state lifts the directional degeneracy of charge currents by admixing a subdominant s-wave component to the d-wave pairing state and a spontaneous finite current appears. [Sigrist 1998] On the other hand, the spin degeneracy can be lifted yielding a spin density wave-like state at the surface, although magnetic ordering is absent in the bulk. [Wakabayashi 1996] This instability is driven by the repulsive electron-electron interaction responsible for the strong antiferromagnetic spin fluctuations in the underdoped region of high-temperature superconductors. From this point of view the magnetic instability represents an equally probable way to lift the degeneracy of the zero-energy states.

In the following we analyze the properties of [110]-oriented surface of the $d_{x^2-y^2}$-wave superconductor on a square lattice forming a strip of finite width (infinitely long along [1,-1,0]-direction) such that we have two surfaces. The translationally invariant direction is denoted by the y-axis and the surface normal direction by the x-axis (Fig.1). We describe this system by a tight-binding model with nearest (t) and next-nearest (t') neighbor hopping, and include an onsite repulsive and a spin-dependent nearest neighbor

troduces

(9.1)

$n(\mathbf{x}) =$
on near-
pairing.
action in
g mean-
ons, two
$S_z = 0$)
) state as
l we ob-
unctions
pendent
and the
r the so-
nagnetic
typical
here the
$= -0.3t$
FS). The
d region

s and

xamined
channel,
long the
ctor po-
lirection
decays
energy
e energy
eads to a
state the

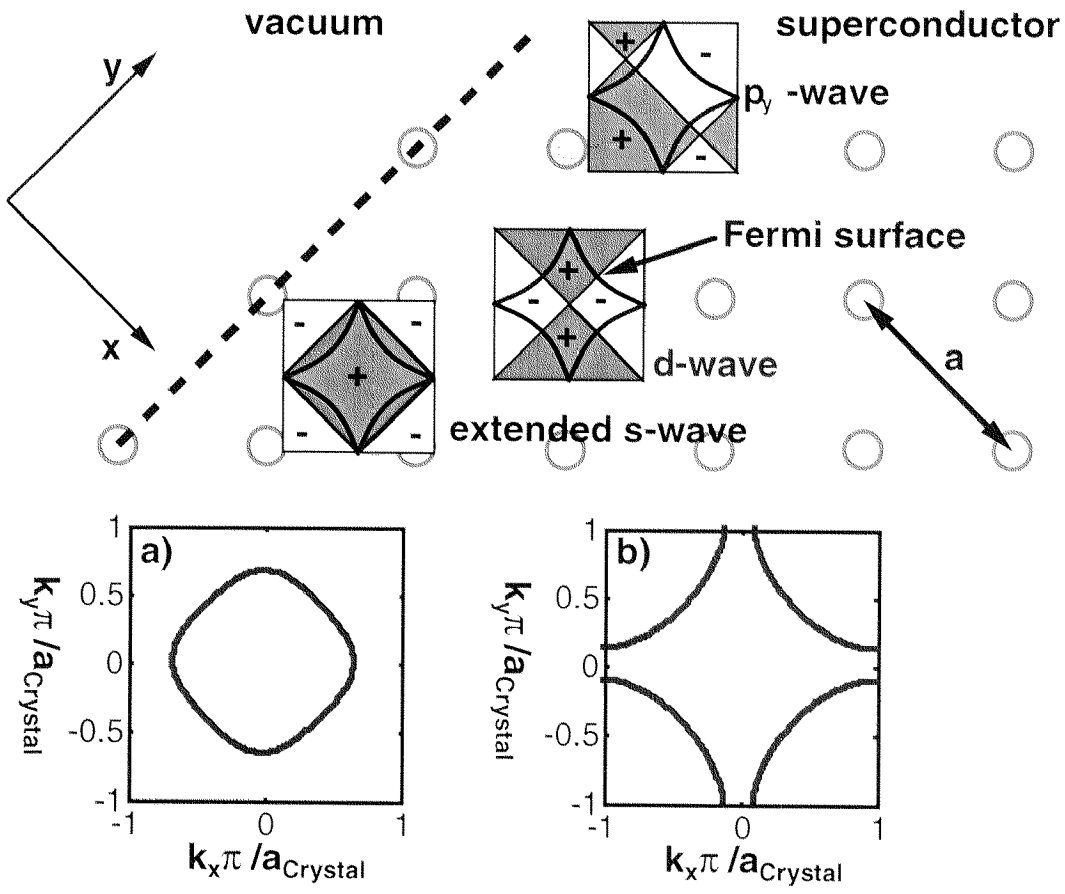

Figure 9.2: *Geometry and coordinate system of the [110] boundary. The symmetries of the relevant gap functions are symbolized by the + and − regions in the Brillouin zones. a) Fermi surface for the* regular FS *parameters given in the text. b) Fermi surface for* singular FS *parameters. In our notation* $a = \sqrt{2}a_{Crystal}$

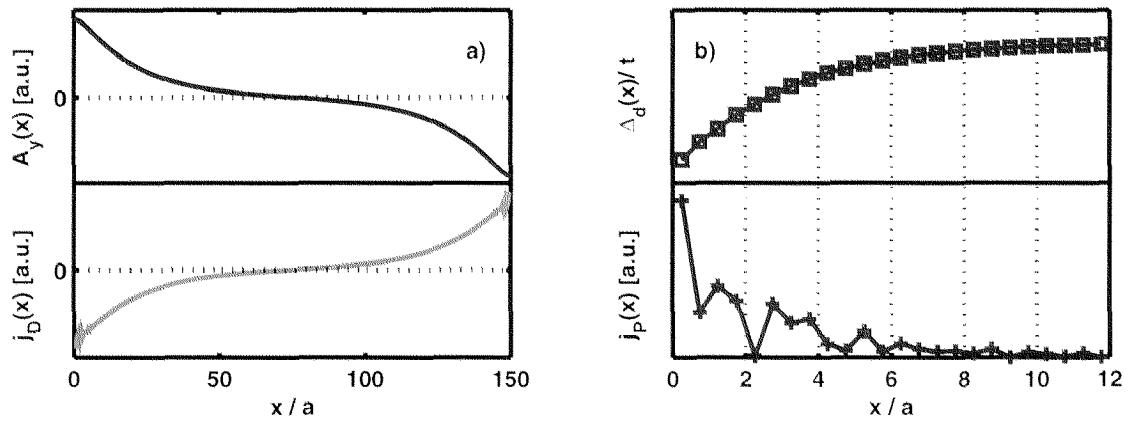

Figure 9.3: *Spontaneous surface current state: a): Vector potential A_y and diamagnetic Meissner current density j_D. b): d-wave gap function Δ_d and the paramagnetic surface current density j_P carried by the Andreev bound states (system width $150a$, $\mu = -t$, $t' = 0$, $\lambda \approx 18a$ and $T = 0.001t$ yielding critical temperatures $T_c^{SSC} = 0.006t$ and $T_c^d = 0.11t$).*

spontaneous surface current (SSC) state. The spatial dependence of the vector potential $A_y(x)$, diamagnetic and paramagnetic current densities and the d-wave gap function are shown in Fig.9.3. From quasi-classical calculations [Higashitani 1997, HS 1997] one expects a critical temperature T_c^{SSC} of the order $(\xi/\lambda)T_c^d$, i.e. rather small for a typical high-T_c superconductor. Our numerical results show $T_c^{SSC} = 0.006t$ or $T_c^{SSC}/T_c^d \approx \frac{1}{2}\xi/\lambda$. This low transition temperature indicates that the split of the ABS levels is rather small and barely visible in the surface DOS. We conclude that this surface instability is a poor candidate in order to explain the experimental observations.

Now we include a finite s-wave component with a relative phase of $\pm\pi/2$ with respect to the d-wave gap ($s \pm id$). This phase is chosen to maximize the condensation energy of the surface state. Since this TRSB s-wave admixture also lifts the charge degeneracy by changing the Andreev reflection properties for the states with left and right going charge currents, it leads naturally to a net surface current. In the presence of a finite attractive s-wave coupling this will lead to an additional contribution in the gap function increasing the energy gain and resulting in a wider splitting of the ZEP. As a consequence the critical temperature for this $s + id$ state is higher than for the SSC state without s-component. Spatial and temperature dependence of s-admixture and vector potential are shown in Fig.9.4. For our choice of parameters, the split in the surface DOS has similar size relative to the bulk gap value as in the experiment.

The onsite Coulomb repulsion U itself does not suppress the extended s-wave admixture induced at the boundary, but it can generate a finite magnetization $m(\mathrm{x})$ which then competes with this superconducting state. If we look for a surface state with finite magnetization for the *regular FS*, we find indeed that already for $U = t$ its critical tem-

perature is comparable to that of the $s+id$-wave state. For the *regular FS* parameters the weak spin polarization (less than 3%) is ferrimagnetic and decays into the bulk on the scale of the superconducting coherence length. It is accompanied by a TRSB spin-triplet p-wave admixture. The p_y-wave component is induced directly by the d-wave state because the spin rotational symmetry is broken such that the total spin of the pair is not a good quantum number anymore. The p_x-wave component does not appear, since it is odd with respect to specular reflection at the surface and is suppressed by pair breaking. Note that neither the magnetization nor the p-wave admixture lift the directional degeneracy. Therefore the magnetic surface state does not generate charge or spin surface currents. The split in the surface DOS by the magnetic state is shown in Fig.9.4. As a consequence of the lifted spin degeneracy of the ABS the surface DOS is different for spin-up (with respect to the magnetization axis) and spin-down electrons, a property which could be tested by spin-polarized quasiparticle tunneling.

In Fig.9.6 we show the U-dependence of the critical temperatures for the two different surface instabilities. Already U slightly larger than t yields a higher T_c for the magnetic surface state. In a narrow range of parameters the coexistence of $s+id$ and magnetic surface state is possible.

9.3 FS close to VHS

Next we consider the case of the *singular FS* close to the VHS by choosing $t' = -0.3t$ and $\mu = -t$. In order to obtain approximately the same value for the d-wave gap magnitude as in the previous case, we take $J = 1.2t$. Due to the VHS a large part of the low-energy quasiparticles come from the k-space regions around the $(\pi, 0)$ and $(0, \pi)$ points (in crystal coordinates). Since the wave function of the ABS is $\propto \sin k_{Fx} x$ and $k_{Fx} \approx \pi/a$ for most quasiparticles all quantities which live on the bonds and involve products of wave functions on neighboring sites (at distance $a/2$) oscillate like $\sin 2k_{Fx} x$. This also holds for the current carried by the bound states and the s-wave admixture at the surface. As a consequence, the surface currents carried by the ABS are nearly canceled and we do not find a transition towards a pure d-wave SSC state down to very low temperatures. This is in contrast to the results for the regular FS, that resemble those from quasi-classical theory which is insensitive to effects on such a microscopic length scale. Even if we admit a finite s-wave coupling the critical temperature for the s admixture is drastically reduced compared with the previous case ($T_c^s \approx 0.005t$) (Fig.9.5). The main reason for the small T_c^s is that the FS lies close to the node lines of the extended s-wave gap. Due to the smaller s-wave admixture the split in the ZEP for the $s+id$-wave state is rather weak (see Fig.9.5 d)). Our results are in in qualitative agreement with the results of Tanuma et al. [Tanuma 1998] who use a $t-J$ model in Gutzwiller approximation at comparable band filling.

For finite Coulomb repulsion $U = t$ we again find a magnetic surface state. The VHS

enhance correlations with the wavevector close to (π, π) so that the magnetization resembles a spin density wave with period a decaying towards the bulk region (see Fig.9.5 b)). The induced p_y gap component also exhibits $2k_F$ oscillations. We obtain a sizable split in the surface DOS, the spin-resolved density of states is shown in the lower panel of Fig.9.5. We find also additional bound states at higher positive energies. This is apparently an effect of the FS, the vicinity to the VHS is responsible for the strong electron-hole asymmetry. However these bound states exist in the entire d-wave phase and are therefore not related to the low temperature surface phase transitions. We would like to remark here: (1) the magnetization approaches the ideal staggered magnetization with period a when we choose $t' = 0$ and, additionally, stay close to half filling; (2) the chosen values $U = t$ and $t' = -0.3t$ are insufficient to establish a Néel state in the bulk in the absence of superconductivity. However, the rearrangement of the ABS provides a mechanism to stabilize the magnetic surface state.

For the *singular FS* the critical temperature T_c^m for the magnetic surface state easily exceeds T_c^s for the $s + id$-wave state (see Fig.9.5 c) and Fig.9.6), so that our results suggest that the magnetic surface state is the most stable state in the considered frame of possibilities. However an external magnetic field creating a Doppler shift for the quasiparticles and therefore again lifting the charge degeneracy of the ABS would support the $s + id$-wave state in the competition with the seemingly quite robust magnetic surface state. Note that the charge coupling corresponds to a considerably higher energy scale than the Zeeman coupling which is negligible in this case. This could induce a transition between these two surface states as the external field is increased. We also refer the reader to a recent preprint by Hu and Yan [Hu 1999], who discuss possible giant magnetic moments due to the split surface states.

9.4 Conclusion

In summary, we have considered different mechanisms to explain the observed low temperature splitting of the ZEP at [110] surfaces of d-wave superconductors. On the one hand, we find that a TRSB superconducting state leads to this effect which is induced by the Doppler shift of a spontaneous surface current [Higashitani 1997, HS 1997] or by the local admixture of an s-wave component $(s + id)$ [Fogelström 1997, Fogelström 1998]. On the other hand, electron correlation effects lead to a magnetic instability related to the antiferromagnetic state. Naturally, the latter is more stable in the underdoped regime represented in our case by the model with a singular FS. The former has a better chance to be realized in the overdoped region (regular FS) where the antiferromagnetic spin fluctuations are sufficiently reduced. The experimental distinction between the two states is possible by spin-polarized tunneling as the magnetic state leads to a splitting of the surface DOS for up and down spin.

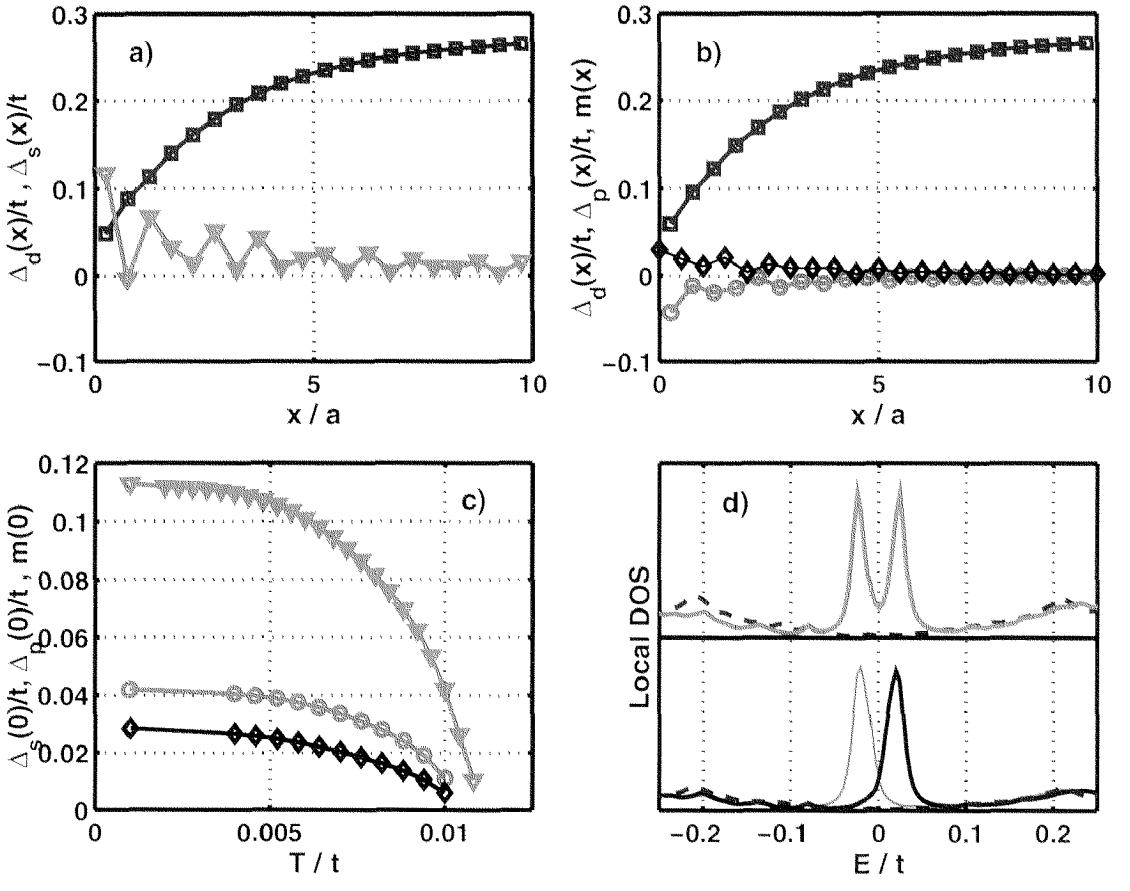

Figure 9.4: *Regular FS scenario (i.e. $t' = 0$, $J = 2t$, $\mu = -t$ and $T_c^d = 0.11t$): a) d-wave gap (squares) and TRSB s-wave admixture (triangles) at $T = 0.001t$ for $U = 0$. b) d-wave gap, magnetization (diamonds) and TRSB p-wave admixture (circles) at $T = 0.001t$ for $U = t$. c): Temperature dependence of the s-wave gap function, p-wave gap function and magnetization on the first site. d) upper panel: Local DOS in the $s + id$ state at the surface (solid line) and in the bulk (dashed line); lower panel: Local DOS in the magnetic surface state at the surface (solid lines, spin-up and spin-down DOS separate) and in the bulk (dashed line).*

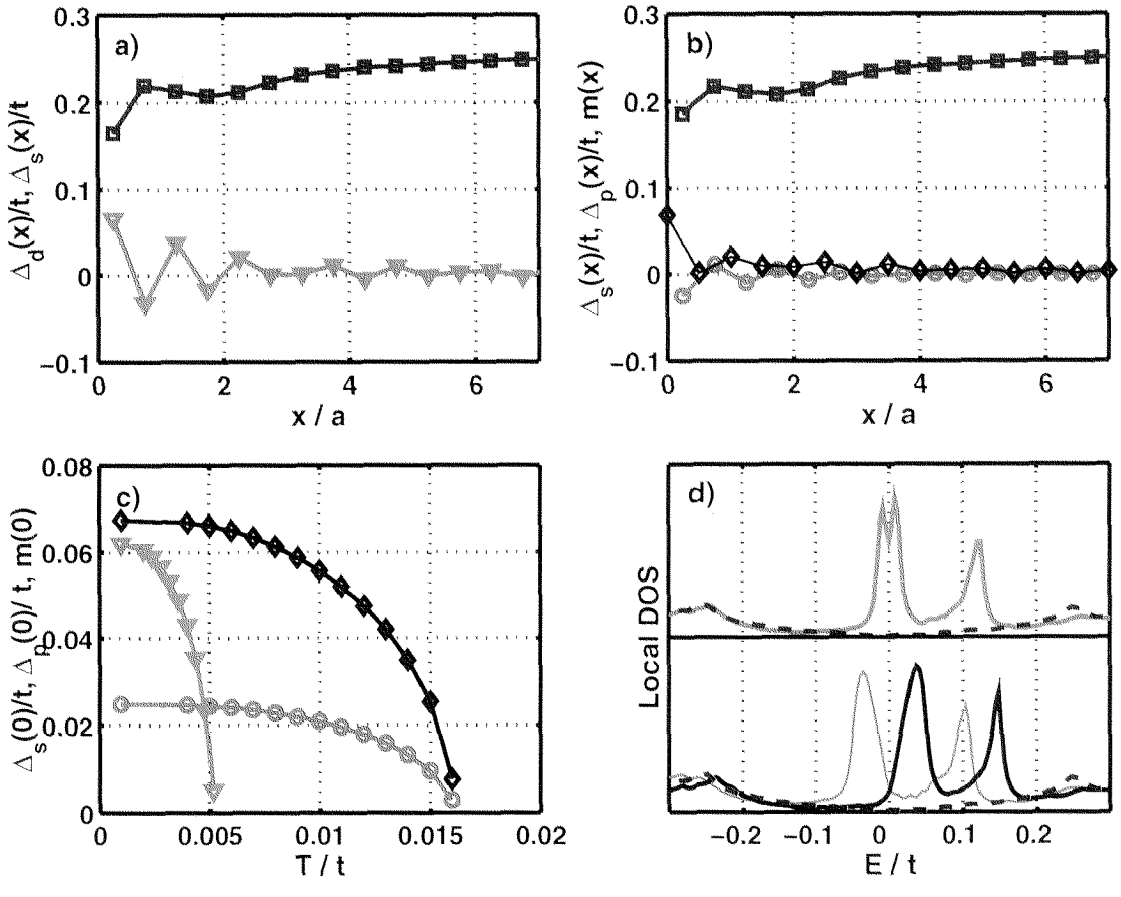

Figure 9.5: *Singular FS scenario (i.e. $t' = -0.3t$, $J = 1.2t$, $\mu = -t$ and $T_c^d = 0.12t$): a) d-wave gap (squares) and TRSB s-wave admixture(triangles) at $T = 0.001t$ for $U = 0$. b) d-wave gap, magnetization (diamonds) and TRSB p-wave admixture (circles)at $T = 0.001t$ for $U = t$. c) Temperature dependence of the s-wave gap function, p-wave gap function and magnetization on the first site. d) upper panel: Local DOS in the $s + id$ state at the surface (solid line) and in the bulk (dashed line); lower panel: Local DOS in the magnetic surface state at the surface (solid lines, spin-up and spin-down DOS separate) and in the bulk (dashed line).*

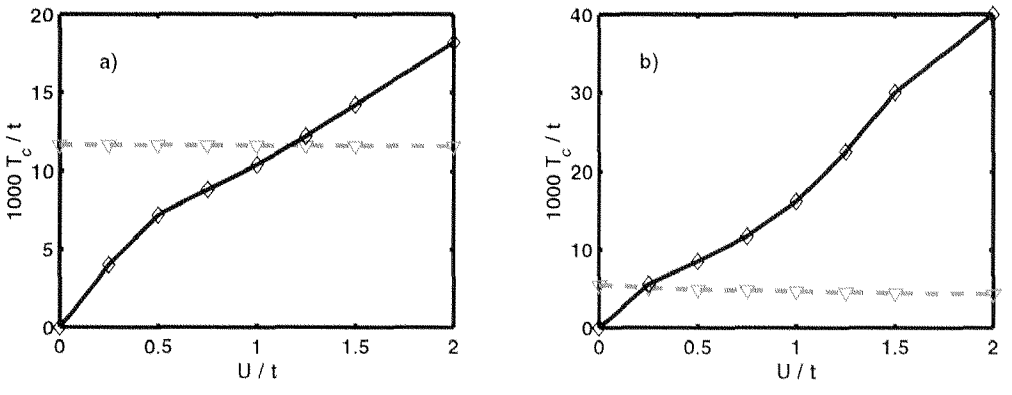

Figure 9.6: *U-dependence of the critical temperature for the $s + id$-wave (dashed line) and the magnetic surface state (solid line) for the regular FS (a)) and the singular FS scenario (b)).*

Bibliography

[Abanov 2000] Ar. Abanov, A.V. Chubukov, and J. Schmalian, cond-mat/0005163.

[AGD] A.A. Abrikosov, L.P. Gorkov and I.E.Dzyaloshinski, *Methods of Quantum Field Theory in Statistical Physics*, Dover, New York, 1975.

[Altmann 1997] J. Altmann, W. Brenig and A.P. Kampf, cond-mat/9707267.

[Alvarez 1998] J.V. Alvarez et al., J.Phys.Soc.Jpn. **67**, 1868 (1998).

[Andersen 1995] O.K.Andersen, A.I.Liechtenstein, O.Jepsen and F.Paulsen, J.Phys.Chem.Solids, Vol. **56**, 1573 (1995).

[Anderson 1970] P.W. Anderson, J.Phys. C**3**, 2436 (1970).

[Anderson 1997] P.W. Anderson, *The Theory of Superconductivity in the High-T_c Cuprates*, Princeton University Press (1997).

[Anderson 2000] P.W. Anderson, cond-mat/0007287.

[Auerbach 1994] A. Auerbach, *Interacting Electrons and Quantum Magnetism*, Springer-Verlag (1994).

[Balents 1996] L. Balents and M.P.A. Fisher, Phys.Rev.B **53**, 12133 (1996).

[Baranov 1992] M.A.Baranov, A.V.Chubukov, and M.Yu.Kagan, Int. J. of Mod. Phys. **6**, 2471 (1992).

[Becca 2000] F.Becca, L. Capriotti, and S.Sorella, cond-mat/0006353.

[Bednorz&Müller 1986] J.G. Bednorz, K.A. Müller, Z.Phys. B**64**, 189 (1986).

[Bourbonnais 1991] C. Bourbonnais in *Strongly interacting fermions and high T_c superconductivity*, LesHouches 1991, Eds. B. Doucot and J. Zinn-Justin, North Holland, Elsevier Science Amsterdam.

[Brinkman&Rice 1970] W.F. Brinkman and T.M. Rice, Phys.Rev. B**2**, 4302 (1907).

[Calandra 2000] M.Calandra and S.Sorella, Phys.Rev. B**61**, R11894 (2000).

[Chen 1995] T. Chen, J. Fröhlich, and M. Seifert, cond-mat/9508063, appeared in *Fluctuatin Geometries in Statistical Mechanics and Field Theory*, edited by F.David, P. Ginsparg, and J. Zinn-Justin, Elsevier Science B.V. (1996); see also J. Fröhlich and R. Götschmann, Phys. Rev. B**55**, 6788 (1996).

[Covington 1997] M.Covington, M.Aprili, E.Paraonu, L.H.Greene, F.Xu, J.Zhu, and C.A. Mirkin, Phys.Rev.Lett. **79**, 277 (1997).

[Dagotto 1992] E.Dagotto, J. Riera, and D.J. Scalapino, Phys.Rev. B**45**, 5744 (1992).

[Dagotto 1994] E. Dagotto, Rev.Mod.Phys. **66**, 763 (1994).

[Dagotto&Rice 1996] E. Dagotto and T.M. Rice, Science **271**, 618 (1996).

[Duffy 1996] D.Duffy and A.Moreo, Phys.Rev. B**55**, R676 (1996). A.P. Kampf is acknowleged for pointing out this reference.

[Dupuis 1998] N. Dupuis, Euro.Phys.J. B**3**, 315 (1998).

[Dzyaloshinski 1987] I. Dzyaloshinskii, Sov.Phys.JETP **66**, 848 (1987); I. Dzyaloshinskii, J.Phys.I (France) **6**, 119 (1996).

[Fabrizio 1993] M. Fabrizio, Phys.Rev.B**48**, 15838 (1993).

[Fauchère 1999] A.L. Fauchere, W. Belzig, and G. Blatter, Phys.Rev.Lett. **82**, 3336.

[Fazekas 1999] P. Fazekas, *Lecture Notes on Electron Correlation and Magnetism*, World Scientific, Singapore (1999).

[Fisher 1998] M.P.A. Fisher, cond-mat/9806164 and references therein.

[M.E.Fisher 1998] Rev.Mod.Phys. **70**, 653 (1998).

[Fogelström 1997] M.Fogelström , D.Rainer, and J.A.Sauls, Phys.Rev.Lett. **79**, 281 (1997).

[Fogelström 1998] M. Fogelstrom and S.K. Yip, cond-mat/9803031.

[Fournier 1998] P. Fournier et al., Phys.Rev.Lett **81**, 4720 (1998).

[Fradkin 1991] E. Frdakin, *Field Theories of Condensed Matter Systems*, Addison Wesley Publishing Company (1991).

[Furukawa] N. Furukawa, unpublished.

[Furukawa 1998] N. Furukawa, T.M. Rice, and M. Salmhofer, Phys.Rev.Lett. **81**, 3195 (1998).

[Gebhard 1999] F. Gebhard, *The Mott Metal-Insulator Transistion*, Springer Tracts in Modern Physics 137, Springer-Verlag Berlin (1997).

[Gell-Mann 1954] M.Gell-Mann and F.Low, Phys.Rev. **95**, 1300 (1954).

[Georges 1996] A.Georges, G.Kotliar, W.Krauth, and M.J. Rozenberg, Rev. Mod. Phys. **68**, 13 (1996).

[Bulla 1999] R. Bulla, Phys.Rev.Lett. **83**, 136 (1999).

[Geshkenbein 1997] V.B. Geshkenbein, L.B. Ioffe, A.I. Larkin, Phys. Rev. B **55**, 3173 (1997).

[Gonzalez 1996] J. Gonzalez et al., Europhys.Lett. **34**, 711 (1996); J. Gonzales et al., Nucl.Phys. B **485**, 694 (1997).

[Greene 1997] L.H. Greene, M.Covington, M.Aprili, and E.Paraoanu, Solid State Comm. **107**, 649 (1998); L.Alff et al., Phys.Rev.B **55**, R14757 (1997).

[Halboth 2000] C.J. Halboth and W. Metzner, Phys.Rev.B **61**, 7364 (2000).

[Haldane 1983] F.D.M Haldane, Phys.Lett **93**A, 464 (19983); Phys.Rev.Lett. **50**, 1153 (1983).

[Heeb 1994] E.S. Heeb and T.M. Rice, Europhys.Lett. **27**, 673 (1994).

[Hewson 1994] A.C.Hewson, Adv. Phys. **43**, 543 (1994).

[Higashitani 1997] S.Higashitani, J.Phys.Soc.Jap. **66**, 2556 (1997);

[Hlubina 1997] R.Hlubina, S.Sorella, and F. Guinea, Phys.Rev.Lett. **78**, 1343 (1997).

[Hlubina 1999] R. Hlubina, Phys.Rev. B**59**, 9600 (1999).

[Hodges 1971] C. Hodges, H. Smith, and J.W. Wilkins, Phys.Rev. B **4**, 302 (1971).

[Hofstetter 1998] W.Hofstetter and D.Vollhardt, Ann.Phys. **7**, 48 (1998).

[HS 1997] C.Honerkamp and M.Sigrist, unpublished (1997).

[HS 1998] C. Honerkamp and M. Sigrist, Prog.Theo.Phys. **100**, 53 (1998).

[HSFR 1999] C. Honerkamp, M. Salmhofer, N. Furukawa and T.M. Rice, cond-mat/9912358, to be published in Phys.Rev. B.

[HS 2000] C. Honerkamp and M. Sigrist, Europhys.Lett. **50**, 368 (2000).

[Hu 1995] C.R.Hu, Phys.Rev.Lett. **72**, 1526 (1995); S.Kashiwaya, Y.Tanaka, M.Koyanagi, and K.Kajimura, Phys.Rev.B **53**, 2667 (1996).

[Hu 1999] C.R.Hu and X.Z.Yan, cond-mat/9901334.

[Ioffe 1998] L.B. Ioffe, A.J. Millis, Phys. Rev. B **58**, 11631 (1998); V.B Geshkenbein, L.B. Ioffe, A.J. Millis Phys. Rev. Lett. **80**, 5778 (1998).

[Kastrinakis 2000] G.Kastrinakis, Physica C (2000); cond-mat/0005485.

[Khveshchenko 1994] D.V. Khveshchenko, Phys.Rev. B**50**, 380 (1994).

[Khveshchenko 1994] D.V. Khveshchenko and T.M. Rice, Phys.Rev. B**50**, 252 (1994).

[Kohn&Luttinger 1965] W. Kohn, J.M. Luttinger, Phys. Rev. Lett. **15**, 524 (1965).

[Kontani 1999] H. Kontani, K, Kani, and K. Ueda, Phys. Rev. B**59**, 14723 (1999).

[Kopietz 1997] P. Kopietz, *Bosonization of interacting fermions in arbitrary dimensions*, Lecture Notes in Physics LNP m48, Springer, (1997).

[Laughlin 2000] R.B. Laughlin and D.Pines, PNAS, Jan 1, (2000).

[Lederer 1987] P. Lederer, G. Montambaux and D. Poilblanc, J.Phys. **48**, 1613 (1987).

[Ledermann 2000] U. Ledermann, K. Le Hur, and T.M. Rice, cond-mat/0002445, to be published in Phys.Rev. B.

[Lee 1999] P.A. Lee, Physica C **317-318**, 194 (1999), (cond-mat/9812226) and references therein.

[Liechtenstein 1999] A.I.Liechtenstein and M.I.Katsnelson, cond-mat/9911320.

[Lin 1998] H. Lin, L. Balents, and M.P.A. Fisher, Phys.Rev.B **58**, 1794 (1998).

[LSM 1961] E. Lieb, Th. Schulz, and D. Mattis, Ann.Phys. **16**, 407 (1961).

[Luther&Emery 1974] A.Luther and V.J. Emery, Phys.Rev.Lett **33**, 589 (1974).

[Maier 2000] Th.Maier, M.Jarrell, Th. Pruschke, and J.Keller, cond-mat/0002352.

[Manousakis 1991] E. Manousakis, Rev Mod. Phys. **63**, 1 (1991).

[Metzner 1989] W.Metzner and D.Vollhardt, Phys.Rev.Lett. **62**, 324 (1989).

[Metzner 1998] W. Metzner, C. Castellani, and C. Di Castro, Adv.Phys. **47**, 317 (1998).

[Morita 1999] K. Morita and K. Miyake, cond-mat/9912292.

[Negele&Orland 1988] J.W. Negel and H.Orland, *Quantum Many-Particle Systems*, Addison-Wesley Publishing Company (1988).

[Noack 1994] R.M. Noack, S.R White and D.J. Scalapino, Phys.Rev.Lett. **73**, 882 (1994).

[Norman 1998] M.R.Norman et al., Nature **392**, 157 (1998).

[Pines&Nozières] D.Pines and P.Nozières, *Theory of Quantum Liquids*.

[Plakida 1995] N.M. Plakida, *High-Temperature Superconductivity*, Springer (1995).

[Prozorov 2000] R.Prozorov, R.W. Gianetta, P. Fournier and R.L.Greene, cond-mat/0002301.

[Renner 1998] Ch. Renner, B. Revaz, J.Y. Genoud, K. Kadowaki, and O. Fischer, Phys.Rev.Lett **80**, 149 (1998).

[Rice 1993] T.M. Rice, S. Gopalan, and M. Sigrist, Euro.Phys.Lett. **23**, 445 (1993).

[Rice 1997] T.M. Rice, S. Haas, M. Sigrist, and F.C. Zhang, Phys.Rev. B**56**, 14655 (1997).

[Sachdev 1999] S.Sachdev, *Quantum Phase Transitions*, Cambridge University Press (1999).

[Salmhofer 1999] M.Salmhofer, *Renormalization: An Introduction*, Texts and Monographs in Physics, Springer (1999).

[Scalapino 1986] D.J. Scalapino, E. Loh Jr., and J.E. Hirsch, **34**, 8190 (1986).

[Schulz 1987] H.J. Schulz, Europhys.Lett. **4**, 609 (1987).

[Schulz 1996] H.J. Schulz, Phys.Rev. B**53**, 2959 (1996).

[Schulz 1999] H.J. Schulz, Phys.Rev. B**59**, R2471 (1999).

[Shankar 1994] R.Shankar, Rev.Mod.Phys. **66**, 129 (1994).

[Sigrist 1994] M.Sigrist, T.M.Rice, and F.C. Zhang, Phys.Rev. B**49**, 12058 (1994).

[Sigrist 1998] For a review see M. Sigrist, Prog. Theor. Phys. **99**, 899 (1998).

[Sigrist&Ueda 1991] M.Sigrist and K.Ueda, Rev.Mod.Phys.**63**, 239 (1991).

[Solyom 1979] J. Solyom, Adv.Phys. **28**, 201 (1979).

[Stückelberg 1953] E.Stückelberg and A.Petermann, Helv.Phys.Acta **26**, 499 (1953).

[Tallon 2000] J.L Tallon and J.W.Loram, cond-mat/0005063.

[Tanuma 1998] Y.Tanuma, Y.Tanaka, M.Ogata, and S.Kashiwaya, J.Phys.Soc.Jap. **67**, 1118 (1998); see also J.X.Zhu, B.Friedman and C.S.Ting, Phys.Rev.B **59**, 3352 (1999).

[Tasaki 1998] H.Tasaki, Prog.Theor.Phys. **99**, 489 (1998).

[Timusk 1999] T. Timusk and B. Statt, Rep.Prog.Phys. **62**, 61 (1999).

[Troyer 1996] M.Troyer, H.Tsunetsugu, and T.M.Rice, Phys.Rev. B**53**, 251 (1996).

[Tsuei 1989] C.C.Tsuei et al., Physica C**161**, 415 (1989).

[Tsuei 2000] C.C. Tsuei, J.R.Tsuei, Phys.Rev.Lett. **85**, 182 (2000).

[Valla 2000] T.Valla, A.V.Federov, P.D.Jhonson, Q.Li, G.D.Gu and N.Koshizuka, cond-mat/0003407.

[Van Dongen 1989] P.G.J. van Dongen, F.Gebhard and D.Vollhardt, Z.Phys. B**76**, 199 (1989).

[van Harlingen 1995] D.J. van Harlingen, Rev.Mod.Phys. **67**, 515 (1995), and references therein.

[Vistulo 1997] F. Vistulo de Abreu, B. Doucot, Euro.Phys.Lett. **38**, 533 (1997).

[Voit 1994] J.Voit, Rep.Prog.Phys. **57** 977 (1994).

[Vollhardt 1999] D.Vollhardt, N.Blümer, K.Held, M.Kollar, J.Schlipf, M.Ulmke, and J.Wahle, *Advances in Solid State Physcis* **38**, 383 (1999).

[Wakabayashi 1996] M. Fujita, K. Wakabayashi, K. Nakada and K. Kusakabe, J. Phys. Soc. Jpn. **65**, 565 (1996).

[Walter 1998] H.Walter, W.Prusseit, R.Semerad, H.Kinder, W.Assmann, H.Huber, H.Burkhardt, D.Rainer, and J.A.Sauls, Phys.Rev.Lett. **80**, 3598 (1998).

[Weinberg 1997] S. Weinberg, *The Quantum Theory of the Fields*.

[White 2000] S.R. White and D.J. Scalapino, cond-mat/0006071; Phys.Rev. B**60**, R753 (1999).

[Wilson&Fisher 1972] K.G. Wilson and M.E.Fisher, Phys.Rev.Lett. **28**, 240 (1972).

[Wilson 1975] K.G. Wilson, Rev.Mod.Phys. **47**, 773 (1975).

[Yanase 1999] Y. Yanase and K. Yamada, J.Phys.Soc.Jap. **68**, 548 (1999).

[Zanchi 1997] D. Zanchi and H.J. Schulz, Europhys.Lett. **44**, 235 (1997); D. Zanchi and H.J. Schulz, Phys. Rev. B **61** 13609 (2000).

[Zhang 1988] F.C. Zhang and T.M Rice, Phys. Rev. B **37**, 3759 (1988).

[Zheleznyak 1997] A.T. Zheleznyak, V.M. Yakovenko, and I.E. Dzyaloshinskii, Phys.Rev.B **55**, 3200 (1997).

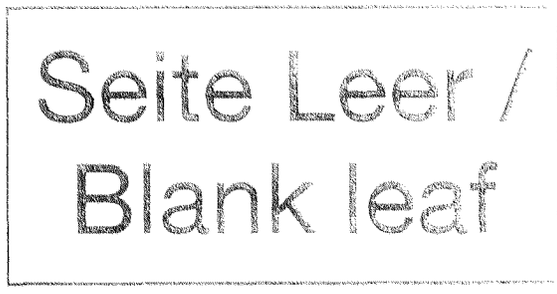
Seite Leer /
Blank leaf

Acknowledgments

It has been a great pleasure to be a student at the ITP at ETH Zürich. First of all I like to thank Maurice Rice and the two Manfreds from distant cultures: Manfred Salmhofer (from mathematics) and Manfred Sigrist (from Japan). Apart from being marvelous persons who guided me through the different projects, at any time open for discussions, they always conveyed the feeling that my work was not just filling up the gaps left by the big guys but that it was interesting for them and some non-vanishing part of the condensed matter community. Further I like to thank Prof. D. Vollhardt for co-examining this thesis and awaking my interest to several related questions.

I also benefited a lot from so many people in the institute: In the early phase I learned a lot about physics and the condensed matter community from Daniel Agterberg (the more pragmatic questions) and Stefan Haas (the more philosophical part, supported by Thierry Müller) and my E-floor colleagues Alban Fauchere, Beat Frischmuth and Rolf Heeb. Later when I moved to the G15 office a had a lot of fun with Misha Zhitomirsky (particular thanks for answering infinitely many questions about physics and phone calls from the outside world) and Thomas Siller (the sports conscience). Nobuo Furukawa helped me a lot to get into the Fermi liquid destruction business. Special thanks to Gianni Blatter for being an entertaining driving force through all my years at ETH, Matthias Troyer for support on many levels (someday I will learn C++, perhaps...) and Dima Geshkenbein for giving amusing lectures on early Friday mornings. Also thanks to Urs Ledermann and Karyn Lehur for numerous discussions up and down the ladders.

Moreover thanks to all the more or less wonderful people here: Walter Aschbacher, Lothar Birke, Malek Boudiab, Hans-Peter Büchler, Laura Cattaneo, Thomas Chen, Pierre-Alain Genilloud, Matthew Dodgson, Denis Gorokhov, David Hasler, Dima Ivanov, Raphael Micha, Mathias Körner, Andreas Läuchli, Bill Pedrini, Guido Schmid, Kai Schnee, Orlando Wagner, Johannes Walcher and Peter Widerin for enjoyable times inside and outside the Institute.

Seite Leer /
Blank leaf

Curriculum Vitae

Persönliche Daten

Name:	Carsten Honerkamp
Geburt:	14. Dezember 1971, in Genf/Schweiz.
Nationalität:	Deutsch

Ausbildung

1978-1982	Grundschule in Emmendingen/Baden-Württemberg
1982-1991	Goethe-Gymnasium Emmendingen, 1991 Abitur
1991-1992	Zivildienst am Kreiskrankenhaus Emmendingen
1992-1995	Physikstudium an der Ruprecht-Karls-Universität Heidelberg.
1994	Vordiplom
1995-1997	Physikstudium an der ETH Zürich
1997	Diplom mit Diplomarbeit "Andreev Reflection in Non-Unitary Superconducting States" bei M. Sigrist im Institut für theoretische Physik der ETH Zürich. Gesamtnote ausgezeichnet mit dem "Willi-Studer-Preis" der ETH Zürich.
1997-2000	Doktoratsstudium im Institut für theoretische Physik an der ETH Zürich bei Prof. T.M. Rice.